# APPLICATION OF BRILLOUIN SCATTERING IN STUDYING THE PHYSICAL PROPERTIES OF METAL ORGANIC FRAMEWORKS, NANOTUBES, IONIC LIQUIDS AND SPIN ICE

A Thesis

Submitted for the Degree of

*Doctor of philosophy*

By

DHANYA R


CHEMISTRY AND PHYSICS OF MATERIALS UNIT

JAWAHARLAL NEHRU CENTRE FOR ADVANCED SCIENTIFIC RESEARCH

BANGALORE – 560 064, INDIA.

November 2015

*Dedicated to*

*Achan and Amma*

# DECLARATION

I hereby declare that the matter embodied in this thesis entitled "**Application of Brillouin Scattering in Studying the Physical Properties of Metal Organic Frameworks, Nanotubes, Ionic Liquids and Spin Ice**" is the result of the investigations carried out by me in the Chemistry and Physics of Materials Unit, Jawaharlal Nehru Centre for Advanced Scientific Research (JNCASR), Bangalore, India, under the supervision of Professor Chandrabhas Narayana.

In keeping with the general practice of reporting scientific observations, due acknowledgements have been made whenever the work described is based on the findings of other investigators. Any omission which might have occurred by oversight or error in judgement is regretted.

_____

(Dhanya R)

# CERTIFICATE

I hereby certify that the matter embodied in this thesis entitled "**Application of Brillouin Scattering in Studying the Physical Properties of Metal Organic Frameworks, Nanotubes, Ionic Liquids and Spin Ice**" has been carried out by Ms. Dhanya R at the Chemistry and Physics of Materials Unit, Jawaharlal Nehru Centre for Advanced Scientific Research (JNCASR), Bangalore, India under my supervision and that it has not been submitted elsewhere for the award of any degree or diploma.

_____

Prof. Chandrabhas Narayana

(Research Supervisor)

# ACKNOWLEDGEMENTS

*I take this opportunity to acknowledge and extend my gratitude to the people who have inspired, motivated and supported me in my academic and personal life.*

*First of all, I would like to thank Prof. Chandrabhas Narayana for all the support and encouragement in professional as well as personal life. I am grateful to him for providing guidance, enormous freedom at workplace and for giving an opportunity to work on wide variety of scientific problems. He is one of the most friendly research supervisor one can get and I will cherish the memory of working with him forever.*

*I would like to thank Prof. Ajay K Sood for his collaborations as well as for the stimulating scientific discussions. I really liked his approach in attempting scientific problems.*

*I would like to thank all my collaborators: Prof. G. U. Kulkarni (JNCASR, Bangalore), Dr. Sebastian C Peter (JNCASR, Bangalore), Dr. Ranjan Datta (JNCASR, Bangalore), Prof. Sundaresan (JNCASR, Bangalore), Prof. Aninda J Bhattacharya (IISc, Bangalore), Dr. Supti (IISc, Bangalore), Dr. Narendra (JNCASR, Bangalore), Mr. Umesh Mogera (JNCASR, Bangalore), Mr. Rana Saha (JNCASR, Bangalore), Mr. Soumyabrata (JNCASR, Bangalore), Mr. Sumanta (JNCASR, Bangalore) and Mr. Rajib Sahu (JNCASR, Bangalore). It has been a great pleasure to work and learn from them.*

*I would like to thank the faculties of CPMU, TSU and Prof. Guru Row (IISc) for their wonderful courses. I had some useful discussions with Prof. Umesh V. Waghmare who has also given me an opportunity to work on first principle calculations. I sincerely thank him for that.*

*I have learnt a lot from the scientific discussions which we had. Particularly, I would like to thank Dr. Venkata Srinu Bhadram who has introduced me most of the experimental techniques present in our lab. Also, I would like to specially thank Dr. John Sandercock from whom I learnt about the critical alignment procedures of the Brillouin spectrometer. Without his inputs few of the works presented in this thesis would have been impossible.*

*I had some amazing lab mates like Partha, Srinu, Soumik, Gayatri, Rajaji, Shantanu, Priyank, Divya, Priyanka, Gopal, Dipti, Santosh, Sorb, Jyothi. We have always learnt*

*from each other. We had lots of fun together and they have always kept the lab atmosphere a wonderfull place to work. I thank all of them.*

*I would also like to thank my batch mates and friends at JNCASR. Few of them need special mention. They are Sunaina, Summayya, Darshana, Dibya, Anindita, Gangaih, Bavani, Shvetha, Arpita, Dileep, Sonu, Sharma, Narendra and Dasari. I thank all of them for their support and encouragement.*

*I thank my friends Asweel, Asa, Sreeshma, Aneesh, Shiju, Gopika and Darshan for making my life memorable and pleasant. I express my heartfelt thank to all the academic, technical, library and computer lab staff members of JNCASR. I specially thank Mr. Arokyanathan, who was in the workshop and has helped us in fabricating many of our experimental designs.*

*I thank my guru Prof. Sitharaman for motivating me to choose research as my career.*

*I acknowledge UGC, India for fellowship and contingency grants. I would also like to acknowledge JNCASR and DST, India for the international travel grants.*

*I would like to take this very special opportunity to thank my family who have been very supportive. I express my special thanks to few of our family friends, Peter Uncle, Benzey aunty and Family, and Sujith for their love and support. I specially thank my father for inspiring and motivating me to choose research as my career and I dedicate this work to my Father and Mother.*

# Table of Contents

# Preface

Brillouin spectroscopy is a non contact probe to study the elastic properties of materials. In this thesis, the technique of Brillouin spectroscopy has been used to study the physical properties of different kinds of materials at ambient conditions and as a function of temperature or pressure. Raman spectroscopy has been used in certain cases to understand the changes in the local structure and has helped in supplementing the Brillouin results. This thesis is divided into seven chapters. The first chapter gives an introduction about the techniques used and second chapter explains the experimental details. The remaining chapters deal with utilising Brillouin spectroscopy in studying different aspects of the Brillouin spectra, taking one example each from metal organic frameworks, carbon nanotubes, ionic liquids and spin ice. Each chapter includes topical introduction on the problem which is being addressed.

Chapter 1 accounts a thorough introduction about the general aspects of Brillouin scattering and a brief discussion on deriving the elastic constants from the acoustic modes. The central peak and second sound which can be observed in certain samples using Brillouin spectroscopy is also discussed. A brief overview on the high pressure Brillouin technique and Raman spectroscopy is also given. Chapter 2 describes the experimental details which include the design and working principle of Brillouin and Raman setup and the methods of doing high pressure experiment.

Chapter 3 deals with the effect of guest incorporation on the elastic properties, linewidth and central peak of zeolitic imidazolate framework-8 (ZIF-8) at ambient and low temperatures. The guest incorporation at ambient conditions shows that pore occupancy plays a major role in the mechanical properties of ZIF-8. The temperature dependence on adsorbing different gases ($N_2$, Ar, and CO2) demonstrated the gate opening behaviour and a hardening of otherwise low shear modulus.

In chapter 4, the pressure dependence of the longitudinal acoustic mode of ZIF-8 is investigated in the presence of two pressure transmitting mediums- methanol: ethanol mixture and 1-propanol. This work demonstrated that, incorporating guest in the pores increases the elastic constants as well as plays a major role in determining the gate opening behaviour. Interaction between the guest and framework under high pressure was investigated using Raman spectroscopy.

In Chapter 5, we have discovered the existence of second sound in double walled carbon nanotubes and have studied its temperature dependence. Central peaks observed were used for determining the thermal conductivity and various relaxation times existing in the system. The relaxation times thus obtained was used to prove the existence of 'window condition' which is necessary for the propagation of second sound.

Chapter 6 deals with the temperature dependent Brillouin study of the phase transitions in pyrrolidinium based ionic liquids. From our study we have determined that, plastic crystals exhibits very low acoustic velocities as well as a higher linewidth which increases on decreasing the temperature. Moreover, we have shown that near the glass transition, linewidth and Brillouin shift exhibit differences depending on whether it is a structural glass or glassy crystal.

In chapter 7, we have studied the pressure dependence of a spin ice, $Dy_2Ti_2O_7$ and have determined the pressure dependence of its elastic constants. A transition was observed at 9 GPa from the change in slope of the elastic constants, bulk modulus and anisotropic factor. Softening of the shear modulus was observed above the transition at 9 GPa, from which we can predict a first order phase transition occurring at ultra higher pressures in this system.

The last chapter presents the summary of the thesis and the future prospects of the present work.

# Chapter 1

# Introduction

## 1.1 Scattering of Light

When light interacts with a material, it can be transmitted, absorbed or scattered. The scattered light contains both elastic and inelastic components. The scattering of light without any change in frequency (elastic scattering) is known as Rayleigh scattering. The blue colour of the sky is attributed to the Rayleigh scattering and can be explained by the well-known $\lambda^{-4}$ law put forward by Lord Rayleigh for the light scattering by objects smaller than the wavelength of incident light [1]. The elastic scattering from the scattering centres consisting of the spherical particles of any diameter is called Mie scattering [2]. The scattering intensity in this case generally does not have a strong dependence on the wavelength, but is sensitive to the particle size. Mie scattering coincides with Rayleigh scattering when the diameter of the particles is much smaller than the wavelength of the light.

Brillouin and Raman scattering constitute two major inelastic light scattering mechanisms attributed to the interaction of light with phonons (lattice vibrations). Light scattering in general results from the density fluctuations in the medium. The inelastic scattering from sound wave mediated density fluctuations results in Brillouin scattering and from polarizability fluctuations associated with optical phonons give rise to Raman scattering. The theory of inelastic scattering of light where the light is scattered by the density fluctuations associated with the acoustic waves in a homogeneous medium was independently investigated by Brillouin (1922) and Mandelstam (1926) [3,4]. They proposed that the light scattered by the thermally excited acoustic waves in a medium should be shifted in frequency with respect to the incident light by an amount equal to the frequency of the scattering fluctuations. The kinematics and the energy shift of the scattering can be described by the Bragg equation and the Doppler effect respectively. This phenomenon, is called Brillouin scattering (or Brillouin-Mandelstam scattering) and was first observed experimentally by Gross in 1930 in quartz [5]. In Raman scattering the photons interacts with the optical phonons, which are predominantly intra-molecular vibrations and rotations where the energies are larger than the acoustic phonons. The theory of Raman scattering was proposed by Smekal, who described the inelastic scattering by a system with two quantised energy levels [6]. Experimentally, it was successfully demonstrated, almost simultaneously, by Sir. C. V. Raman and Sir K. S. Krishnan in benzene and Landsberg and Mandelstam in quartz [7-10].

These two inelastic scattering techniques were immediately realized as potential tools for studying the excitations in different molecules and crystals. However, with the conventional light sources available before the development of lasers, the measurement of Brillouin and Raman scattering was limited only to compressed gases, fluids and a few solids, which had high scattering cross sections. The invention of lasers in 1960s made it possible to perform the inelastic light scattering measurements on a wider range of solids, liquids and gases. With improved spectrometers and optical detection devices, inelastic light scattering has now become a powerful technique for material characterization and for studying material properties under extreme thermodynamic conditions (both temperature and pressure).

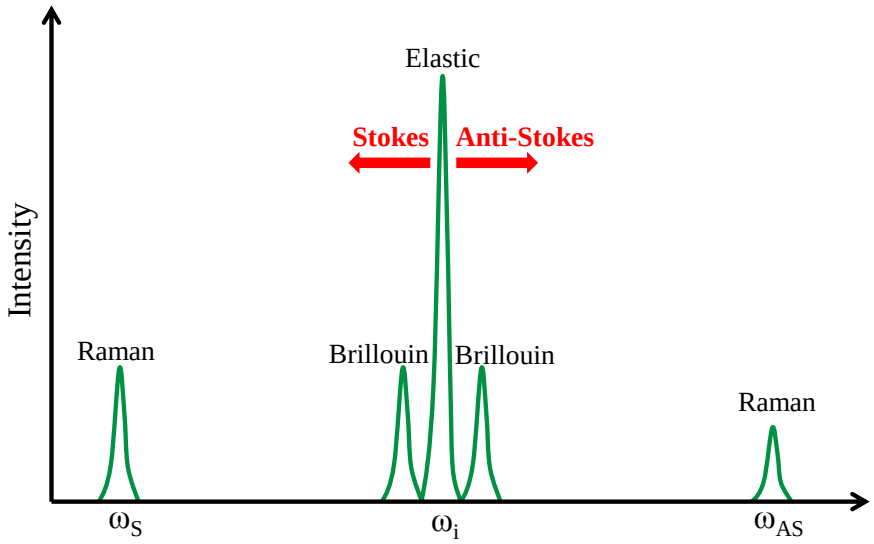


Fig. 1.1. The schematic representation of light scattering spectrum.

In both Raman and Brillouin scattering, energy is exchanged between light and the scattering medium. The Brillouin component resulting from the scattering by acoustic waves occurs close to the frequency of incident light with typical frequency shifts ranging from 0.1-6 $cm^{-1}$ while Raman shift ranges from 10-4000 $cm^{-1}$. The different frequency regime probed by these techniques demands the usage of different experimental techniques used for their study. Figure 1.1 shows the schematic of the scattered light spectrum. The inelastically scattered light is distributed over a range of frequencies on both sides of the incident light frequency. The scattered light with the frequencies smaller than the incident frequency ($\omega_i$) are called Stokes component ($\omega_{Stokes}$) and the frequencies larger than $\omega_i$ are called anti-Stokes component ($\omega_{AStokes}$). If $\boldsymbol{k}_i$, $\boldsymbol{k}_{Stokes}$ and

$\boldsymbol{k}_{AStokes}$ represents the wavevector of incident, Stokes and anti-Stokes scattered photons, then the law of conservation of energy and momentum (Fig. 1.2) is given by

$$\omega_{Stokes} = \omega_i - \omega,\ \boldsymbol{k}_{Stokes} = \boldsymbol{k}_i - \boldsymbol{q} \tag{1.1}$$

$$\omega_{AStokes} = \omega_i + \omega,\ \boldsymbol{k}_{AStokes} = \boldsymbol{k}_i + \boldsymbol{q} \tag{1.2}$$

where ω and $\boldsymbol{q}$ are the frequency and wavevector of the phonon involved in the scattering process. The following sections describe various aspects of the inelastic scattering techniques, with greater emphasis to the Brillouin scattering.

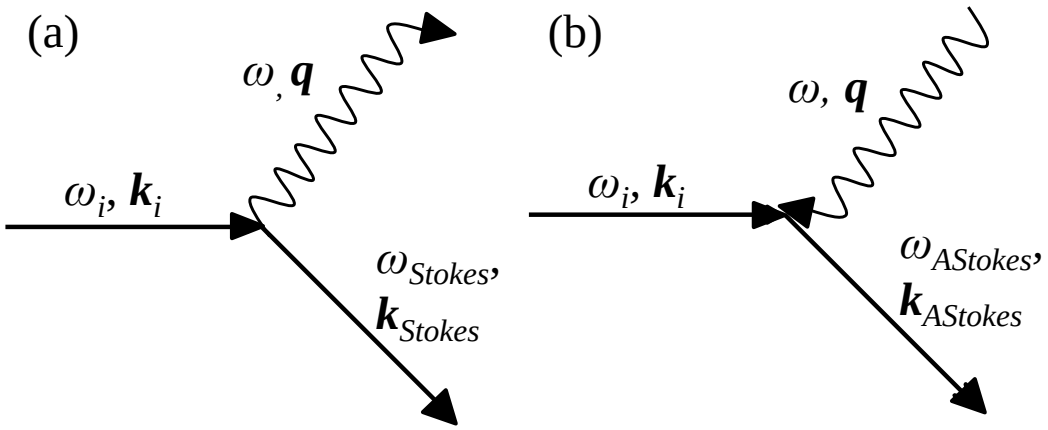


Fig. 1.2. The vector diagram for the conservation of energy and momentum in (a) Stokes and (b) anti-Stokes process.

## 1.2. Kinematics of Light scattering

The conservation of energy and momentum determines the kinematics of the inelastic light scattering. For a scattering medium with translational symmetry, the conservation conditions can be written in terms of the wavevector and the frequencies of the photons and elementary crystal excitations involved in the process. If $\omega_i$, $\omega_s$ and $\boldsymbol{k}_i$, $\boldsymbol{k}_s$ are the frequency and wavevector of incident and scattered light, the conservation of energy and momentum can be written as

$$\omega_i - \omega_s = \pm\omega \tag{1.3}$$

$$\boldsymbol{k}_i - \boldsymbol{k}_s = \pm\boldsymbol{q} \tag{1.4}$$

where $\omega$ and $\boldsymbol{q}$ are the frequency and wave vector of the elementary crystal excitations.

The magnitude of the scattering wavevector can be determined from the scattering geometry. Figure 1.3 shows the vector diagram depicting the scattering geometry where

the light is collected at an angle θ with respect to $\boldsymbol{k}_i$. The minimum and maximum values of $q$ will be obtained for the forward and scattering and backward scattering geometries, respectively. The value of $q$ in an isotropic media is

$$[n(\omega_i)\omega_i - n(\omega_s)\omega_s]/c \leq q \leq [n(\omega_i)\omega_i + n(\omega_s)\omega_s]/c \tag{1.5}$$

where $n$ and $c$ are the refractive index of medium and velocity of light in the vacuum. Eq .1.5 becomes $0 \leq q \leq 10^5$ cm$^{-1}$ for visible light scattering, implying that the accessible range of $q$ for visible light is very small compared to the length of the Brillouin zone ($10^8$ cm$^{-1}$). Hence the first order crystal excitations or phonons very close to the Brillouin zone centre (Γ) will be probed using inelastic light scattering techniques. Since the scattered wavevector changes only by a very small value, we can assume that $k_i = k_s = k$. Thus, from Fig. 1.3 we can show that

$$q = 2kSin(\theta/2) \tag{1.6}$$

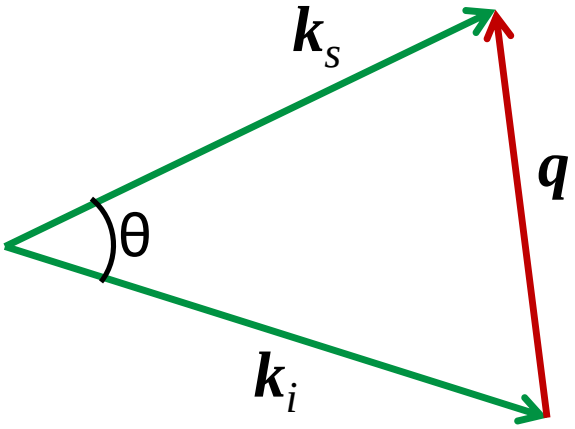


Fig. 1.3. Schematic representation of the scattering geometry.

Figure 1.4 shows the schematic of phonon dispersion relation along a general direction. The frequency of optical phonons (upper curves), do not change much near Brillouin zone centre ($q$ ~ 0) and can be studied using Raman spectroscopy. The three lower curves are the acoustic modes which shows linear dispersion $\omega = Vq$ ($V$ = velocity) for small $q$ and can be probed using Brillouin spectroscopy. Hence the Raman frequencies are insensitive to the scattering geometry while Brillouin scattering depends on the scattering geometry, enabling us to trace a small part of the dispersion curve by varying the scattering angle θ.

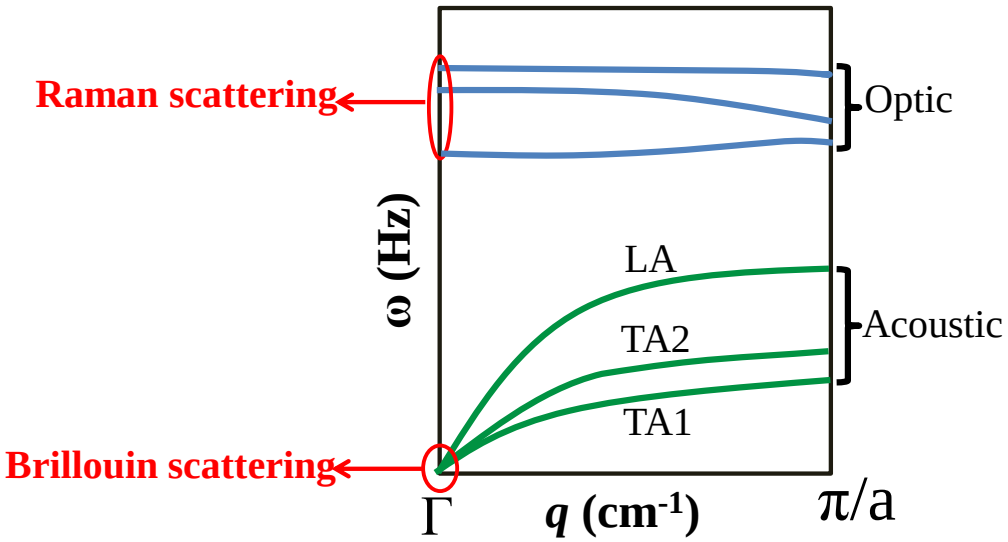


Fig. 1.4. The schematic representation of the phonon dispersion curve along a general direction for a lattice with two atom basis.

## 1.3. Brillouin scattering

Brillouin scattering is the inelastic scattering of light by the spontaneous thermal fluctuations or excitations in a material which results in the fluctuation in the dielectric tensor of a material. The acoustic phonons at the Brillouin zone centre as well as excitations from magnons, plasmons *etc*. contribute to such fluctuations. The Brillouin spectrum provides information about the various properties of materials like acoustic sound velocities, attenuation coefficients, structural relaxation, thermal diffusivity, elastic and photo elastic properties *etc*. Brillouin spectroscopy can be also used for determining the optical properties like refractive index of a material. The Brillouin peak shift can be used to estimate the velocity and elastic properties of the materials while their width gives information about life time, acoustic attenuation *etc*. In addition to the acoustic peaks, the Brillouin spectrum also contains a non shifted central peak which provides information on the structural relaxation/diffusion in the liquids and gases and thermal diffusivity in the case of solids. The thermal diffusivity can be used to derive the thermal conductivity once the specific heat capacity of the material is known. Seldom, Brillouin spectra contain additional low frequency excitations like magnons, plasmons, second sound *etc*.

Brillouin scattering is complimentary to the ultrasound technique used for studying the acoustical properties. It take place in the hypersonic frequency regime ($10^7$ $s^{-1}$ < ω < $10^{12}$ $s^{-1}$) of the vibrational energy spectrum. This frequency range is in between the frequency

ranges probed by ultrasonic and neutron scattering. Being a light scattering technique, Brillouin spectra is obtained by focussing monochromatic light on the sample and collecting the scattered light while the sample is in thermodynamic equilibrium. In addition to being a non contact and non destructive technique to estimate the elastic properties of materials, the major advantage of Brillouin spectroscopy is that you can perform experiments on small samples (few microns). Samples having diameter of few microns (20 - 50 μm) and as thin as 15 μm are sufficient for Brillouin spectroscopy experiments. Also experiments can be carried out on samples which are highly reactive or fragile and also under extreme physical conditions (temperature or pressure). The major disadvantage of Brillouin spectroscopy is the expensive experimental techniques required which consists of single mode monochromatic laser, Fabry-Pérot interferometer and associated controller units.

### 1.3.1. Principle of Brillouin scattering

In classical description of light scattering as described by Rayleigh, the electromagnetic field acts on charged particles in the medium which in turn will act as independent scatters which radiates light [1]. The major drawback of this theory was that it could not explain the experimentally observed scattering in all the directions. The oscillating electromagnetic field polarizes the medium, but the light scattered from different scatters are out of phase (different scatters are closer to each other by less than the wavelength of light) which results in destructive interference in all except in the forward direction. To explain the observed scattering in all the directions, Smoluchowski and Einstein introduced the concept that the light is scattered by the spatially correlated fluctuations of the dielectric constant of a material at finite temperature, which arises from the translational and rotational motion of particles [11,12].

In thermodynamic equilibrium, the fluctuations in the number density of atoms or particles as a function of position and time will be determined by their thermal motions. The fluctuations can be represented by,

$$N(r,t) = N + \Delta N(r,t) \tag{1.7}$$

where, $N$ is the average number density and $\Delta N(r, t)$ is its fluctuations and $r$ and $t$ are the position and the time. The interaction between the incident light and the particles acting as dipoles results in the Doppler shift of the scattered light. The wavevector and the

frequency of the incident light and the density fluctuations determine the wavevector and the frequency of the scattered light. The density fluctuations *ΔN(r, t)* can be represented in terms of wavevector $q$ and frequency ω by the Fourier transformations. The fluctuations in the number density *ΔN(ω, q)* thus obtained will have the wavelength, Λ

$$\Lambda = {}^{2\pi}/_{q} \tag{1.8}$$

and phase velocity, V

$$V = {}^{\omega}/_{q} \tag{1.9}$$

The density fluctuations can be considered as a diffraction grating for the incident light in comparison with Bragg's X-ray diffraction from the lattice planes. Thus using the Bragg's diffraction condition, we can obtain the relation

$$\lambda_I = 2\Lambda \sin\frac{\theta}{2} \tag{1.10}$$

where $\lambda_I$ (=$\lambda/n$) is the wavelength of the incident light in a medium of refractive index $n$ and $\lambda$ is the wavelength of the incident light in vacuum. The frequency shift can be then obtained as

$$\Delta\omega = \pm Vq = \pm 2\frac{2\pi}{\lambda} VnSin(\theta/2) \tag{1.11}$$

The coupling of light with the fluctuations in the medium can be represented by the fluctuating part of the dielectric tensor as

$$\varepsilon_{ij}(r,t) = \varepsilon_{ij} + \Delta\varepsilon_{ij}(r,t) \tag{1.12}$$

where, $\varepsilon_{ij}$ is the average dielectric tensor and $\Delta\varepsilon_{ij}(r,t)$ is its fluctuating part which couples with light. Fluctuations in $\varepsilon$ should be determined for calculating the Brillouin spectra.

### 1.3.2. Brillouin scattering in fluids

To calculate the intensity and the spectral features of Brillouin scattering in fluids, the appropriate value of the fluctuating part of the dielectric tensor Δε and its coupling with fluctuations in pressure, density, temperature or entropy needs to be determined. According to the thermodynamic approach, the fluctuating part of the dielectric tensor is characterised by its dependence on two parameters, pressure (P) and entropy (S) [13].

$$\Delta\varepsilon = \left(\frac{\partial\varepsilon}{\partial P}\right)_S \Delta P + \left(\frac{\partial\varepsilon}{\partial S}\right)_P \Delta S \tag{1.13}$$

The total intensity of the scattered electromagnetic field is proportional to the mean square fluctuations in ε which depends on the fluctuations in temperature (T) and density (ρ)

$$I_s = <|\Delta\varepsilon|^2> \tag{1.14}$$

$$|\Delta\varepsilon|^2 = \left(\frac{\partial\varepsilon}{\partial P}\right)_S^2 \frac{k_B T}{\beta_S V_0} + \left(\frac{\partial\varepsilon}{\partial T}\right)_P^2 \frac{k_B T^2}{\rho C_P V_0} \tag{1.15}$$

$k_B$ is Boltzmann's constant, $\beta_S$ is the isentropic compressibility, $C_P$ is the specific heat at constant pressure and $V_0$ is the volume at ambient pressure. The first term on the right side of Eq. 1.15 represents the Brillouin doublets of frequencies $\omega_B = \omega_i \pm \omega_s$ ($\omega_B$ is the frequency of the Brillouin spectral feature, $\omega_i$ and $\omega_s$ are the frequencies of the incident and the scattered photons) which results from the scattering of light from the isentropic pressure fluctuations (*i.e.*, acoustic waves) and the second term represents the component resulting from the isobaric (non-propagating) entropy fluctuations which is not shifted in frequency. The ratio of the intensity of the Rayleigh component ($I_C$) to the sum of the two Brillouin components ($I_B$) is called Landau-Placzek ratio and is given by

$$\frac{I_C}{I_B} = \left(\frac{\partial\varepsilon}{\partial P}\right)_S^2 \left(\frac{\partial\varepsilon}{\partial T}\right)_P^{-2} \approx \frac{C_P - C_V}{C_V} = \frac{\beta_T - \beta_S}{\beta_S} \tag{1.16}$$

$C_P$ and $C_V$ are the specific heat at constant pressure and volume and $\beta_S$ and $\beta_T$ are the isentropic and isothermal compressibility.

Hydrodynamic approximation represents the spectrum in a complete manner as it includes the dynamics of the fluctuations that affect the spectral line shape also, which cannot be captured by the thermodynamic approach. In this approximation, the spectrum can be represented as [13]

$$S(\omega, q) \propto \frac{C_P - C_V}{C_V}\left[\frac{2D_T q^2}{D_T + \omega^2}\right] + \left[\frac{\Gamma q^2}{(\Gamma q^2)^2 + (\omega + Vq)^2} + \frac{\Gamma q^2}{(\Gamma q^2)^2 - (\omega + Vq)^2}\right] \tag{1.17}$$

where, $D_T$ is the thermal diffusivity. The first term in the right side represents the central component and the second term represents the two Brillouin peaks of full width at half maximum (FWHM) $\Gamma q^2$, where Γ is the acoustic absorption coefficient.

### 1.3.3. Brillouin Scattering in solids

For wavelengths that are not infinite but larger compared to the primitive cell dimensions, the acoustic modes in a crystal lattice behave like sound waves in a continuous medium and their properties can be derived from the macroscopic elasticity theory. In the long wavelength limit, the equation of motion of the atomic displacement in comparison with that of an elastic continuum is

$$\rho \frac{\partial^2 u_{i\,(r,t)}}{\partial t^2} = C_{ijkl} \frac{\partial^2 u_{k\,(r,t)}}{\partial x_j \partial x_i} \tag{1.18}$$

where, $C_{ijkl}$ is the stiffness tensor and $u_i$ represents the atomic displacement from the equilibrium position. Assuming plane wave solutions of the form

$$u_i = u_i^0 expi(qr - \omega t) \tag{1.19}$$

we obtain from Eq. 1.18

$$\left(C_{ijkl} q_j\, q_l - \rho\omega^2 \delta_{ik}\right) u_k^0(q,\omega) = 0 \tag{1.20}$$

where, $q_j$ are the components of the scattering wavevector, $\delta_{ik}$ is the Kronecker delta function and $u_k^0$ is the polarization. This equations has non-trivial solutions that satisfy the secular equation

$$\left|C_{ijkl} q_j\, q_l - \rho\omega^2 \delta_{ik}\right| = 0 \tag{1.21}$$

This equation has three solutions for each direction of $q$, corresponding to the three phonon branches. For $q$ along high symmetry directions we have displacement vectors parallel and perpendicular to $q$, corresponding to one pure longitudinal and two pure transverse acoustic modes. The displacement vectors are mixed in a general direction in an anisotropic medium and the vibrations consists of one quasi longitudinal and two quasi shear modes.

The spectral intensity $I_s$ is proportional to the mean square of the fluctuating part of the dielectric tensor and can be given as

$$I_s \propto (\mathrm{e^s})^2 . < |\Delta\varepsilon|^2 > . (\mathrm{e^i})^2 \tag{1.22}$$

where, $e_i$ and $e_s$ are the polarizations of incident and scattered light. In a direction $q$, the intensity of $\alpha^{th}$ acoustic mode of acoustic velocity $V^{\alpha}$ is given by

$$I_s = I_i \frac{k_B T \pi^2 V_0}{2\lambda_s^4 \rho (V^\alpha)^2 r^2} \frac{n_s}{n_i} [e_s . \mathbf{T}^\alpha . e_i]^2 \quad (1.23)$$

where, $I_i$ is the intensity of incident light, $V_0$ is the scattering volume, $n_i$ and $n_s$ are the refractive indices of medium in the incident and scattered directions, $\lambda_s$ is the wavelength of the scattered light in vacuum, $r$ is the distance of observation from the scattering volume and $\mathbf{T}^\alpha$ is a tensor which represents the fluctuations in the dielectric tensor. The following sections give a brief overview on the different features of Brillouin spectroscopy measurements, depending on the opacity of the materials.

## (a) Transparent materials

Intensity of the Brillouin spectra from the transparent samples are higher compared to that of opaque samples due to the high scattering volume they provide. Moreover, scattering geometry for transparent materials can be selected anywhere between 0º and 180º. Among the different scattering geometries which can be used, the platelet geometry (Fig. 1.5 (a)) has the advantage that it does not require the knowledge of the refractive index of the sample [14]. A combination of platelet geometry and any other geometry can be used to derive the refractive index of the material [14]. The presence of dislocations and fractures in the samples can increase the elastic scattering from the sample which can mask the weak Brillouin spectral features. Hence, optically clear samples can facilitate the Brillouin scattering measurements.

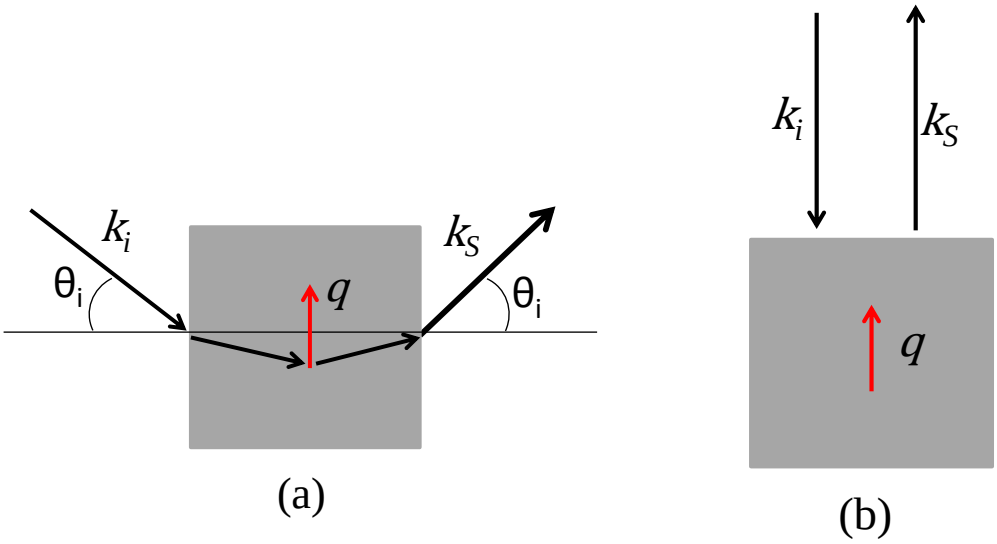


Fig. 1.5. Schematic of (a) platelet and (b) back scattering geometries.

## (b) Opaque materials

Due to the high optical absorption, opaque materials are characterised by a complex refractive index η = n + iκ. As a result of the high optical absorption, the intensity of scattered light decreases exponentially inside the medium and the scattering volume will be confined close to the sample surface, which influences the wave vector conservation rules. In the presence of optical absorption, the wave vector transfer $K = k_s - k_i$ becomes complex and can be represented using the real (K′) and imaginary (K″) parts as

$$K = K' - iK'' \tag{1.24}$$

Assuming that $K$ is perpendicular to the sample surface, the $q$ dependence of scattered intensity can be represented by [15]

$$\frac{dP}{d\omega} \sim \frac{1}{(q - K')^2 + K''^2} \sim \frac{1}{(q/(k - 2n)^2 + 2\kappa''^2} \tag{1.25}$$

Eq. 1.25 shows that in the presence of optical absorption, the phonon wavevector $q$ is not uniquely defined as all the phonons within a range $\Delta q \sim K''$ around the value $q = K'$ may scatter the light in the direction of $\boldsymbol{k}_s$. For acoustic phonons, the phonon energy is proportional to the wavevector with the peak position at $\omega = 2nVk_i$. In the presence of optical absorption, the Brillouin peak position remains same but FWHM (Γ) broadens with a value given by

$$\Gamma = 4Vk_i\kappa \tag{1.26}$$

The broadening effect was experimentally first observed in CdS and was convincingly demonstrated in Si and Ge by Sandercock [16,17].

Experimental results in the backscattering geometry (Fig. 1.5(b)) on opaque samples shows asymmetry and frequency shift of the Brillouin peaks. These effects can be attributed to the coherent reflection of the phonons at the surface. The asymmetric lineshape is because $q$ and $-q$ contribute to both Stokes and anti-Stokes processes whereas in transparent materials, each contributes only to one of the two processes. The shifted peak position in this case is given by

$$\omega = 2k_iV(n^2 + \kappa^2)^{1/2} \tag{1.27}$$

### (c) Surface Brillouin scattering

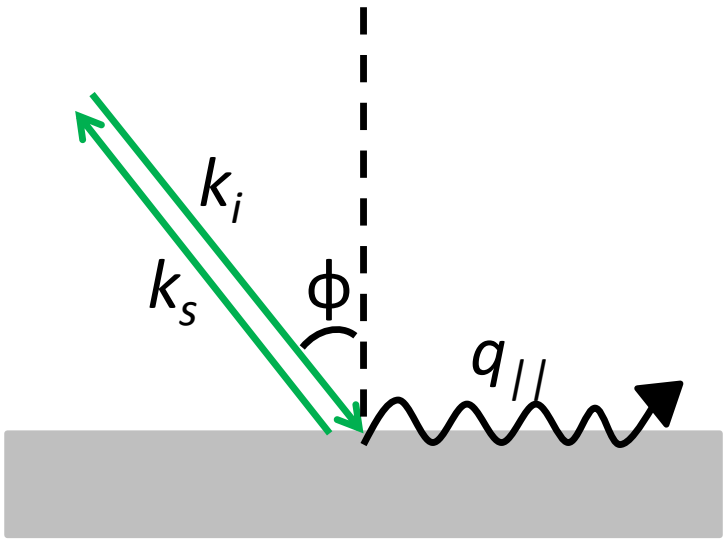


Fig. 1.6. The scattering of light from an opaque sample for oblique incidence in backscattering geometry.

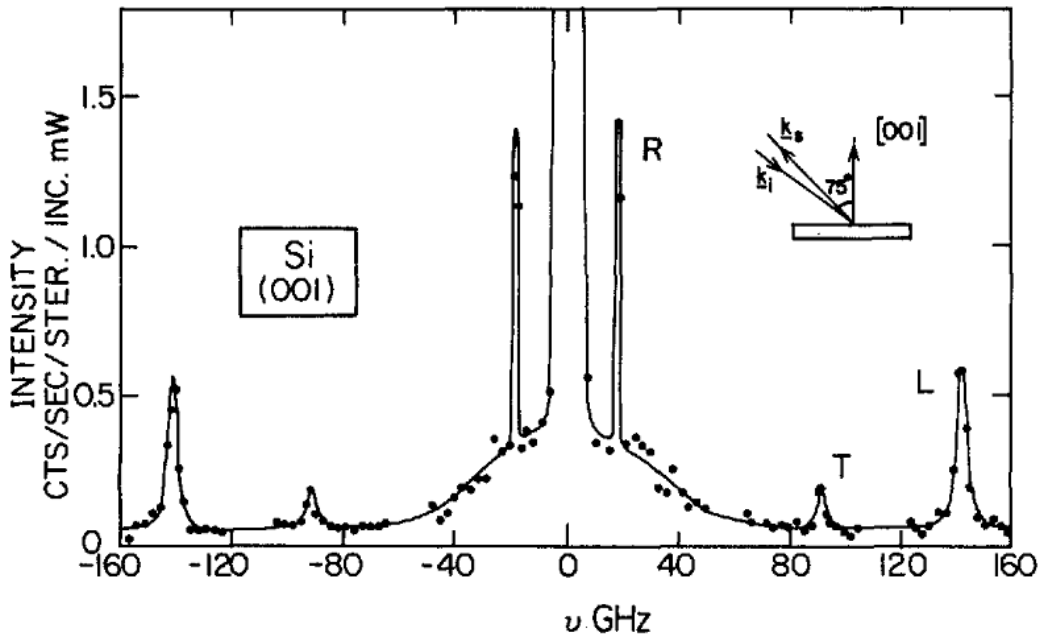


Fig. 1.7. The Brillouin spectra of silicon showing the surface Rayleigh wave (R) and the bulk Brillouin modes (L and T). The central unshifted peak is also observed. (Adopted from Ref. [18])

The ripple scattering or surface scattering (as shown in Fig. 1.6) is a dominant scattering mechanism in opaque materials which generates new modes in the Brillouin spectra. For less opaque materials, ($\kappa < n$) normal elasto-optic contributions will be dominant.

Surface acoustic waves originate from the propagation of elastic energy along the surface of elastic solids. It is also known as Rayleigh waves and typically almost all energy will be localized within a depth of two wavelengths [19]. The surface ripples behave like a moving grating and diffract the incident light *via* Doppler effect without invoking any modulation of the dielectric constants in the interior of the material. The surface Rayleigh wave produces sharp and pronounced peak for any propagation direction. The Brillouin spectrum of Silicon which contains the bulk Brillouin peaks, surface Rayleigh wave and the central unshifted peak is shown in Fig. 1.7.

Generally backscattering geometry with an oblique incidence angle, $\phi$ is used for studying the scattering from surfaces of sample. The phonon wavevector in this case can be derived from Fig. 1.6 as

$$q_{||} = 2ksin\phi \tag{1.28}$$

where, $\phi$ is the angle between incident and scattered wavevector with respect to the normal of the surface. In addition to the usual surface Rayleigh wave, we can also encounter several other surface features like pseudo surface, Lamb, Love, Sezawa, Stonely waves *etc*., of which few are specific only for thin films or scattering from interfaces [15,20-23].

### 1.3.4. Elastic constants for cubic crystals

Though it is frequently assumed that the elastic properties of materials are isotropic, they rarely are. In single crystals the elastic properties changes with different directions. According to the Hooke's law, relation between stress (σ) and strain (ε) in a linear elastic medium can be written as [24-28]

$$\sigma_{ij} = C_{ijkl}\varepsilon_{kl} \text{ where i, j, k, l = 1, 2, 3} \tag{1.29}$$

$C_{ijkl}$ is called elastic *stiffness tensor* and it has 81 components. Alternatively strain can be expressed in terms of stress as $\varepsilon_{ij} = S_{ijkl}\sigma_{kl}$ where, $S_{ijkl}$ is a fourth order tensor and the individual elements are called compliances.

The stress and strain tensors are symmetric, resulting in the reduction of the number of independent quantities in $C_{ijkl}$ and $S_{ijkl}$ to 36. Voigt notation can be used to simplify the representation of the stiffness/compliance tensor. According to Voigt representation, the element $C_{ijkl}$ can be written as $C_{IJ}$ (I, J= 1, 2, 3) which is a 6x6 matrix. For a cubic

crystal there will be only three independent elastic constants *viz*, $C_{11}$, $C_{12}$ and $C_{44}$. The stiffness tensor for cubic crystal is given as:

$$\begin{pmatrix} C_{11} & C_{12} & C_{12} & 0 & 0 & 0 \\ C_{12} & C_{11} & C_{12} & 0 & 0 & 0 \\ C_{12} & C_{12} & C_{11} & 0 & 0 & 0 \\ 0 & 0 & 0 & C_{44} & 0 & 0 \\ 0 & 0 & 0 & 0 & C_{44} & 0 \\ 0 & 0 & 0 & 0 & 0 & C_{44} \end{pmatrix}$$

The relation between the acoustic velocities and elastic constants in certain high symmetry directions in a cubic crystal is given in Table 1.1 [24,25]. Determination of the elastic constants from the Brillouin experiments will be easier if the experiments are performed on crystals where *q* is chosen along the high symmetry directions.

For crystals with cubic symmetry, the degree of elastic anisotropy can be represented using the 'Zener ratio' or 'Anisotropic factor', A. The anisotropic factor for a cubic crystal can be defined by the ratio of two extremes of shear coefficients, $C_{44}$ and $(C_{11}-C_{12})/2$.

$$A = \frac{V_{TA2}^2}{V_{TA1}^2} = \frac{2C_{44}}{C_{11} - C_{12}} \tag{1.30}$$

The anisotropic factor, A can be greater or lesser than unity. A=1 in the case of isotropic materials. When A is less than 1, the crystal is stiffest along <100> direction and when A is greater than 1 it is stiffest along <111> direction. *i.e.*, for A<1, $V_{LA}$ will be maximum along the <100> direction and minimum along <111> direction and also $C_{44}$ will be less than $(C_{11}-C_{12})/2$. The opposite happens when A is greater than 1. The relation between the compliance and elastic constants can be written as

$$S_{11} = \frac{C_{11} + C_{12}}{(C_{11} - C_{12})(C_{11} + 2C_{12})} \tag{1.31}$$

$$S_{12} = \frac{-C_{12}}{(C_{11} - C_{12})(C_{11} + 2C_{12})} \tag{1.32}$$

$$S_{44} = \frac{1}{C_{44}} \tag{1.33}$$

The Young's modulus, *E* along different directions can be obtained from the relation

$$\frac{1}{E} = S_{11} + (2S_{12} - 2S_{11} + S_{44})\frac{h^2k^2 + k^2l^2 + h^2l^2}{(h^2 + k^2 + l^2)^2} \quad (1.34)$$

where, *h*, *k* and *l* are the direction indices. For isotropic materials, $2(S_{12}-S_{11}) = S_{44}$ (*i.e.*, only one TA mode will be present) and E will be independent of direction.

Table. 1.1. The velocities of acoustic modes in high symmetry directions for cubic space group.

| Direction of | $V_{LA}^2$ Longitudinal | $V_{TA2}^2$ Transverse | $V_{TA1}^2$ Transverse |
|---|---|---|---|
| <001> | $C_{11}/\rho$ | $C_{44}/\rho$ | $C_{44}/\rho$ |
| <110> | $(2C_{44}+C_{11}+C_{12})/2\rho$ | $C_{44}/\rho$ | $(C_{11}-C_{12})/2\rho$ |
| <111> | $(4C_{44}+2C_{12}+C_{11})/3\rho$ | $(C_{44}+C_{11}-C_{12})/3\rho$ | $(C_{44}+C_{11}-C_{12})/3\rho$ |

## 1.3.5. Central peaks

The quasi-elastic light scattering (QELS) or the central peak (CP) phenomenon gives rise to the central unshifted peaks in the Brillouin spectrum. It has attracted considerable interest recently in dielectrics, due to its relationship with the critical behaviour near second-order phase transitions [29]. QELS can originate due to various reasons and often one or more of these could be present simultaneously. Though QELS is often associated with critical phenomena and has been observed in the materials that exhibit phase transitions, it is also observed in materials which are considered to be unrelated to phase transitions, for example silicon, diamond, $TiO_2$ *etc* [30-33]. The Brillouin spectra in these cases often consist of two QELS components: QES-I (or narrow central peak, NCP) and QELS-II (or broad central peak, BCP). The Brillouin spectra showing the central peaks in $TiO_2$ is given in Fig. 1.8.

When the temperature of the crystal is high, the number of phonons will be large and the phonons collide frequently while the local thermal equilibrium will be well established. The incident light in this case is considered to be scattered by the fluctuations in temperature or entropy and results in a diffusive Rayleigh central peak. This regime where the heat transport theory is valid can be referred to as the “collision-dominated” or “hydrodynamic phonon regime.” When phonons rarely collide, (usually at low temperatures) phonon transport theory is no longer valid and temperature or entropy

cannot be defined locally. Non-thermodynamic scattering processes are taken into account in this case and light is considered to be scattered as a consequence of simultaneous creation and annihilation of a few phonons (two phonon difference light scattering). This region is referred to as "collisionless phonon regime" or "ballistic regime".

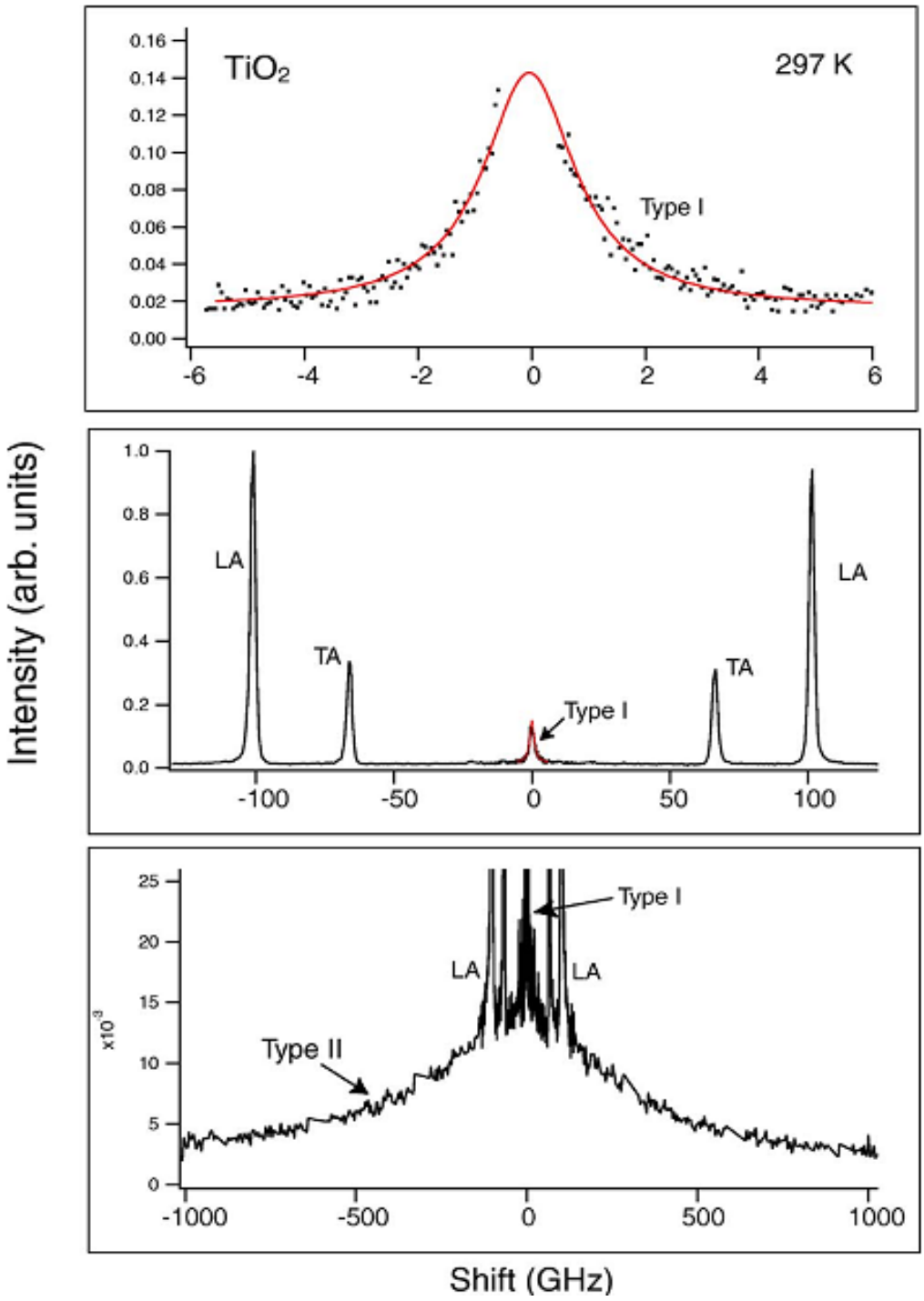


Fig. 1.8. The Brillouin spectra of QELS in $TiO_2$. Type I and Type II refers to NCP and BCP respectively. (Adopted from Ref. [32])

In the hydrodynamic regime, the entropy fluctuations give rise to NCP. The linewidth or half width at half maximum (HWHM) of NCP in the hydrodynamic regime is given by $\Gamma_{NCP} = D_{th}q^2$, where $D_{th}$ is the thermal diffusivity. At low temperatures, linewidth do

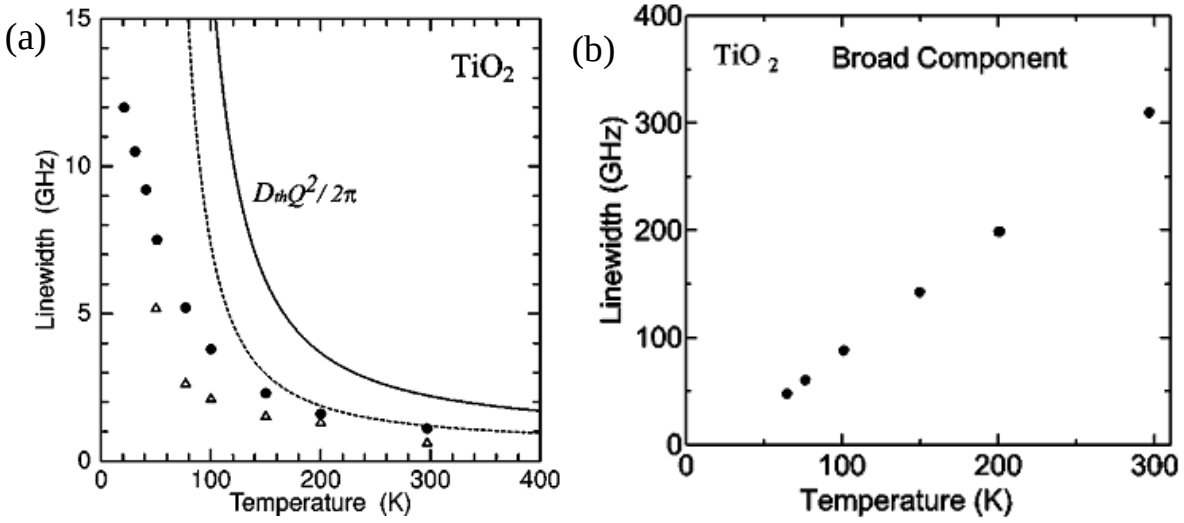


Fig. 1.9. The temperature dependence of the linewidth (half width at half maximum) for (a) NCP and (b) BCP in $TiO_2$. The circles and the triangles in (a) are the measured linewidths for 180° and 90° scattering, respectively. The solid and broken lines represent the theoretical $D_{th}q^2$ for 180° and 90° scattering geometries, respectively. (Adopted from Ref.[33])

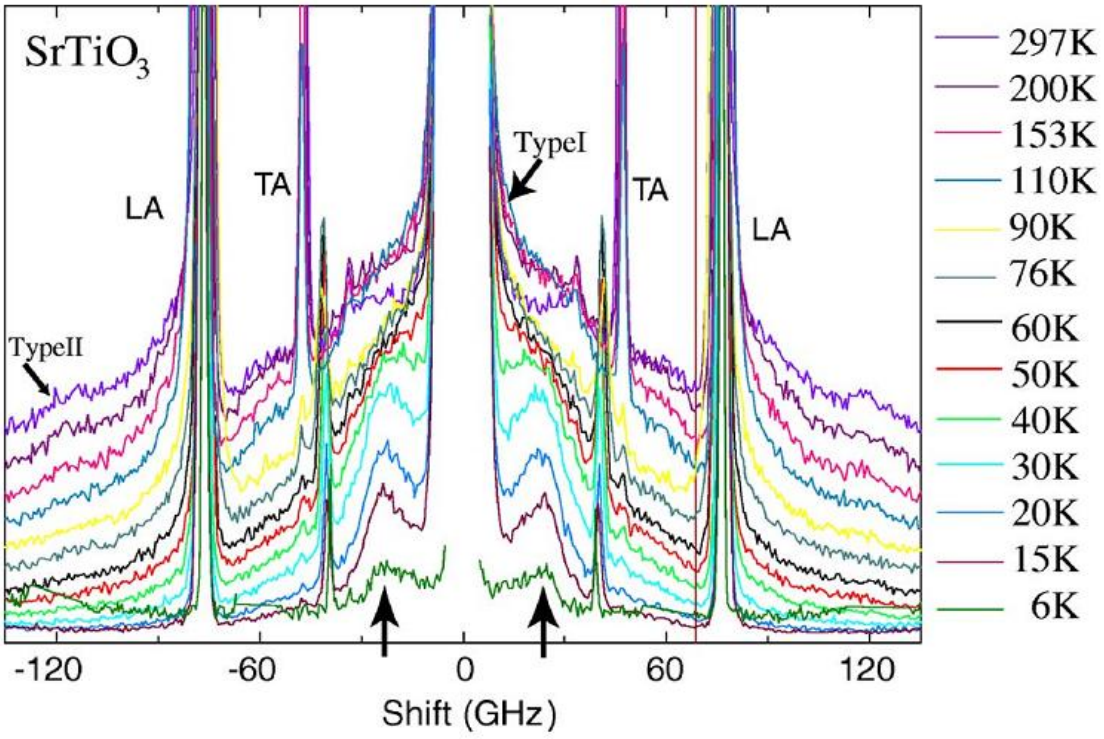


Fig. 1.10. The temperature dependent evolution of second sound (upward arrows) from NCP (Type I) in $SrTiO_3$. (Adopted from Ref. [32])

not follow $D_{th}q^2$ and the origin of NCP can be credited to two phonon difference scattering where two phonons from a single phonon branch participate. Thus, NCP at high temperature exhibits $q^2$ dependence while at low temperature it depends linearly on $q$. The exact reason for the origin of BCP is not clearly understood yet, but it can be explained qualitatively by two phonon difference scattering where phonons from different phonon branches participate. BCP do not show $q$ dependence and its width decreases on decreasing the temperature. On cooling, the linewidth of NCP broadens while BCP narrows and they become indistinguishable in the ballistic regime. It is also observed that the linewidth of the NCP do not extend beyond the Brillouin peaks while the linewidth of BCP extends beyond the Brillouin peaks, often coupling with them and resulting in their asymmetric lineshape. The temperature dependence of linewidth for NCP and BCP in $TiO_2$ is shown in the Fig. 1.9.

In addition to these two quasielastic components, the low frequency light scattering spectra seldom contains extra sound like peak called second sound [34,35]. The second sound is a wave like propagation of heat and it is seen only in very few materials like $SrTiO_3$, solid helium, NaF *etc* [36-38]. Second sound was first observed in the Brillouin spectra by Hehlen *et al.* in $SrTiO_3$, where a broad doublet was seen emerging from the NCP at low temperatures [36]. *i.e.*, the NCP centered at zero frequency shift develops into two shifted Brillouin peaks at low temperatures, as the thermal wave becomes under damped. Figure 1.10 shows the Brillouin spectra of $SrTiO_3$ showing the emergence of second sound from NCP.

The phonon collisions play an important role in the origin of central peaks and second sound. The phonon collisions in a material can take place by (1) normal and (2) resistive relaxation process [39]. Normal process is a phonon collision in which the total initial and final crystal momenta are equal, while for umklapp or resistive process they differ by a nonzero reciprocal lattice vector, $K_0$ (Fig. 1.11). Umklapp process is responsible for thermal resistivity at high temperature and its absence can result in infinite thermal conductivity in an insulating crystal.

The reciprocal number of collision frequency over a characteristic length is called as "Knudsen number", Kn [40]. The characteristic length scale in light scattering experiments is reciprocal of $q$ and hence the Knudsen number for a phonon gas can be defined as

$$Kn = ql = qc\tau \tag{1.35}$$

where, $l$ is the mean free path and $\tau$ is the relaxation time. The relaxation time and the Knudsen number for the normal and resistive process can be denoted as $\tau_N$, $\tau_R$ and $Kn_N$, $Kn_R$. The hydrodynamic regime, where we can observe thermal diffusion or second sound exist for the condition, $Kn_N << 1$ or $Kn_R << 1$. When $Kn_N >> 1$ or $Kn_R >> 1$ we have collisionless or ballistic regime. A schematic of the various phonon regimes and Knudsen number is given in Fig. 1.12.

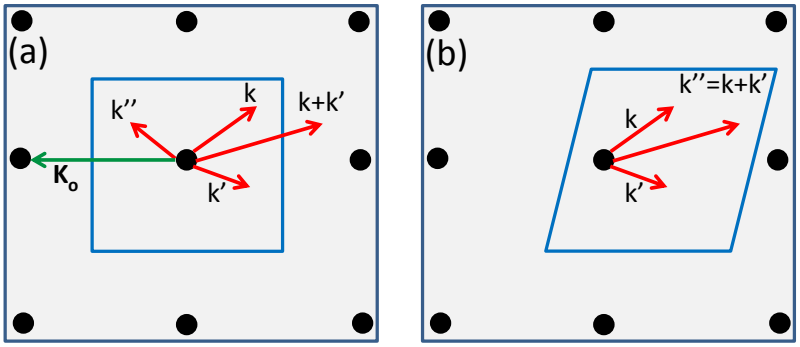


Fig. 1.11. The schematic representation of (a) umklapp and (b) normal processes. The points are reciprocal lattice points and the square region in (a) and parallelogram in (b) represents the first Brillouin zone. k and k′ are wavevector of phonons which are allowed to merge into a single wavevector k″. Umklapp process occurs if k″ differs from k + k′ by a non zero reciprocal lattice vector, $K_0$ while normal process occurs when k″= k + k′.

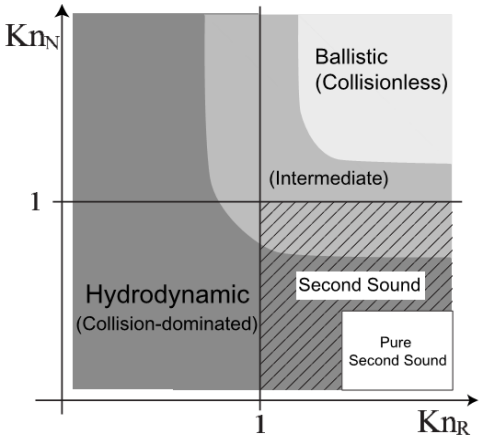


Fig. 1.12. The phonon regimes for different values of Knudsen number, $Kn_N$ and $Kn_R$. (Adopted from Ref. [40])

Second sound propagates only when the condition $Kn_N << 1$ or $Kn_R << 1$ is satisfied. This is well known as the “window condition” which can be expressed as [34]

$$\tau_R^{-1} \ll \omega_0 \ll \tau_N^{-1} \tag{1.36}$$

The QELS and second sound can be explained by the "extended thermodynamic" equations which is applicable in hydrodynamic as well as collisionless regimes [40]. According to this approach, the Brillouin spectrum of second sound and BCP is given by the expression

$$S(q,\omega) = A\frac{2{\omega_0}^2\Gamma_{ss}}{(\omega^2-{\omega_0}^2)^2+4\omega^2{\Gamma_{ss}}^2} + B\frac{\Gamma_2}{\omega^2+\Gamma_2^2} \tag{1.37}$$

The first part here corresponds to the spectrum of a damped harmonic oscillator representing the second sound and the second part corresponds to the BCP. $\omega_0 = V_D q/\sqrt{3}$ is the natural frequency of phonon gas ($V_D$ is the Debye mean velocity) and $\Gamma_{SS}$ is the linewidth of the second sound. A and B are constants and $\Gamma_2$ is the linewidth of BCP. The linewidth of second sound is represented by

$$\Gamma_{ss} = \frac{2}{5}{\omega_0}^2\tau_N + \frac{1}{2\tau_R} \tag{1.38}$$

and frequency can be determined from the formula

$$\omega_{SS} = \sqrt{\omega_0^2 - 2\Gamma_{ss}^2} \tag{1.39}$$

When $\Gamma_{SS} > \omega_0$, the second sound is over damped and cannot propagate resulting in the NCP, which is encountered in most materials. The NCP spectra can be then written as

$$S(q,\omega) = \frac{\Gamma_{th}}{\omega^2+\Gamma_{th}^2} \tag{1.40}$$

The linewidth of NCP is given by

$$\Gamma_{th} = D_{th}q^2 \tag{1.41}$$

where, $D_{th}$ is the thermal diffusivity which can be estimated from the relation

$$D_{th} = \frac{1}{3}{V_D}^2\tau_R \tag{1.42}$$

$D_{th}$ depends on the thermal conductivity by

$$D_{th} = \frac{\kappa}{\rho C} \tag{1.43}$$

where $\kappa$, $\rho$ and $C$ are the thermal conductivity, density and heat capacity respectively. The thermal conductivity of a three dimensional material can be expressed as

$$\kappa = \frac{1}{3} C V_D l = \frac{1}{3} C {V_D}^2 \tau \tag{1.44}$$

The spectra of broad central peak can be written as

$$S(q, \omega) = \frac{\Gamma_2}{\omega^2 + \Gamma_2^2} \tag{1.45}$$

The linewidth of BCP, $\Gamma_2$ is equal to the phonon collision rate

$$\Gamma_2 = \frac{1}{\tau} = \frac{1}{\tau_N} + \frac{1}{\tau_R} \tag{1.46}$$

Here, $\tau$ is the average relaxation time of the whole thermal phonons in the Brillouin zone and hence it is considered to be independent of the frequency and wave vector of thermal phonons, thus accounting for the $q$ independent behaviour of BCP. The decrease in the linewidth of BCP on decreasing the temperature can be explained by the increase in $\tau$ as the temperature is reduced.

## 1.4. Raman scattering

Raman scattering is an important tool which provides valuable information about the lattice and molecular vibrations. Raman scattering is associated with optical phonons while acoustic phonons participate in the Brillouin scattering. The phonon frequencies, scattering intensities and the selection rules deduced from Raman spectra provides information about the crystal structure, bonding character, phase transitions *etc.* The Raman scattering process involves the following steps:

1. Photon-electron interaction: An incident photon excites the electron from ground state to an intermediate or virtual energy state by creating an electron-hole pair.
2. Electron-phonon or hole-phonon interaction: the intermediate state goes to another state of lower energy (Stokes) or higher energy (anti-Stokes) by creation or annihilation of phonon.
3. Electron-photon interaction: The electron-hole pair recombines by emission of the Raman scattered photon.

The origin of Raman effect can be explained by classical theory. When an oscillating electric field, $E = E_0 e^{i\omega_0 t}$ of an electromagnetic radiation is incident on a crystal, a polarization is induced in the crystal. The induced electric polarization in any specific direction is given by

$$P_i = \chi_{ij} E_j \tag{1.47}$$

where $\chi_{ij}$ is the susceptibility tensor (for molecules polarizability ($\alpha_{ij}$) tensor has to be considered instead of susceptibility). The susceptibility becomes altered as the atoms in the solid are vibrating periodically around their equilibrium positions. The scattered light can be then described as the oscillation of an ensemble of dipoles and the Raman intensity can be expressed by

$$I_s = I_i \frac{\omega_s^2 V}{(4\pi\varepsilon\varepsilon_0)^2 c^4} [e_s . \chi . e_i]^2 \tag{1.48}$$

For a phonon vibrating at a frequency $\Omega_j$, component of susceptibility tensor can be expressed as

$$\chi_{ij} = \chi_{ij}^{(0)} + \sum \frac{\partial \chi_{ij}}{\partial Q_k} Q_k + \frac{1}{2} \sum \left( \frac{\partial^2 \chi_{ij}}{\partial Q_k \partial Q_l} \right) Q_k Q_l + \ higher\ order\ terms \tag{1.49}$$

$Q_j = Q_0 e^{\pm i\Omega_j}$ is the atomic displacement associated with a phonon of wavevector $q$ and frequency Ω. The induced polarization is given by

$$P_i = \chi_{ij}^{(0)} E_{0j} e^{i\omega_i t} + E_{0j} Q_0 \sum \frac{\partial \chi_{ij}}{\partial Q_k} e^{i(\omega_i \pm \Omega_j)t} + \frac{1}{2} E_{0j} Q_0^2 \sum \left( \frac{\partial^2 \chi_{ij}}{\partial Q_k \partial Q_l} \right) e^{i(\omega_i \pm \Omega_j \pm \Omega_l)t} + \ higher\ order\ terms \tag{1.50}$$

This expression corresponds to oscillating dipoles re-radiating light at frequencies,$\omega_0$, $\omega_0 - \Omega_j$ (Stokes) and $\omega_0 - \Omega_j$ (anti-Stokes).

## 1.5. Pressure and Temperature

Pressure and temperature are two thermodynamic variables which determine the material properties. When subjected to a change in these two variables, materials undergo several changes including phase transitions. Physical properties of materials has to be studied for different temperature and pressure in view of preparing materials which exhibits an expected property in a specific thermal (temperature) and mechanical pressure (stress) environment. On increasing the pressure the atoms of materials form closely packed structure, while increasing the temperature results in less ordered structures which may even result in the disruption of chemical bonds. The primary function of pressure and temperature dependent experiments is to study and understand the properties of material around us. Pressure/temperature can also be used to synthesise new and technologically

interesting materials which do not exist naturally, for example super-hard materials. We can also study the electrical, magnetic and other properties at extreme pressure and temperature to test the validity of many theoretical studies which predicts many novel material properties under the application of external stresses.

Pressure is a cleaner and stronger perturbation than the temperature. For example, in silicon a volume change of 5 % is obtained on applying a pressure of 10 GPa whereas temperature induced volume change from 0 K to melting is only ~1.8 %. Also temperature is complicated by the parallel action of anharmonic effects or thermal expansion. The frequencies of the phonons in materials changes on applying pressure or temperature, enabling the inelastic light scattering techniques to probe their effects. The shift in the Brillouin/ Raman peaks as well as their FWHM yields several useful information regarding their structure, phase transitions, lifetimes *etc.*

### 1.5.1. High pressure Brillouin spectroscopy

Brillouin spectroscopy is a good tool to study the elastic properties of materials at high pressure/temperature. Major advantage of Brillouin spectroscopy is that, samples of small dimensions (microns) can be probed. This enables experiments to be performed on wide variety of materials, which includes samples important in the field of biology, geophysics, material science, condensed matter *etc* [13]. Sometimes, using Brillouin spectroscopy is complicated due to the fact that inside a cryostage or inside a diamond anvil cell (DAC), parasitic diffuse scattered light from different parts of the sample container masks the weak Brillouin peaks. Moreover in DAC the sample peaks can have interference from the hydrostatic medium or the peaks of diamond. Also transparent samples are required for high pressure Brillouin studies [14]. Nevertheless, Brillouin spectroscopy has emerged as an important tool to study the anisotropic elastic properties of materials at extreme pressures and temperatures.

A combination of Brillouin scattering and X-ray diffraction (which determines the density) enables us to determine the pressure dependent mechanical properties of materials. Using platelet geometry can help us to determine the elastic constants without the knowledge of the pressure dependence of refractive index. For anisotropic crystals, the orientation of the sample within the DAC should be known for determining the elastic constant using Brillouin spectroscopy. If the crystal orientation is unknown as in the case

of solid noble gases, and other molecular solids, two approaches can be used to derive the elastic constants [14]:

1. Envelope method
2. Rotation method

In the envelope method the pressure dependence of acoustic velocities are determined for unknown directions and the envelope of such a data (from many sets of experiment) corresponds to the extreme values of acoustic velocity, which occurs along certain high symmetry directions. In most cases, all the three acoustic modes will not be visible in the Brillouin spectra. For example, in backscattering geometry TA modes will not be observed or it could very weak and only LA modes will be present in the spectra. In such cases when only LA is seen, the extreme values of LA and the isothermal bulk modulus can be used to determine the adiabatic elastic constants [41]. The major limitation of this technique is the error which can arise due to the assumption that the lower and upper bounds of the acoustic velocities are really achieved and using isothermal bulk modulus instead of adiabatic bulk modulus for determining elastic constants [41,42]. If we can find the extremes of LA and one of the TA, the confidence with which we can determine the acoustic velocity and hence the elastic constants can be improved when compared to the envelope method which uses only the lower and upper bounds of LA and isothermal bulk modulus [43]. The rotation method is carried out by finding the angular dependence of the Brillouin shift of sample inside the DAC by rotating the crystal around the load axis and fitting the obtained velocity curve using modified Every's velocity expression as proposed by Shimizu and Sasaki [44].

## 1.6. Scope of the present investigations

We have used Brillouin spectroscopy to study the elastic properties, phase transitions, and second sound at ambient and extreme conditions in different materials. Four different materials are studied in this thesis:

1. ZIF-8: The influence of guest, temperature and pressure on the elastic properties of the metal organic framework, ZIF-8 is studied.
2. Carbon nanotubes: We have observed the phenomena of second sound in carbon nanotubes and have studied their temperature dependence. We have also determined

the temperature dependence of thermal conductivities from the two central peaks observed.

3. Pyrrolidinium based ionic liquids: We have investigated the temperature dependence of the acoustic velocities during phase transition for a series of pyrrolidinium based ionic liquids.
4. $Dy_2Ti_2O_{7:}$ Pressure dependence of the elastic properties of a pyrochlore, $Dy_2Ti_2O_7$ across phase transition is also investigated.

Raman spectroscopy has been also used to probe the changes in the local structure whenever required in few of the chapters.

## 1.7. Bibliography

[1] R. L, Philos Mag **47**, 375 (1899).

[2] G. Mie, Ann. Phy. **25**, 377 (1908).

[3] B. L, Annalen der Physik (Paris) **17**, 88 (1922).

[4] M. LI, J Russian Phys Chem Soc **58**, 381 (1926).

[5] G. E, Z Phys A **63** (1930).

[6] A. Smekal, Die Naturwissenschaften **11**, 873 (1923).

[7] K. S. K. C. V Raman, Nature **121**, 501 (1928).

[8] C. V. Raman, Nature **121**, 619 (1928).

[9] C. V. Raman, Indian J. Phys. **2**, 387 (1928).

[10] L. I. M. G. S. Landsberg, Naturewiss **16**, 557 (1928).

[11] S. M, Ann Phys **22**, 205 (1908).

[12] E. A, Ann Phys **33**, 1275 (1910).

[13] Sergio Speziale, Hauke Marquardt, and T. S. Duffy, Reviews in Mineralogy & Geochemistry **78**, 543 (2014).

[14] A. Polian, Journal of Raman Spectroscopy **34**, 633 (2003).

[15] J. R. Sandercock, *Light scattering in solids III* (Springer, 1982), Vol. 51, p. 187.

[16] A. S. Pine, Physical Review B **5**, 3003 (1972).

[17] J. R. Sandercock, Physical Review Letters **28**, 237 (1972).

[18] J. R. Sanderocock, Solid State Communications **26**, 547 (1978).

[19] L. Rayleigh, London. Math. Soc. Proc. **17**, 4 (1887).

[20] H. Lamb, Proc. R. Soc. London **93**, 114 (1917).

[21] A. E. H. Love, *Some problems in geodynamics* (Cambridge University Press, 1911).

[22] K. Sezawa, Bull. Earthquake REs. Inst **3**, 1 (1927).

[23] R. Stoneley, Proc. R. Soc. London A **232**, 447 (1955).

[24] K. Fritch, Ph.D thesis, Massachusetts institute of technology, 1965.

[25] W. Hayes and R. Louden, *Scattering of light by crystals* (John Wiley & sons, New York, 1978), p. 337.

[26] R. E. Newnham, *Properties of materials* (Oxford University press,. New York, 2005).

[27] W. F. Hosford, *Mechanical Behavior of Materials* (Cambridge University Press, New York, 2005).

[28] B. A. Auld, *Acoustic fields and waves in solids* (John Wiley & Sons, Inc., United States of America, 1973).

[29] J.-H. Ko, T. H. Kim, K. Roleder, D. Rytz, and S. Kojima, Physical Review B **84**, 094123 (2011).

[30] M. W. Anderson, S. M. Lindsay, and R. T. Harley, Journal of Physics C: Solid State Physics **17**, 6877 (1984).

[31] H. E. Jackson, R. T. Harley, S. M. Lindsay, and M. W. Anderson, Physical Review Letters **54**, 459 (1985).

[32] A. Koreeda, T. Nagano, S. Ohno, and S. Saikan, Physical Review B **73**, 024303 (2006).

[33] A. Koreeda, M. Yoshizawa, S. Saikan, and M. Grimsditch, Physical Review B **60**, 12730 (1999).

[34] W. Dreyer and H. Struchtrup, Continuum Mechanics and Thermodynamics **5**, 3 (1993).

[35] E. W. Prohofsky and J. A. Krumhansl, Physical Review **133**, A1403 (1964).

[36] B. Hehlen, A.-L. Pérou, E. Courtens, and R. Vacher, Physical Review Letters **75**, 2416 (1995).

[37] H. E. Jackson and C. T. Walker, Physical Review B **3**, 1428 (1971).

[38] V. Narayanamurti and R. C. Dynes, Physical Review B **12**, 1731 (1975).

[39] Neil. W. Ashcroft and N. D. Mermin, *Solid state physics* (Cengage Learning India Private Limited, New Delhi, 2010).

[40] A. Koreeda, R. Takano, and S. Saikan, Physical Review B **80**, 165104 (2009).

[41] M. Grimsditch, P. Loubeyre, and A. Polian, Physical Review B **33**, 7192 (1986).

[42] T. Kume, M. Daimon, S. Sasaki, and H. Shimizu, Physical Review B **57**, 13347 (1998).

[43] H. Shimizu, H. Tashiro, T. Kume, and S. Sasaki, Physical Review Letters **86**, 4568 (2001).

[44] H. Shimizu and S. Sasaki, Science **257**, 514 (1992).

## Chapter 2

# Experimental methods

In both Raman and Brillouin spectroscopy, the light scattered from the sample is collected and dispersed into its spectral components. These components are then detected by the appropriate detectors. Major difference between the Raman and Brillouin spectrometer comes from the frequency range probed by these two techniques as discussed in Chapter 1.

## 2.1. Brillouin spectrometer

Most Brillouin experiments probes the acoustic phonons in the frequency range of 0.1 - 1 $cm^{-1}$. A grating based spectrometer cannot be used to separate such low frequency shifts and weak components of the scattered light from the central Rayleigh peak which necessitates a high resolution, high contrast and a good throughput spectrometer. This is achieved using a Fabry-Pérot (FP) interferometer which is the major component of the Brillouin spectrometer [1-4]. The following sections briefly explain the details of the Brillouin spectrometer.

### 2.1.1. Fabry Perot interferometer

A FP consists of two plane mirrors which are parallel to each other with a spacing of $L_1$ between them which can be varied. For a spacing $L_1$, the interferometer will transmit only certain wavelength λ as determined by [5]

$$T = \frac{T_0}{1 + (4F^2/\pi^2) sin^2(2\pi L_1/\lambda)} \tag{2.1}$$

where, $T_0$ is the maximum possible transmission determined by the losses in the system and F is the finesse, defined as the ratio of the free spectral range (FSR) divided by the instrumental linewidth. FSR is the spacing between the successive transmitted wavelengths and can be varied by changing the mirror spacing (FSR, $\Delta\lambda = 1/2L_1$). Finesse depends on the reflectivity and flatness of the mirrors. For high quality mirror surfaces F ~ 100. The spectral contrast, $C$ is defined as the ratio of the maximum and minimum transmission and is given by [6].

$$C = 1 + (4F^2/\pi^2) \tag{2.2}$$

A single FP has a contrast of ~ $10^4$ which is not sufficient to measure the Brillouin signals, when signal is weak and strong elastically scattered light is present. This issue

can be resolved by passing the scattered light multiple times through the FP or through a series of FPs [6]. When light is passed 'n' times through the FP, contrast increases by $C^n$.

Even though the contrast improves on using the multi-pass technique, there is a problem of overlapping of the neighbouring interference orders. This can be compensated by extending the FSR using two interferometers of unequal mirror spacing which are combined to work in tandem mode. The wavelengths transmitted by them must simultaneously satisfy the conditions:

$$L_1 = {}^1/_2\, p\lambda_1 \text{ and } L_2 = {}^1/_2\, q\lambda_2 \tag{2.3}$$

where p, q are the integers and $\lambda_1$, $\lambda_2$ are the wavelength of light transmitted by the mirrors of spacing $L_1$, $L_2$ respectively. The light will be transmitted through the combined interferometer only if $\lambda_1 = \lambda_2$. The use of the tandem interferometer has been complicated due to the problem in achieving synchronisation of the scan. To scan the transmitted light, the mirror spacing $L_1$ and $L_2$ has to be incremented by $\Delta L_1$ and $\Delta L_2$ such that interferometers satisfy the conditions:

$$\frac{\Delta L1}{\Delta L2} = \frac{L1}{L2} \tag{2.4}$$

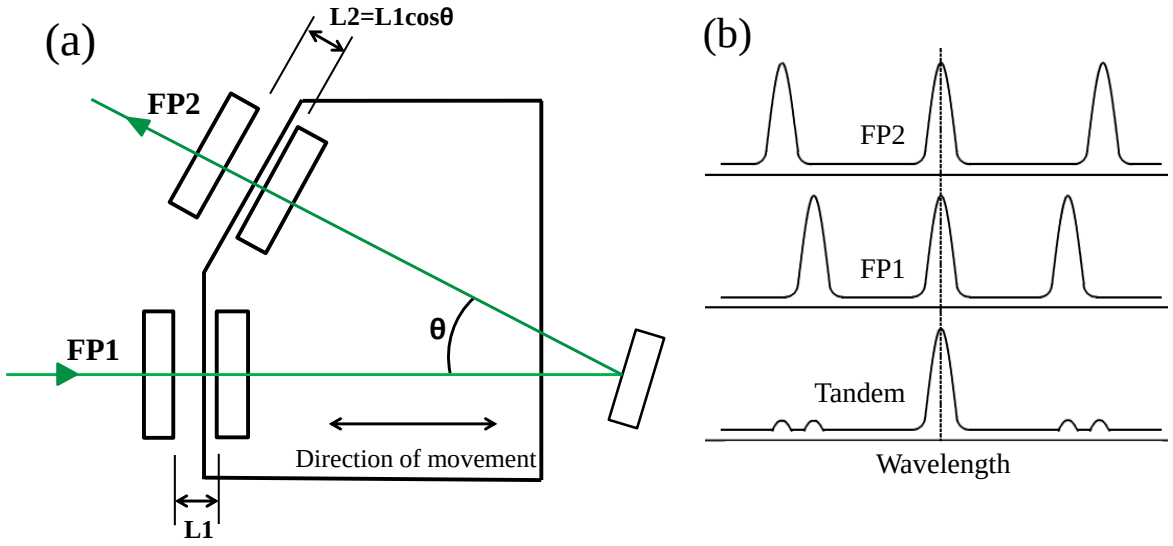


Fig. 2.1. (a) The schematic of the FPs in tandem operation in Sandercock-type Brillouin spectrometer. (b) Transmission from Fabry-Pérot interferometers during tandem operation.

In Sandercock-type interferometer, this condition is achieved by mounting the interferometers on the same scanning stage where FP2 is kept at an angle θ ~ 18º from FP1 as shown in Fig. 2.1(a) [7,8]. The spacing of the two interferometers satisfies the

condition $L_2 = L_1\cos\theta$ and the synchronisation condition (Eq. 2.4) is satisfied. The combined spectrum from this tandem operation is given in Fig. 2.1(b). The transmission peaks from neighbouring orders, overlaps only after several times the FSR of FP1 though small "ghosts" of the intervening transmission peaks remains. In this way, the FSR can be increased by a factor of 10-20 compared to that of single interferometer while the resolution remains the same.

### 2.1.2. Interferometer construction

The major drawbacks of a traditional FP which uses piezoelectric controlled scanning stacks for controlling and scanning the movement of mirrors are [5,6]:

1. Non linear scan (mirror displacement is not linearly proportional to the applied scan voltage).
2. Loss of parallel mirror alignment due to the tilting of the mirrors during the scan.
3. Changing mirror spacing is tedious as the mirror alignment will be lost on changing the mirror spacing.
4. Not stable (mean mirror spacing and parallel mirror alignment varies with time due to temperature fluctuations).

To circumvent the above problems, Sandercock-type Brillouin spectrometer uses scanning mirrors which sit on a translation stage comprising of a deformable parallelogram (for small displacement) attached to a crossed roller translation stage (for large displacement) [5,8]. The translation stage controls the mirror spacing by means of micrometer screw while the interferometer is scanned by piezoelectric transducer acting on the deformable parallelogram. The mirror spacing is sensed by a capacitive displacement transducer which controls the piezoelectric scanning transducer by means of a feedback loop.

The schematic of the arrangement of FPs in tandem operation is given in Fig. 2.1(a). The interferometers sit on a single scanning stage and the first interferometer FP1 is arranged in the direction of the translation stage movement with one mirror sitting on the translation stage and other on a separate angular orientation device. FP2 sits at an angle $\theta$ with the scanning direction with one mirror on the translation stage (similar to FP1) thus facilitating synchronous scanning by the two interferometers.

In order to scan the FP through a single transmission peak, a change in mirror spacing of ~ 25 Å is required which calls for a good vibration isolation. Any external influence which distorts the mirror spacing by a few Å should be avoided as they can degrade the spectrum. This can be provided using optical tables which are mounted rigidly on the floor and isolating the interferometer from the optical table by means of air columns. In addition, dynamic isolation mounts with feedback control are also used for the isolation of interferometer.

In order for a given spectral feature to occur always at the same point in a scan, a small correction has to be made to the scan voltage offset [6]. The mirror parallelism is maintained by making small alignment corrections so that a dominant spectral feature has either maximum amplitude or minimum linewidth, which is controlled automatically by a feedback loop. In most experiments, there is often too much elastic light entering the spectrometer so that the photon counting system gets saturated and no signal will be available for stabilising the interferometer. For this purpose, a reference beam is introduced into the spectrometer through the pinhole P1′ (Fig. 2.2) by means of opening the shutter SH2 and closing the shutter SH1 (which is in front of the entrance pinhole P1) while scanning the elastic peak.

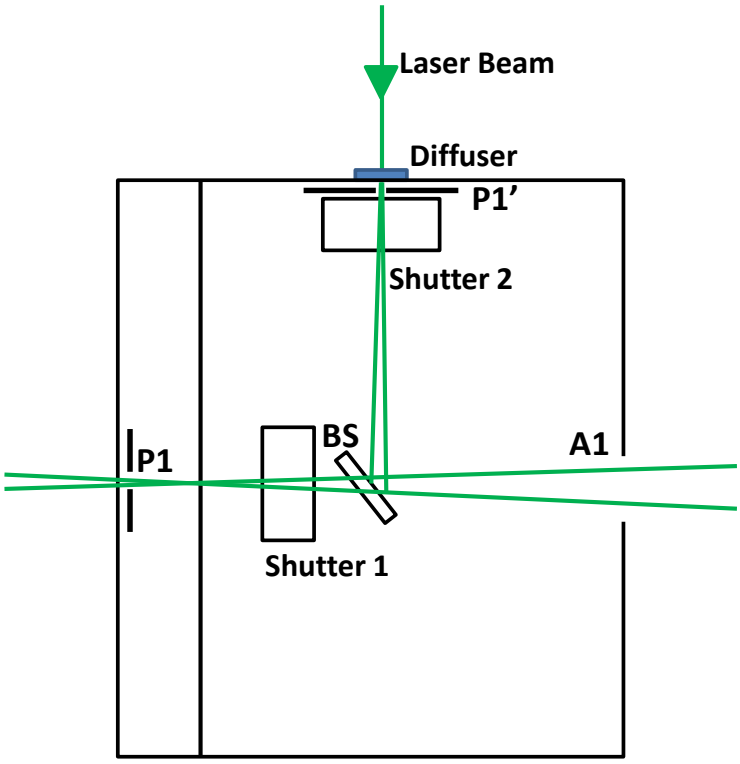


Fig. 2.2. The schematic of the pinhole and shutter assembly. P1-input pinhole, P1′-pinhole for the reference beam entrance, BS-beam splitter, A1-aperture.

### 2.1.3. Alignment of the interferometer

The alignment of the interferometer includes a) aligning the optics and b) pre-alignment of the interferometer before a Brillouin measurement.

Brillouin experiments are performed by operating the interferometer in multi-pass tandem mode [3,7]. The optical path during the tandem operation is shown in Fig. 2.3(a). The colored arrow heads indicate the different paths taken by light while passing through FPs and the holes in the apertures. The light entering through the input pinhole P1, passes through each FP three times before entering the exit pinholes, P2. The pinholes and apertures (Ap) helps to reduce the stray light. A series of mirrors, lenses and prisms are used to steer the light inside the interferometer. The pre-alignment is done in the 'alignment mode' whose optics arrangement is shown in Fig. 2.3(b). In the alignment mode, few optical components which are placed on a translational stage (inside the dashed rectangle in Fig. 2.3(a)) are inserted in the optical path inside the spectrometer by means of an external switch. The glass blocks G1, G2 and the beam splitters BS1, BS2 helps in directing the light onto the center of the FP1 and FP2 and in reflecting it to the output path so that it exit through the output pinhole (Fig. 2.3(b)). The optical components in both tandem and alignment mode has to be optimally aligned so as to obtain maximum output signal. The detailed steps for this alignment is given in Ref.[5]. This alignment is very crucial, especially for detecting weak Brillouin signals and has to be checked occasionally.

Before switching onto the tandem mode, both FPs has to be pre-aligned with correct relative mirror spacing. The reference beam is used for this. The pre-alignment method is based on the fact that when the FP is transmitting, the reflected intensity tends to zero with a minimum intensity obtained when the interferometer is optimally aligned. On scanning, the output signal will thus show a back ground intensity with a minima as shown for the case of a poorly aligned interferometer in Fig. 2.4(a). The alignment of the FP1 and FP2 can be then optimised to obtain a minimum which approaches zero (Fig. 2.4(b)) for both FP1 and FP2 by means of adjusting the X and Y tilts of the mirrors using the interferometer controller. The relative spacing $L_1$-$L_2$ can be adjusted to bring the pair of minima into coincidence and the pre-alignment of the interferometer is completed. The optical system can be then switched back to the 'tandem mode' and transmission will be observed with minor adjustment of X and Y and relative mirror spacing. The major

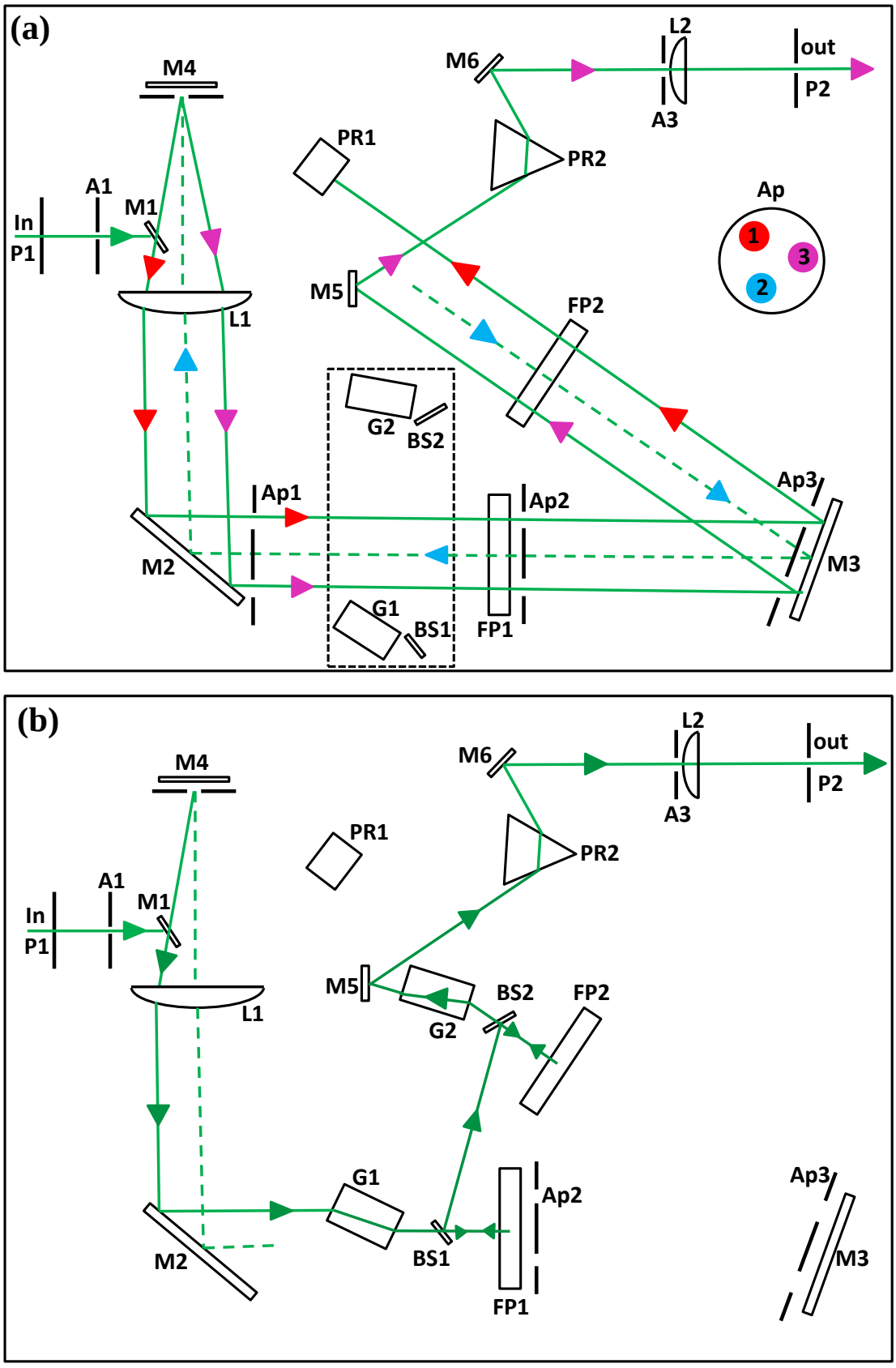


Fig. 2.3. The schematic of the optics in (a) tandem mode and (b) alignment mode. P-pinhole, M-mirrors, L-lenses, G-glass block, BS- beam splitter, PR-prisms, Ap-apertures, FP-Fabry Perot interferometer.

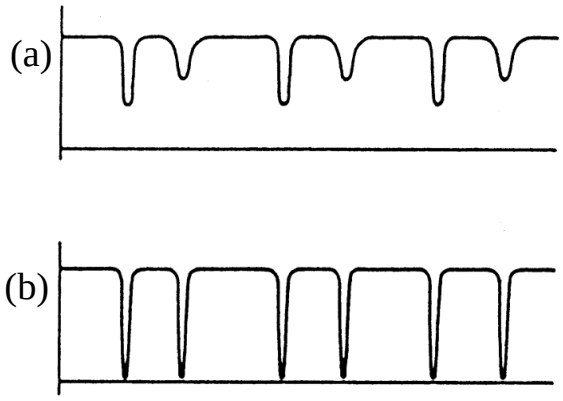


Fig. 2.4. The measured reflected intensity for two (a) imperfectly and (b) perfectly aligned interferometers.

advantage of the pre-alignment is that we can align the setup without opening the enclosure of the spectrometer.

### 2.1.4. Detection of the scattered light

To detect the weak Brillouin signal, a single photon counting detector is necessary. For this purpose, a very low background noise silicon photo avalanche diode (SPCM-AQR-16, Perkin Elmer, Canada) with quantum efficiency greater than 65% is used. The photodiode has to be thermoelectrically cooled and temperature controlled to ensure a stabilised performance regardless of the temperature fluctuations. As each photon is detected, a TTL pulse of 5 V is generated and is counted using a multichannel analyser (GHOST multichannel analyser MCA1, JRS Scientific Instruments, Switzerland) which is interfaced to a computer. The data acquisition is then done using GHOST 6.65 software. We have used 1024 channels for processing the data which gives the maximum resolution for a given mirror spacing.

### 2.1.5. Choice of the pinhole

The use of correct pinhole size is necessary to prevent the strong elastically scattered light from entering the spectrometer and preventing the stray light from being detected. Moreover, an input pinhole which is too large will lead to an asymmetry at the base of the elastic peak while a small pinhole leads to unnecessary loss of the signal. Both input and output pinhole sizes can be adjusted from outside and the output pinhole is usually 1.5 times that of the input pinhole to maximise the collection efficiency [5].

### 2.1.6. Scattering geometry

The schematic representation of the 180º scattering geometry used in the Brillouin scattering experiments in the thesis is shown in Fig. 2.5. The p-polarised 532 nm line of a single mode ($TEM_{00}$) solid-state diode pumped frequency doubled Nd:YAG laser (Model COMPASS 315M-150, Coherent Inc., USA) is used as the incident light source. It is focussed onto the sample by means of a suitable lens (L1). The laser power can be controlled using neutral density filters (NDF) which can be moved in and out of the beam path according to the intensity requirements. A long working distance (WD) objective lens (NIKON L Plan 20X, numerical aperture, NA = 0.33 and WD 24 mm) is used here for focussing the incident light onto the sample as well as for collecting the scattered light.

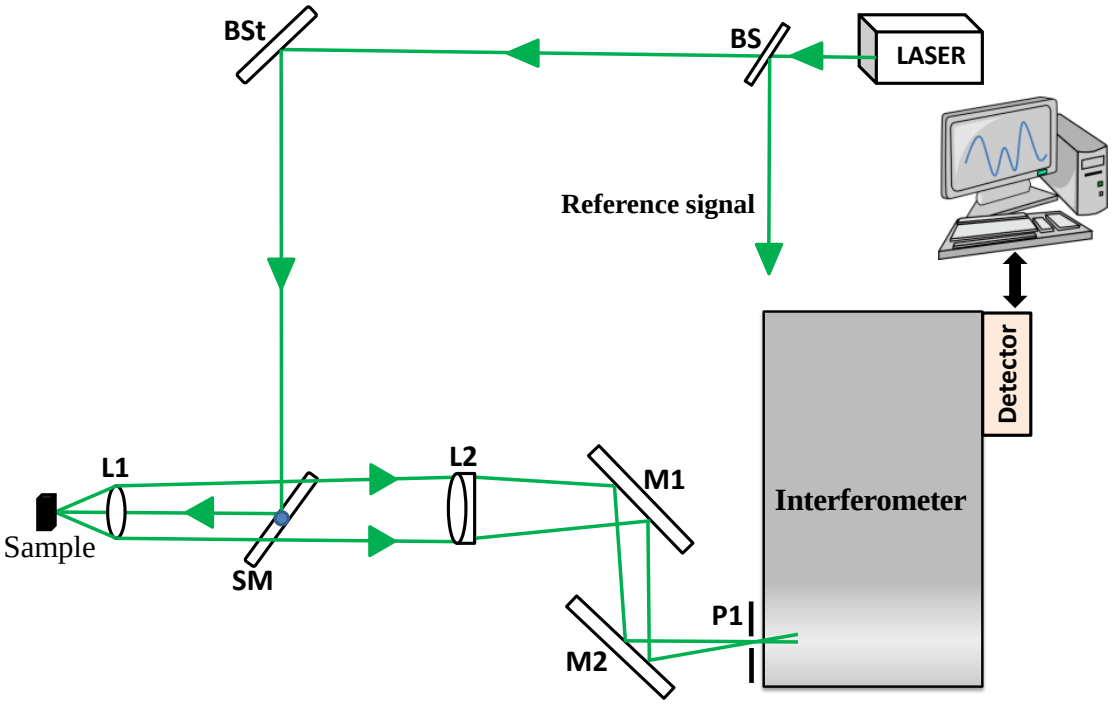


Fig. 2.5. The schematic of the Brillouin setup. BS-beam splitter, BSt-beam steerer, SM-special mirror, L-lens, M-mirror.

A special mirror (SM) with a silver spot of diameter ~ 3 mm on a 25 X 35 mm fused silica substrate of thickness of 1 mm is used for directing the light from the source to the sample. This ensures the collection of maximum scattered light especially when objectives having small back apertures are used. The scattered light is then focused onto the input pinhole of the interferometer using an achromatic doublet lens (L2). The focal

length of the doublet depends on the diameter of the back aperture of the objective and is selected to ensure that maximum light enters through the pinhole (~ 150 mm for the 20X objective lens used). The mirrors M2 and M3 are utmost necessary as it helps to steer the focussed beam normal to the entrance pinhole.

## 2.2. Raman spectrometer

We have used a custom build micro-Raman spectrometer which is based on a single monochromator and a CCD detector coupled to a part of a Nikon microscope using a fiber optic cable. The basic difference between the Brillouin and Raman spectrometer lies in the use of grating for dispersing the spectral components of the scattered light instead of FP.

The schematic of the Raman spectrometer used is shown in Fig. 2.6. A linearly polarised 532 nm line of a frequency doubled Nd-YAG solid state diode pumped continuous wave laser (Model GDLM-5015L, Photop Suwetech Inc., China) with an output power of ~ 30 mW is used as the excitation source. The plasma lines of the laser can be removed using a plasma line filter (PF) (LL01-633-12.5, Semrock). NDFs are used to control the intensity of the laser at the sample. A dichroic mirror (DM) at an angle of 45$^{o}$ reflects the laser onto the sample where it is focussed using an infinity corrected objective lens (OL) (NIKON, L Plan 50X, 0.45 NA, WD 17 mm). The Rayleigh elastically scattered light and the inelastically scattered Raman signals from the sample are collected by the objective lens and directed onto an edge filter (EF) (LP03-532RS-25, Semrock) which rejects majority of the Rayleigh light. The light is then focussed onto an optical fiber using an objective lens (NIKON L Plan 20X, 0.33 NA, WD 24 mm). The other end of the optical fiber is f-number matched to the monochromator (MONO) of focal length 550 mm (Jobin-Yovn, Triax 550, Instruments SA, Inc., NJ, USA) attached with a liquid nitrogen cooled CCD detector (spectrum one). The light enters the monochromator through a slit of width 200 μm and was dispersed using a holographic grating of 1800 grooves/mm onto the CCD. The CCD consists of a rectangular two dimensional array of pixels (1024 x 128). Labspec software is used for controlling the data acquisition, slit width, spectral range *etc.* The area under the objective lens can be used for keeping the micrometer stage (MS) which is used for placing the samples. The cryostage and diamond anvil cells (DAC) used for performing the Raman measurements at different thermodynamic conditions can also be placed on the microstage.

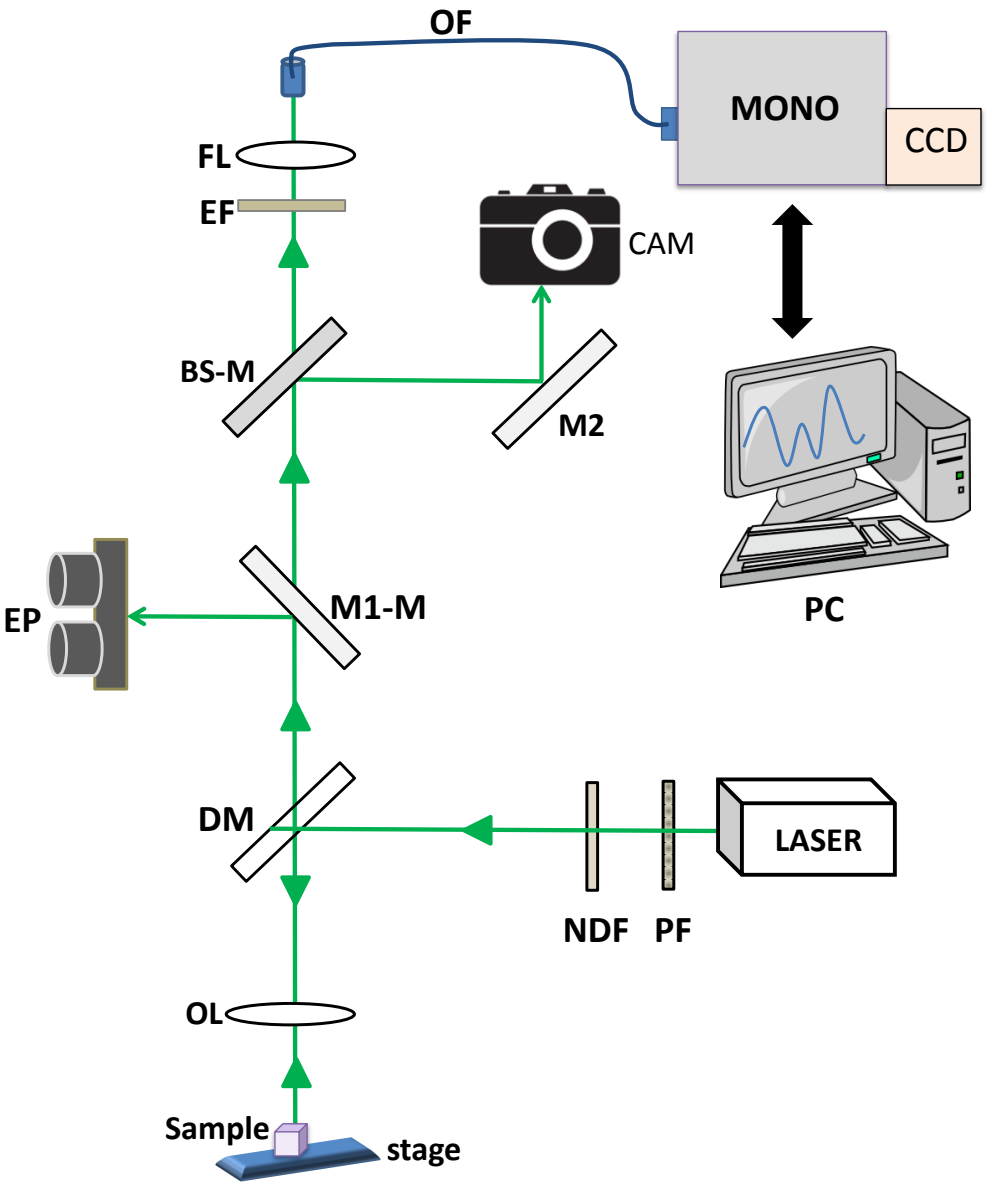


Fig. 2.6. Schematic of the Raman spectrometer. PF-plasma line filter, NDF-neutral density filter, DM-dichroic mirror, OL-objective lens, M1-M- movable mirror, BS-M-movable beam splitter, EP-eye piece, M2-mirror, EF-edge filter, FL-focussing lens, OF-optical fiber, CAM-camera, MONO-monochromator.

## 2.3. High pressure techniques

Pressure is a fundamental thermodynamic parameter for tuning the properties of materials. The pressure, P is generated by applying an external force, F on the area, A according to the formula

$$P = \frac{F}{A} \tag{2.5}$$

An opposed anvil device can be employed for exerting a large force on a small area which generates pressures upto megabar regime. Reducing the effective area of the flat faces of anvils is a smarter way to achieve higher pressures compared to increasing the force on them. Increasing the applied force may result in the failure of the anvils if it exceeds the compressive strengths of the anvils to withstand the stress. This forms the basis of the pressure generation technique [9,10]. The subsequent sections discusses the pressure generation using diamond anvil cell (DAC), diamond alignment, gaskets, pressure transmitting mediums *etc.* which are very crucial for the technique of high pressure.

### 2.3.1. Diamond anvil cell

Diamond anvil cell is the most widely known high pressure research equipment among all the anvil materials used so far. Diamond is used for the high pressure studies of materials as it is the hardest and the least compressible material. Moreover it is transparent to the most of the spectrum of electromagnetic radiation, including γ-ray, X-ray, visible light and most of the infrared and ultraviolet region. The DAC have been used for the in-situ pressure studies in Mossbauer spectroscopy, X-ray, Raman spectroscopy, Brillouin spectroscopy *etc* [11-14]. The schematic diagram of a DAC is given in Fig. 2.7. In a DAC, sample is placed between the polished culets of two diamonds which are placed opposite to each other. The sample chamber is formed by a metal gasket which also encloses a pressure transmitting medium and pressure calibrant. Based on the differences in the mechanisms for generating the force and alignment of the anvils, there are different DAC designs. The five major types of DACs are [15-19]: Mao-Bell cell, Bassett cell, NBS cell, Merrill-Bassett cell and Syassen-Holzapfel/Membrane cell. We have used the membrane diamond anvil cell (MDAC) from IMPMC, University of Pierre and Marie Curie, France for the high pressure studies in this thesis. This MDAC has a wide angle aperture of ~ 85º / 85º which is ideal for the Brillouin experiments.

The schematic diagram of the MDAC is shown in the Fig. 2.8. The major components of the MDAC are:

1. Stainless steel gas membrane or diaphragm which pushes the piston against the cylinder when gas is filled in it.
2. Diamonds which are glued to the upper and lower rockers or backing plates.
3. Guidance dowel/guide screws to hold and align the piston inside the cylinder.

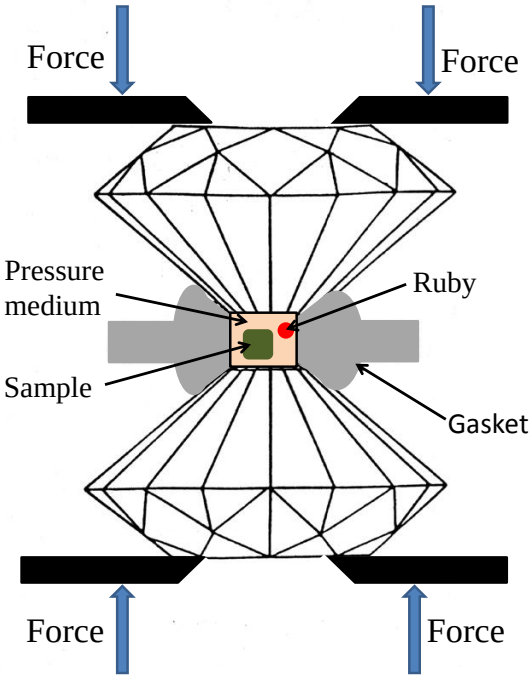


Fig. 2.7. Schematic of a diamond anvil cell.

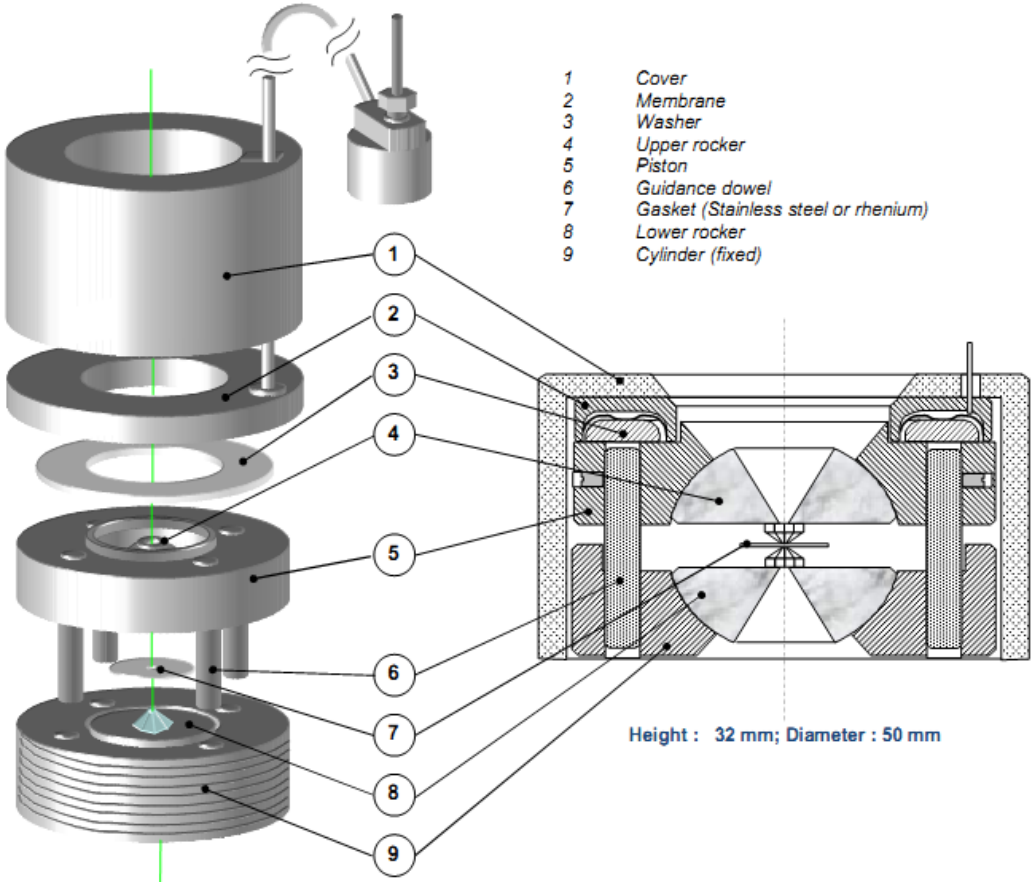


Fig. 2.8. The Schematic diagram of the membrane diamond anvil cell. (Adopted from the website *www.betsa.fr*)

In our MDAC, guidance dowel is replaced with a guide screw and notch which aligns and lock the piston over the cylinder in only one way. A pneumatic drive system (PDS) which consist of a helium gas cylinder of 200 bar capacity is connected to the MDAC to control the pressure. The MDAC and the PDS used in the thesis is shown in Fig. 2.9(a, b). For generating pressure inside the cell, the gas membrane is filled with the helium gas which bulges it and pushes the piston against the cylinder.

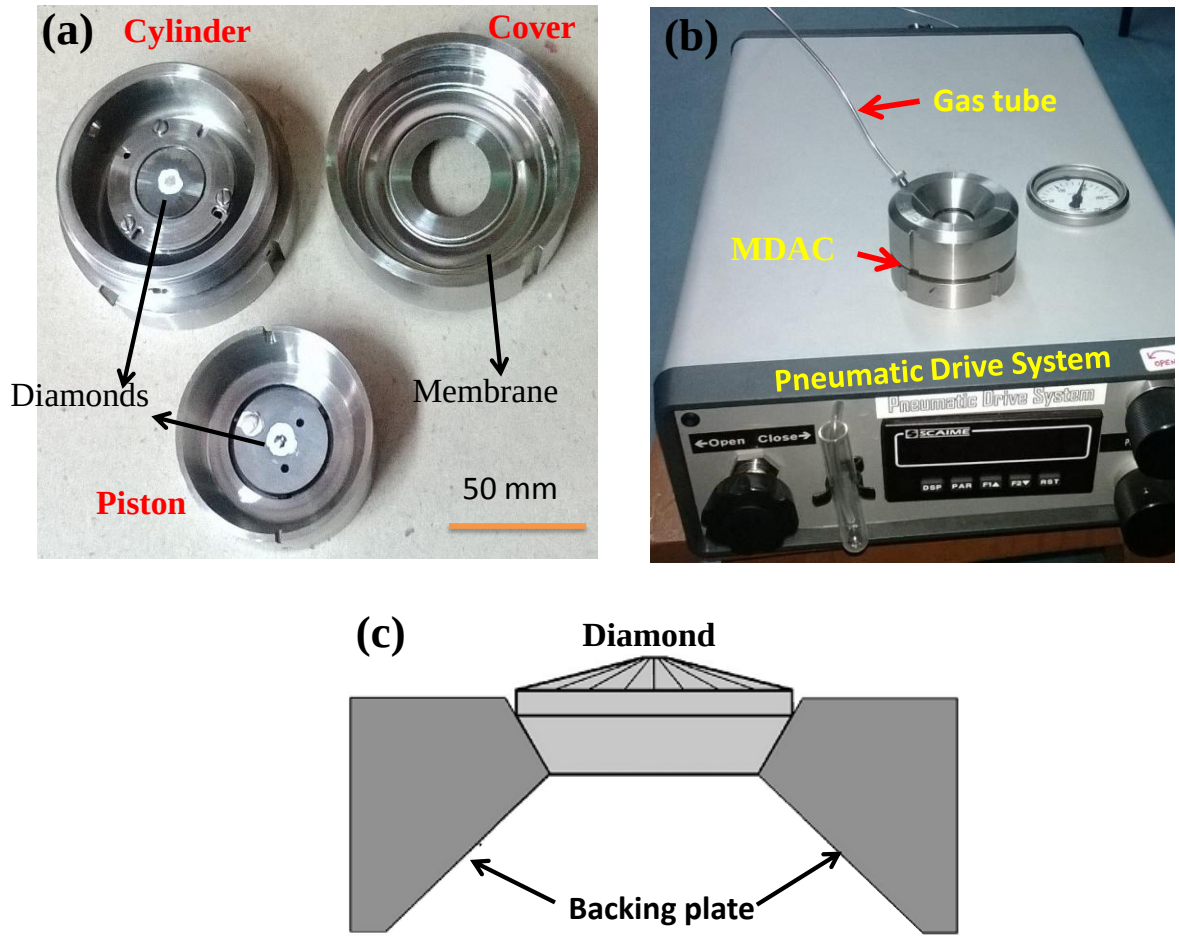


Fig. 2.9. Photograph of (a) MDAC and (b) MDAC connected to the pneumatic drive system (PDS). (c) Schematic of the Boehler-Almax design diamond (picture adopted from Ref. [20]).

### 2.3.2. Diamond

Diamonds has to be chosen carefully for the DAC with special consideration of the cut, color, clarity and carat. Generally, gem quality and brilliant cut diamonds are used in most DACs. In MDAC we use Boehler-Almax diamond anvils which are designed for giving optimised mechanical support for the anvils crown section, by a perfect match

between the anvil and the rocker [20,21]. The schematic of the Boehler-Almax diamond design is given in the Fig. 2.9(c). The diamonds are classified as type Ia, type Ib, type IIa and type IIb depending on the presence and nature of the impurities. Type IIa diamonds are the purest and Type I contains nitrogen impurities. Type Ia diamonds which contains nitrogen atoms clustered within the carbon lattice are commonly used due to their easy availability and low cost, though they have very strong adsorption in the mid infrared region. The size of the diamonds in the DAC ranges from 1/8 to 1/2 carat. The culet size of the diamond determines the maximum pressure achieved using it. The maximum attainable pressure ($P_{max}$) using a diamond anvil of culet diameter $d$ is given by [22]

$$P_{max} = \frac{12.5}{(d(mm))^2} \tag{2.6}$$

The table diameter of the diamonds determines the stress applied to the backing plates which in turn determine the maximum attainable pressure. The culet size should be much smaller than the table size of the diamonds to intensify the low pressure applied to the table for generating high pressure at the culet. The ratio of the table area to the culet area gives the pressure intensification.

### 2.3.3. Backing plates

They support the diamonds and are very important factor which limits the maximum pressure that can be exerted. If the stress in the backing plate exceeds that needed for the plastic deformation, the alignment of the diamonds can be upset which will ultimately results in the breakage of the diamonds. Backing plates are usually made from tungsten carbide or boron carbide. They are provided with tapered holes where the diamonds are placed and the culet can be centered. The holes of the backing plates provide access to the laser light and other radiations.

### 2.3.4. Diamond alignment

The critical and important part of the DAC measurement is aligning the diamonds. The culet surfaces should be aligned laterally and parallel to each other to prevent severe gasket deformation and diamond breakage. The MDAC can be aligned using the following steps. First the diamonds needs to be laterally aligned. This is achieved by carefully inserting the piston into the cylinder, and seeing through a microscope the culets of the diamonds are matched along the X and Y directions by adjusting the set screws

located on the piston wall. Then the culets can be aligned parallel to each other by observing the Newton's rings and adjusting the screws on top of the cylinder. The interference fringe pattern is observed when the diamonds are not perfectly parallel and perfect alignment will be achieved when zero-fringe condition (when a single dark or bright fringe covering the entire culet) is formed. The alignment of the diamonds needs to be checked after each pressure cycle.

### 2.3.5. Gasket

The introduction of the gasket between the diamonds creates a sample chamber where the pressure transmitting medium and the sample can be contained for the high pressure experiments. The gasket also helps in supporting the diamond culet as it extrudes around the diamond and forms a ring on compression, thereby protecting the diamond edges from breaking. Materials like hardened stainless steel (T301), inconel, tungsten, rhenium and copper-beryllium alloys are usually used as gasket materials. The gasket is pre-indented before being used for high pressure studies. Pre-indentation of the gasket work hardens it and reduces the deformation of the hole, thus preventing the damage of the diamonds. The hole (size of ~ 1/3 culet size [23]) which confines the sample and medium has to be drilled at the center of the pre-indented area. The stability of the gasket is indicated by an equal and opposite force acting between the gasket material and the surface of the culet. If the thickness of the gasket is small, the destabilising inward force will be larger than the outward stabilizing force and results in the shrinkage of the holes. If the thickness of the gasket is large, the outward destabilizing force will be larger than the inward stabilizing force, and results in the elongation of the gasket hole. Hence it is very important to watch the shape of the gasket hole during the experiment each time when the pressure is changed and the experiment has to be terminated if there is any asymmetric elongation or extreme shrinkage.

We have used stainless steel gasket (T301) of dimension 5 X 5 mm with an initial thickness 180 μm. This was pre-indented to a thickness of ~ 60 μm and ~ 100 μm for the high pressure experiments in Chapter 7 and Chapter 4, respectively. A hole of 140 μm was drilled in the gasket with a micro drill equipment using micro solid carbide drill bit. After pre-indenting, the gasket was fixed on the rocker using glue. Special care has to be taken so that the glue does not enter the hole during the experiment.

## 2.3.6. Pressure medium

To achieve the hydrostatic pressure conditions on the sample inside the DAC, sample has to be immersed in a medium. Various fluids, solids and gases can be used as the pressure transmitting medium (PTM) with an important criterion that these do not react with the sample [24-27]. The hydrostatic limits of few liquid mediums are : silicone oil ~ 2 GPa, isopropyl alcohol ~ 4 GPa, $H_2O$ ~ 5 GPa, pentane - iso pentane (1:1) ~ 7 GPa, methanol ~ 8 GPa, methanol - ethanol (4:1) ~ 10 GPa, methanol - ethanol - water (16:3:1) ~ 14.5 GPa. These liquids solidify above the pressure mentioned, becoming quasi-hydrostatic. Hence weak changes in the sample properties above the hydrostatic pressure limit have to be carefully verified before concluding any useful information. Solid mediums like NaCl ~ 7 GPa and AgI ~ 7 GPa can also be used. For hydrostatic conditions at very high pressures, gases like hydrogen ~ 177 GPa, He ~ 70 GPa, Ne ~ 16 GPa *etc*. can be used. We have used methanol - ethanol (4:1), propanol mediums in Chapter 4 and methanol - ethanol - water (16:3:1), water mediums in Chapter 7.

## 2.3.7. Pressure measurement

Ruby fluorescence method is used for the in-situ pressure calibration in high pressure experiments. Ruby chips are loaded along with the samples to measure the in-situ pressure. Fluorescence from ruby crystal (5% $Cr^{3+}$-doped $Al_2O_3$) exhibits pressure dependence [28]. The ruby emission spectra consists of two peaks - R1 and R2 which originates from the crystal field splitting of d-orbitals of $Cr^{3+}$ ion which is surrounded by oxygen atoms in octahedral geometry. The R1 and R2 lines occurs at 694.2 nm and 692.7 nm respectively, and R1 line is mainly used for the pressure calibration under static pressure [29]. Under hydrostatic conditions, the two R-lines equally shift and the difference between their peak positions (R1 - R2) remains constant. The pressure can be calculated from the formula [30]

$$P(GPa) = \frac{1904}{B}\left[\left(1 + \frac{\Delta\lambda}{\lambda_0}\right)^B - 1\right] \tag{2.7}$$

Where, $\Delta\lambda = \lambda_P - \lambda_0$. $\lambda_P$ and $\lambda_0$ are the wavelength at pressure P and ambient pressure respectively. The value of B = 7.655 for hydrostatic conditions and 5 for quasi hydrostatic conditions. Under non hydrostatic condition, R1 - R2 no longer remains constant and the peaks broaden.

### 2.3.8. Pressure dependent Brillouin studies

The Pressure dependent Brillouin setup was developed for these experiments by the author. The schematic of the high pressure Brillouin setup is given in Fig. 2.10. The image of the sample can be obtained on a screen placed in front of the entrance pinhole by illuminating the DAC from backside as shown. This can be used for focussing the laser on the sample or ruby. The Ruby fluorescence was measured using a miniature spectrometer (model USB4000-SPL, Ocean optics) where the light is focussed onto an optical fiber using a lens assembly.

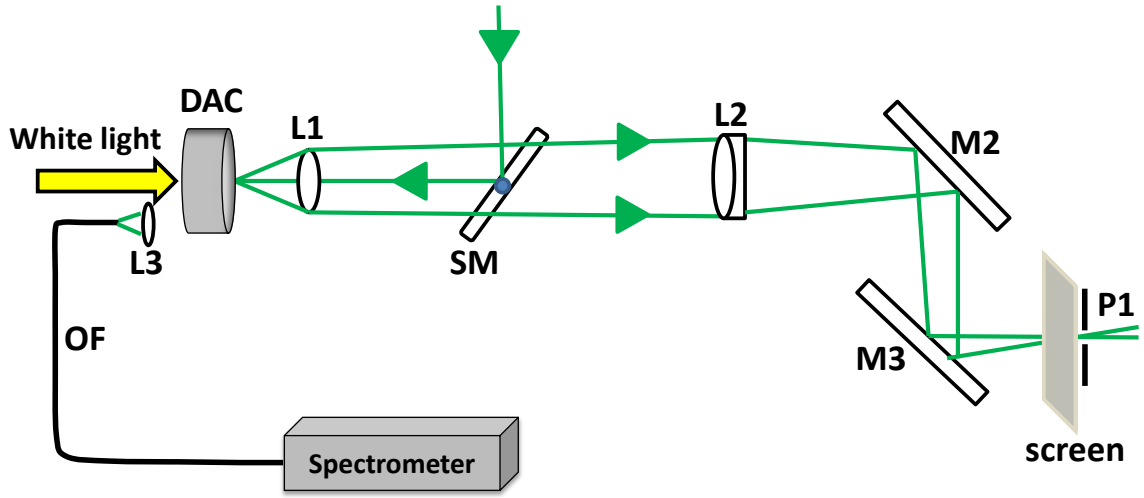


Fig. 2.10. Schematic of the high pressure Brillouin setup.

## 2.4.Temperature dependent studies

We have used the cryostage (Linkam THMS 600, Linkam scientific, UK) equipped with a liquid nitrogen pumping module (LNP 94) for the temperature dependent studies. The temperature was controlled with an accuracy of ± 0.1 K. An external control unit (Linkham TMS 94) was used for setting the temperature and performing the ramping at user specified rates. A ramp rate of 10 ºC/min was used for the experiments in the thesis. The Linkam stage has ports for the gas entry and exit and this is used for performing the gas adsorption Brillouin studies in Chapter 3.

## 2.5. Bibliography

[1] T. Blachowicz, R. Bukowski, and Z. Kleszczewski, Review of Scientific Instruments **67**, 4057 (1996).

[2] J. G. Dil, N. C. J. A. van Hijningen, F. van Dorst, and R. M. Aarts, Applied Optics **20**, 1374 (1981).

[3] R. Mock, B. Hillebrands, and R. Sandercock, Journal of Physics E: Scientific Instruments **20**, 656 (1987).

[4] K. Weishaupt, S. H. Anders, R. G. Eberle, and M. Pietralla, Review of Scientific Instruments **68**, 3996 (1997).

[5] C. V. Raman, Indian J. Phys. **2**, 387 (1928).

[6] J. R. Sandercock, *Light Scattering in Solids III, Topics in Applied Physics* (Springer, Germany, 1982), Vol. 51.

[7] S. M. Lindsay, M. W. Anderson, and J. R. Sandercock, Review of Scientific Instruments **52**, 1478 (1981).

[8] S. M. Lindsay and I. W. Shepherd, Review of Scientific Instruments **48**, 1228 (1977).

[9] W. A. Bassett, High Pressure Research **29**, 163 (2009).

[10] J. C. Jamieson, A. W. Lawson, and N. D. Nachtrieb, Review of Scientific Instruments **30**, 1016 (1959).

[11] A. Jayaraman, Reviews of Modern Physics **55**, 65 (1983).

[12] A. Jayaraman and S. K. Sharma, Current Science **74** (1998).

[13] A. Polian, Journal of Raman Spectroscopy **34**, 633 (2003).

[14] Sergio Speziale, Hauke Marquardt, and T. S. Duffy, Reviews in Mineralogy & Geochemistry **78**, 543 (2014).

[15] W. A. Bassett, T. Takahashi, and P. W. Stook, Review of Scientific Instruments **38**, 37 (1967).

[16] H. K. Mao and P. M. Bell, Carnegie Inst. Washington Yearbook **77**, 904 (1975).

[17] G. Huber, K. Syassen, and W. B. Holzapfel, Physical Review B **15**, 5123 (1977).

[18] L. Merrill and W. A. Bassett, Review of Scientific Instruments **45**, 290 (1974).

[19] G. J. Piermarini and S. Block, Review of Scientific Instruments **46**, 973 (1975).

[20] R. Boehler, Review of Scientific Instruments **77**, 115103 (2006).

[21] R. Boehler and K. De Hantsetters, High Pressure Research **24**, 391 (2004).

[22] D. J. Dunstan and I. L. Spain, Journal of Physics E: Scientific Instruments **22**, 913 (1989).

[23] D. J. Dunstan, Review of Scientific Instruments **60**, 3789 (1989).

[24] G. J. Piermarini, S. Block, and J. D. Barnett, Journal of Applied Physics **44**, 5377 (1973).

[25] Y. Shen, R. S. Kumar, M. Pravica, and M. F. Nicol, Review of Scientific Instruments **75**, 4450 (2004).

[26] Y. Shu-Jie, C. Liang-Chen, and J. Chang-Qing, Chinese Physics Letters **26**, 096202 (2009).

[27] N. Tateiwa and Y. Haga, Review of Scientific Instruments **80**, 123901 (2009).

[28] R. A. Forman, G. J. Piermarini, J. D. Barnett, and S. Block, Science **176**, 284 (1972).

[29] K. Syassen, High Pressure Research **28**, 75 (2008).

[30] H. K. Mao, P. M. Bell, J. W. Shaner, and D. J. Steinberg, Journal of Applied Physics **49**, 3276 (1978).

# Chapter 3

# Effect of pore occupancy on the acoustic properties of Zeolitic Imidazolate Framework (ZIF)-8 at ambient and low temperatures

Dhanya Radhakrishnan and Chandrabhas Narayana "*Effect of pore occupancy on the acoustic properties of ZIF-8: A Brillouin spectroscopic study at ambient and low temperatures"* J. Chem. Phy., **143**, 234703 (2015)

## 3.1. Introduction

Metal organic frameworks (MOFs) are microporous materials consisting of metal ions and organic linkers which have a huge variety of applications ranging from gas storage to drug delivery [1,2]. Though knowledge of elastic properties of MOFs are very important due to their technological applications, they are rarely studied [3]. MOFs exhibit huge responses to external stimuli like temperature, pressure, guest incorporation *etc.* due to the presence of weak chemical bonding and flexible organic ligands [4]. Yet, thorough experimental and computational studies on the elastic properties of MOFs at extreme conditions (temperature/pressure) with or without the presence of guest remains unexplored. There have been recent temperature dependent elastic property studies on MOFs, namely, molecular dynamic calculations on MOFs in the absence of any guest [3,5], Brillouin scattering studies across ferroelectric phase transition in $[NH_4][Mn(HCOO)_3]$ and $[NH_4][Zn(HCOO)_3]$ as the system goes from $P6_322$ to the $P6_3$ phase [6]. Nanoindentation has been used at the ambient temperature to study the influence of guest incorporation on the mechanical properties of some ZIFs, MOF-74-Zn and a few soft porous crystals, but the temperature dependence of elastic properties on guest incorporation have not been attempted [7-10].

Zeolitic imidazolate frameworks (ZIFs) are a class of MOFs where the metal atoms ($M^{n+}$=$Zn^{2+}$, $Co^{2+}$) are tetrahedrally coordinated to the N atoms of imidazolate derived linkers (IM=$C_3N_2H_3^-$) subtending an angle of 145° at the M-IM-M centre, analogous to the Si-O-Si angle in zeolites to form porous architectures (Fig. 3.1(a, b)) [11]. They possess exceptional thermal and chemical stability and exhibits diverse topologies. ZIF-8 ($Zn(mIM)_2$, mIM = 2-methyl imidazolate) a prototypical ZIF with sodalite (SOD) topology, crystallizes in cubic space group $I\bar{4}3m$ and exhibits a large solvent accessible volume (SAV) of 50%, making it an ideal candidate for studying the effect of pore occupancy on the mechanical properties and thus the guest-host interaction. ZIF-8 contains pores of 11.6 Å diameter connected by eight windows of 3.4 Å (Fig. 3.1(c)) and its structure is flexible as evidenced by the adsorption of gases of kinetic diameter higher than its window dimensions (for example $N_2$ and $CH_4$ of kinetic diameter greater than 3.6 Å) [12-14]. At relatively high pressures (1.46 GPa) imidazolate linker rotates which increases the pore volume as well as window dimensions thus introducing more guest molecules inside the pores (Fig. 3.1(d)) [15]. This phase at high pressure has been called

ZIF-8HP while the one at ambient pressure is ZIF-8AP [13]. The enhanced gas uptake at low temperature is also explained by this gate opening. XRD, IR, Raman, NMR *etc.* have been employed to study the flexibility of ZIF-8 in the presence of guests with temperature or pressure [15-20].

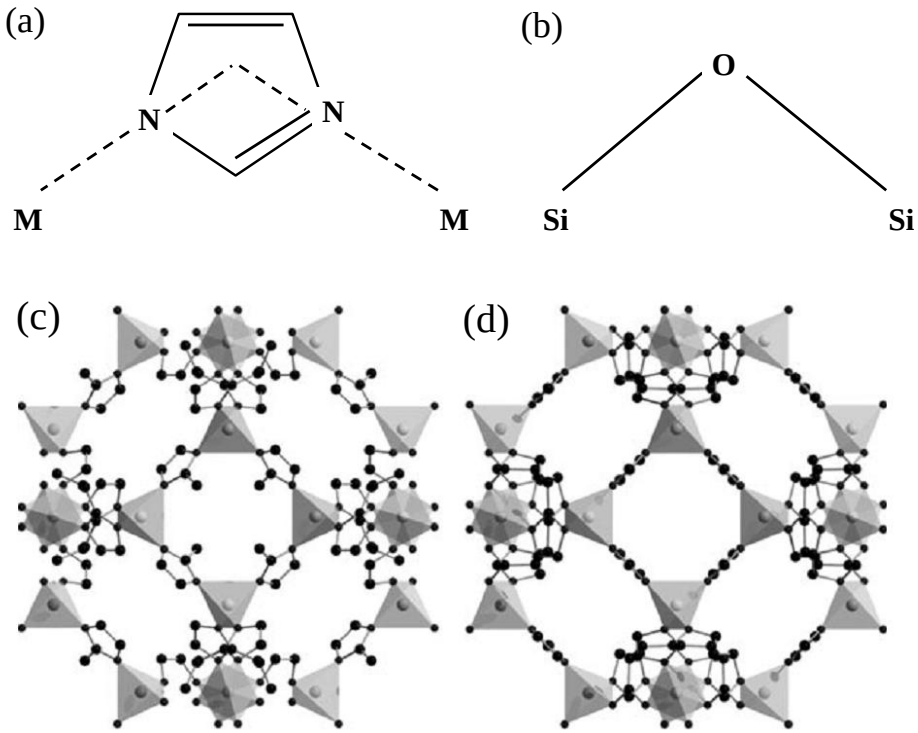


Fig. 3.1 Bridging between (a) imidazolate and the metal centers (M) in ZIFs, M-IM-M which is analogous to (b) Si-O-Si bridging in aluminosilicate zeolites. The structure of ZIF-8 at (a) ambient pressure and at (b) 1.47 GPa depicting the change in the orientation of the imidazolate group. The polyhedra represent $ZnN_4$ tetrahedra (c and d are adopted from Ref. [14]).

Brillouin spectroscopy has been used earlier to study the ambient temperature elastic properties of evacuated ZIF-8 which revealed its exceptionally low shear modulus [21]. Compared to ultrasonic and nanoindentation techniques, Brillouin spectroscopy is much more versatile, easy and adaptable for many samples, making it an ideal tool to determine the acoustic velocity in MOFs. Moreover temperature dependent adsorption studies can be carried out easily using Brillouin spectroscopy unlike nanoindentation [22]. We have used Brillouin spectroscopy to study the effect of pore occupancy on the spectral features (the peak position, width of the acoustic modes and the central peak) of ZIF-8 by introducing various guests at room temperature. This is followed by the temperature dependence of acoustic modes upon gas adsorption.

## 3.2. Experimental details

Brillouin spectra were recorded in backscattering geometry, using a 532 nm laser excitation with a power of 2 mW focused using a 20X objective lens. The scattered light was analyzed using a six pass tandem Fabry-Perot interferometer (JRS scientific instruments). Transmitted light was detected using a silicon photo avalanche diode (SPCM-AQR-16, Perkin Elmer, Canada) and processed by a multi-channel analyser with 1024 channels. A free spectral range of 43 GHz was used with a typical accumulation time of 5-10 min.

ZIF-8 was synthesised according to Ref. [10]. All the reagents and solvents were used as supplied without further purification. 0.210 g of $Zn(NO_3)_2.6H_2O$ and 0.06 g of 2-methyl imidazole (both obtained from Sigma-Aldrich) was mixed in 18 ml of N,N-dimethylformamide (DMF) and stirred for 20 min after which the mixture was heated at 140 $^oC$ for 24 hrs. On cooling the mixture, the mother liquid was removed and colourless polyhedral crystals were isolated. The crystals were then washed with DMF several times and immersed in methanol for solvent exchange, followed by heating at 150 ºC for 6 hours. ZIF-8 was characterised by powder x-ray diffraction (PXRD) recorded on a Bruker Discover instrument using Cu-Kα radiation. Figure 3.2 shows the XRD pattern of the as-synthesised and evacuated ZIF-8. The XRD data shows that the structure of the ZIF-8 did not change on evacuation. The elastic property of ZIF-8 with respect to pore occupancy is studied by introducing various guests. Alcohols (methanol, ethanol, 1-propanol and 1-butanol) and DMF were introduced by soaking ZIF-8 in respective solvents for 48 hrs after which they were taken in capillary tubes.

The temperature dependent gas adsorption measurements were done using a Linkam stage (THMS 600) with a temperature stability of 0.1 K. ZIF-8 crystals were enclosed between two coverslips with only the corners being sealed, letting sufficient gap for the gas to enter. Coverslips were used just to hold the sample, because cryogenic stage has to be placed vertically in our Brillouin setup. Heat transmitting grease was used to fix the coverslip on the stage. Prior to the experiment, sample was first heated to 120 ºC for 1 hr to remove any trapped solvent molecules and then cooled to room temperature. At this stage, gases ($N_2$, $CO_2$ and Ar) were introduced for 15 min, after which the sample was cooled at a rate of 10 ºC/min, keeping the gas pressure at a constant value of ~ 1 atm. The temperature dependent Raman measurements were also performed under similar

experimental conditions using 532 nm laser excitation (Chapter 2) to study the changes in the local structure.

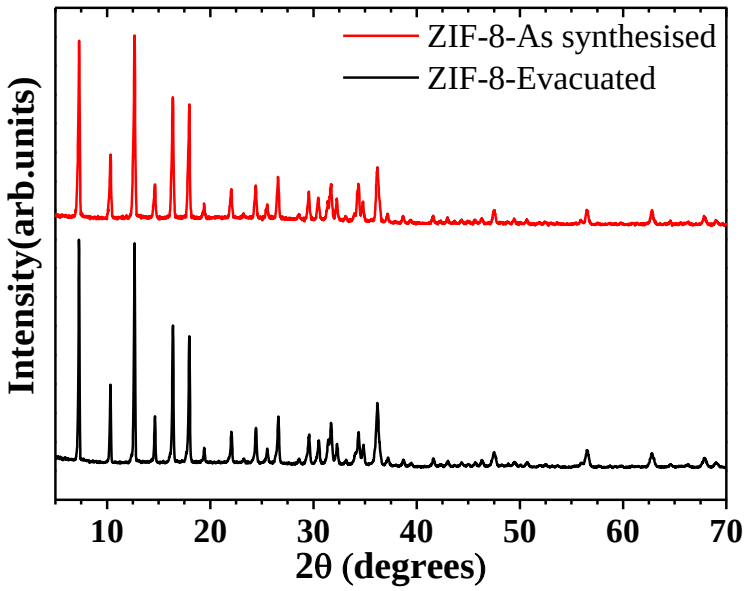


Fig. 3.2. The powder XRD pattern of as-synthesised and evacuated ZIF-8.

## 3.3. Results and discussion

A typical Brillouin spectrum of evacuated ZIF-8 is shown in Fig. 3.3. Two acoustic modes are observed, namely a longitudinal acoustic mode (LA) at ~ 16 GHz and a transverse acoustic mode (TA) at ~ 5 GHz. From the Brillouin study at ambient conditions by Tan *et al.* we can say that the TA mode observed is the slow TA mode (TA1) which is related to the minimum value of shear modulus [21]. In addition to the acoustic modes, a quasielastic central peak (CP) centered at zero frequency is also observed.

Brillouin spectra were obtained for samples of unknown crystallographic orientation and the acoustic velocity $V$, can be determined from the Brillouin shift $v$, using the relation $v = 2\frac{2\pi}{\lambda} n\, V \sin\theta/2$ where $n, \lambda\ and\ \theta$ are refractive index, excitation wavelength and the scattering angle, respectively. The elastic properties can be derived from the direction dependence of the acoustic velocities which is obtained by rotating the sample along the azimuthal direction, $\phi$ considering a random direction (x) as $\phi = 0$ (Fig. 3.4(a)).

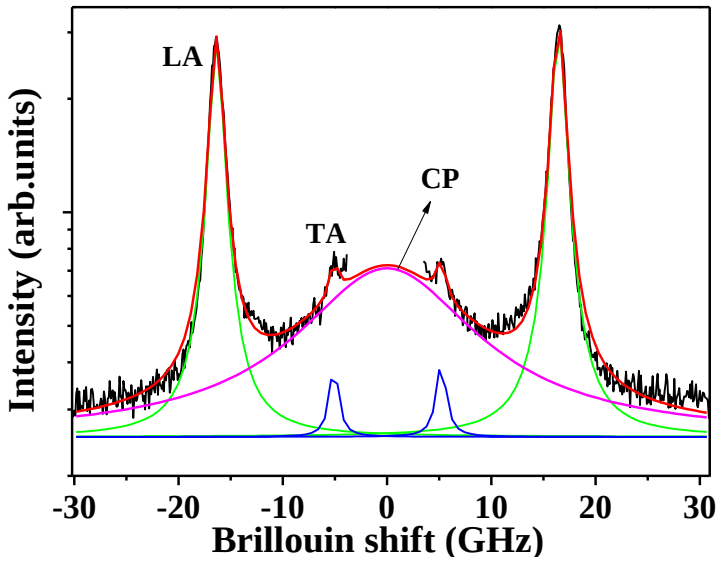


Fig. 3.3. Room temperature Brillouin spectra of evacuated ZIF-8 (LA-Longitudinal acoustic mode, TA-Transverse Acoustic mode, CP- Central Peak).

We have used 'envelop method' to determine the elastic constants from the ϕ dependence of Brillouin shifts. Envelop method is usually employed in deriving the elastic constants of the samples when the crystallographic orientation is unknown, especially in high pressure Brillouin experiments [23,24]. In such cases, Brillouin shifts from many experimental runs are obtained and envelop of the data thus obtained are assumed to represent the maximum and minimum values of the shift. This method can be used even when a phi dependent study is not possible with the major disadvantage being the uncertainty in determining the extreme values of the Brillouin shift. Figure 3.4(b) shows the phi dependence of the LA and TA modes in evacuated ZIF-8 displaying the maxima and minima in the Brillouin shifts, which will occur along certain crystallographic directions. The Brillouin shift and FWHM (full with at half maximum) were obtained by fitting the LA, TA and CP simultaneously using Lorentzian functions, as shown in Fig. 3.3. The independent elastic constants $C_{11}$, $C_{12}$ and $C_{44}$ of ZIF-8 can be determined from the maximum and minimum values of acoustic modes and density (ρ) using the following relations [25-27]:

$$V_{LA,max}^2 = C_{11}/\rho \text{ along } <100> \quad (3.1)$$

$$V_{LA,min}^2 = (C_{11}+2C_{12}+4C_{44})/3\rho \text{ along } <111> \quad (3.2)$$

$$V_{TA1,min}^2 = C_{44}/\rho \quad (3.3)$$

The minimum value of TA1 (Eq. 3.3) can be used to determine the minimum value of shear modulus, $G_{min} = C_{44}$ and the maximum value of LA determines $C_{11}$ (Eq. 3.1). Once $C_{11}$ and $C_{44}$ are known, $C_{12}$ can be derived from the minimum value of LA (Eq. 3.2). The elastic constants $C_{11}$, $C_{12}$ and $C_{44}$ thus obtained for evacuated ZIF-8 from our studies using a refractive index of 1.39 and density, 950 kg/m$^3$ are 9.4, 6.7 and 0.90 GPa, respectively which is in close agreement with the reported values of 9.52, 6.86 and 0.96 GPa [21]. The structure of the ZIF-8 do not change on introducing guests at room temperature [15,20,28] and hence we can use Eq. 3.1 to 3.3 to derive the elastic constants of guest incorporated ZIF-8 also.

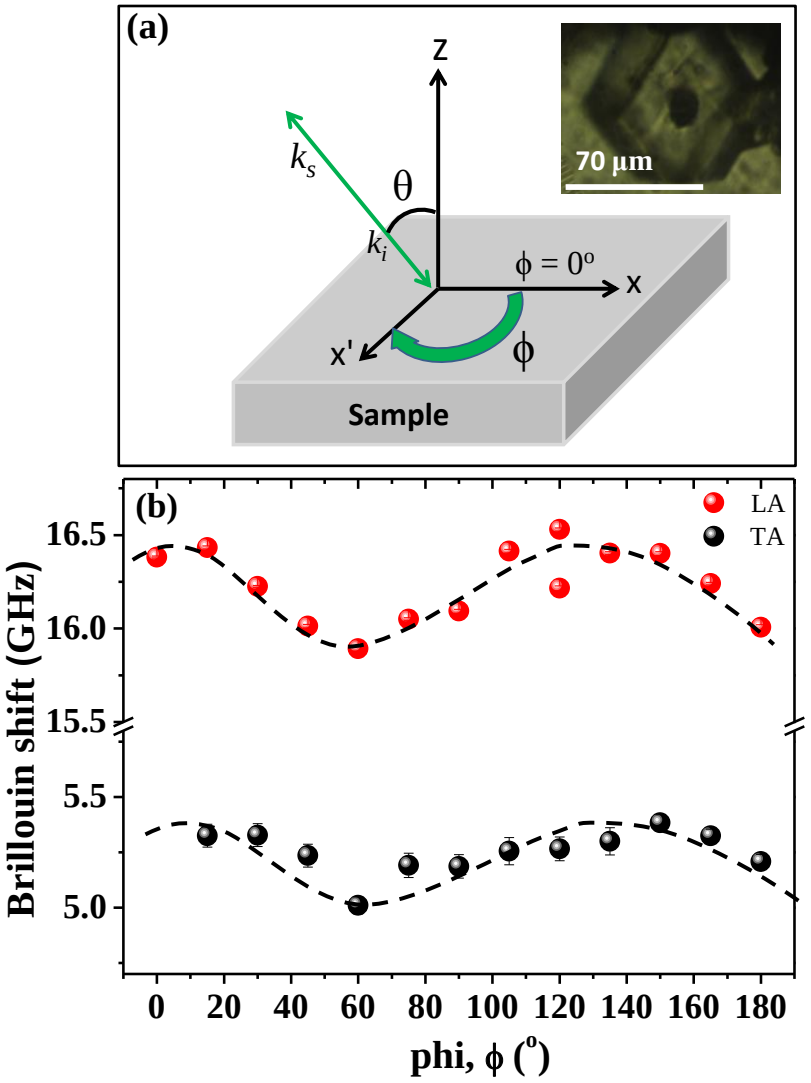


Fig. 3.4. (a) The schematic of the scattering geometry and phi dependent study on a ZIF-8 crystal. A random direction, x is taken as $\phi = 0^o$ and the sample is rotated azimuthally to a new direction x'. θ is the angle between the incident/scattered light ($k_i$ / $k_s$) and the normal (z). The inset shows the optical image of ZIF-8. (b) The phi dependence of LA and TA shift in evacuated ZIF-8 at room temperature. The dashed lines are guide to the eyes.

### 3.3.1. Solvent incorporation at room temperature

The presence of solvent, its mass, polarity *etc.* can affect the elastic properties of guest-host systems. To calculate the acoustic velocities and elastic constants, the refractive index and density of solvent incorporated ZIF-8 is required. The effective refractive index of solvent incorporated ZIF-8 can be calculated using the formula

$$n_{eff} = \sqrt{V_{sol} n_{sol}^2 + V_{fram} n_{fram}^2 + (1 - V_{fram} - V_{sol}) n_{vac}^2} \quad (3.4)$$

where $V_{sol}$, $V_{fram}$ are the volume fraction of the solvent and framework, respectively and $n_{sol}$, $n_{fram}$ and $n_{vac}$ are the refractive index of the solvent, framework and vacuum, respectively. From the thermo gravimetric analysis (TGA, Fig. 3.5(a)) the number of molecules per unit cell determined for methanol, ethanol, propanol, butanol and DMF incorporated ZIF-8 are 4, 4, 6, 8, 7, respectively. These molecules occupy a volume fraction of approximately 0.1 within the framework, considering their kinetic diameters. Refractive index of evacuated ZIF-8 was taken from the literature [29] and the anisotropy in the refractive index of ZIF-8 need not be considered as per the earlier reports [29,30] (due to its cubic structure). Also, we are only interested in the relative increase or decrease in elastic constants and not in the absolute value.

The density of solvent incorporated ZIF-8 can be obtained either from literature or from number of guest molecules determined using TGA. While the density of as-syn, evacuated, methanol and butanol incorporated ZIF-8 can be obtained from the literature, [11,15,21,28] some of the references has not taken into consideration the mass of the H atoms of the framework and the guests, for example density of butanol incorporated ZIF-8 [28]. Also, experimental conditions of Brillouin and density measurements (literature) are quite different. For example, in the case of methanol incorporated ZIF-8, density is obtained from the high pressure XRD experiment where the sample is surrounded by the methanol medium while our Brillouin experiments are performed in the absence of liquid medium surrounding the sample. Thus densities determined from the TGA measurements are more appropriate in determining the elastic constants. The effective refractive indices and the densities of the solvent incorporated ZIF-8 used in determining the elastic constants are given in Table 3.1. The Brillouin shifts, acoustic velocities and elastic constants of solvent incorporated and evacuated ZIF-8 are given in Table 3.2 and 3.3. The error in the Brillouin shifts were determined using the procedure given in Ref [31] using a

standard deviation of ~ 0.05 GHz (shifts given in Table 3.2 is the mean from 6 data) and an instrumental resolution of ~ 0.08 GHz.

Table. 3.1. The refractive index and density of guest incorporated ZIF-8. Polarisabilities of guests are also shown. The first line and second line in the refractive index of each sample corresponds to refractive index obtained by assuming a pore occupancy of 0.25 (from Ref [29]) and 0.1 (from TGA), respectively. The first line and second line in the density corresponds to the values obtained from literature and present measurement, (*i.e.* from the determination of the number of molecules present in a unit cell from the TGA measurements. Mass of $C_8H_{12}N_4Zn$= 229.6 amu and Z=12) respectively.

| Guest | Refractive index | Density ($kg/m^3$) | Polarizability ($Å^3$) |
|---|---|---|---|
| Evacuated | 1.39 | 950[a]<br>924 | |
| Methanol | 1.457<br>1.417 | 1056[b]<br>967.6 | 4.84 |
| Ethanol | 1.464<br>1.419 | -<br>977.8 | 5.13 |
| 1-propanol | 1.469<br>1.422 | -<br>1045.5 | 6.96 |
| 1-butanol | 1.473<br>1.424 | 1116[c]<br>1123.5 | 8.79 |
| DMF | 1.481<br>1.434 | 1141[d]<br>1.97.4 | 11.56 |
| $CO_2$ | 1.39 | - | 2.91 |
| $N_2$ | 1.39 | - | 1.74 |
| Ar | 1.39 | - | 1.64 |

[a]Reference [20,21], [b]Reference [15], [c]Reference [28], [d]Reference [11]

Table. 3.2. The Brillouin shifts, full width at half maximum (FWHM) of the longitudinal acoustic mode (LA) as well as the central peak (CP) of evacuated and solvent incorporated ZIF-8 at 298 K.

| Sample | LA[max/min] (GHz) | TA[min] (GHz) | FWHM–LA (GHz) | CP (± 2 GHz) |
|---|---|---|---|---|
| As- syn | 17.11/16.89 | 5.22 | 1.833±0.12 | 13 |
| DMF | 17.87/17.60 | 5.28 | 2.05±0.12 | 13 |

| | | | | |
|---|---|---|---|---|
| methanol | 16.43/16.25 | 5.14 | 0.99±0.08 | 12.5 |
| ethanol | 16.58/16.41 | 5.02 | 0.91±0.06 | 7.4 |
| 1-propanol | 16.31/16.18 | 5.21 | 1.4±0.07 | 8 |
| 1-butanol | 16.37/16.19 | 5.14 | 1.33±0.08 | 9 |
| Evacuated | 16.43/15.89 | 5.06 | 1.258±0.14 | 17 |
| Evacuated[a] | - | - | - | - |

[a]Reference[21]

The decrease in the Brillouin shift of as-syn ZIF-8 on evacuation indicates the role of guest molecules in strengthening the framework as predicted by *Ortiz et al.*[32] Upon re-adsorption of DMF, the observed shift is higher than that of as-syn ZIF-8, probably because as-syn ZIF-8 has both DMF and water molecules inside while on re-adsorption only DMF molecules are present [11]. This demonstrates the permanent porosity character of ZIF-8 as well as the nature of the guest in determining the elastic properties of the framework. This also gives the evidence for the presence of guest molecules in the pores and its interaction with the framework.

The XRD studies in methanol and butanol incorporated ZIF-8 has shown that there are 12 molecules of each per unit cell [15,28]. Assuming that ethanol and propanol incorporated ZIF-8 also have 12 molecules per unit cell, elastic constants determined will increase on increasing the chain length which implies that the trend in the elastic constants will not change even if experimental values of the density are used, though their values may differ.

For alcohol incorporated ZIF-8, on increasing the chain length the acoustic velocity decreases. The elastic constants increase as n increases from 1 to 4 with DMF incorporated ZIF-8 (DMF@ZIF-8) exhibiting the highest elastic constants. On introducing solvents, $C_{12}$ exhibits a huge increase when compared to other elastic constants as it increases by approximately 44% and 25% for DMF@ZIF-8 and butanol incorporated ZIF-8 (butanol@ZIF-8), respectively when compared to the evacuated ZIF-8. ZIF-8 is elastically anisotropic with the maximum value of Young's modulus (E) along <100> direction and minimum along <111> direction [21]. The Young's modulus determined along these directions is shown in Table 3.3 [26]. It can be observed that E<111> increases on incorporating solvents, which can be accredited to the increase in $C_{12}$. The <111> direction is normal to the six-membered rings of ZIF-8 which is a major

guest occupation site [21]. An increase in E<111> thus gives an indirect evidence for the guest adsorption near the six-membered rings of ZIF-8. Also the difference between E<100> and E<111> decreases on incorporating the guests which indicates a decrease in the anisotropy of the Young's modulus.

Table. 3.3. The acoustic velocities, elastic constants and the extreme values of the Young's modulus (E) of evacuated and solvent incorporated ZIF-8 at 298 K. The first line in the acoustic velocities and elastic constants of each sample corresponds to the values determined using the density and pore occupancy obtained from literature, while the second line corresponds to the same determined from our experiments.

| Sample | $V_{max}/V_{min}$ (± 0.006 km/s) | $C_{11}$ (± 0.04 GPa) | $C_{12}$ (± 0.03 GPa) | $C_{44}$ (± 0.01 GPa) | E<100> (± 0.02 GPa) | E<111> (± 0.02 GPa) |
|---|---|---|---|---|---|---|
| As- syn | 3.072/3.051 | 10.77 | 8.37 | 1.00 | | |
| | 3.173/3.134 | 11.48 | 8.93 | 1.07 | 3.68 | 3.04 |
| DMF | 3.209/3.179 | 11.75 | 9.18 | 1.03 | | |
| | 3.314/3.265 | 12.05 | 9.42 | 1.05 | 3.79 | 3.00 |
| methanol | 3.002/2.936 | 9.52 | 7.33 | 0.93 | | |
| | 3.087/3.051 | 9.22 | 7.11 | 0.90 | 3.04 | 2.55 |
| ethanol | 3.013/2.964 | - | - | - | | |
| | 3.102/3.077 | 9.41 | 7.45 | 0.87 | 2.83 | 2.46 |
| 1-propanol | 2.954/2.923 | - | - | - | | |
| | 3.047/3.027 | 9.74 | 7.53 | 0.93 | 3.13 | 2.81 |
| 1-butanol | 2.959/2.925 | 9.77 | 7.51 | 0.96 | | |
| | 3.039/3.025 | 10.38 | 8.16 | 1.04 | 3.19 | 2.93 |
| Evacuated | 3.145/2.871 | 9.39 | 6.71 | 0.90 | | |
| | 3.145/3.041 | 9.15 | 6.52 | 0.87 | 3.73 | 2.45 |
| Evacuated[a] | 3.17/3.08 | 9.52 | 6.86 | 0.96 | 3.77 | 2.78 |

[a]Reference[21]

The decrease in the acoustic velocity on increasing the chain length of alcohols is similar to the behaviour exhibited by the clatharates and can be explained as a result of the

stiffening of the framework due to the guest-host interaction [33]. Mass and number of butanol and DMF molecules incorporated in ZIF-8 are almost same but the difference in the values of their elastic constants show that interaction between framework and guest indeed affects the elastic constants. DMF possess highest polarizability among the solvents used. Also it is shown from DFT calculations that the interaction between the ZIF-8 and alcohol increases as we go from methanol to butanol so are their polarisabilities [34]. Thus elastic constants increase as the polarizability of guest in ZIF-8 is increased. A high filling of the cage by the guests can also increase the elastic constants as it can buttress the cage larger. Thus the guest-host interaction as well as filling factor/high packing affects the elastic constants [35,36].

On increasing the chain length, FWHM also increases and DMF@ZIF-8 exhibits the maximum FWHM. A high FWHM indicate high attenuation coefficient or a low phonon life-time which indicates high phonon scattering due to the guest-host interaction. Thus an increase in the FWHM implies that the guest molecules can absorb and scatter the phonons by the coupling of vibrational modes of guest molecules with the acoustic modes of host [33,37]. Such changes in the FWHM results in low thermal conductivity in guest-host systems as exemplified by clatharate hydrates [33]. Similarly, the changes in FWHM in our study indicate that we can tune the thermal conductivity of ZIF-8 by incorporation of solvents.

It has to be mentioned that while obtaining the Brillouin spectrum, if liquid solvent surrounds the ZIF-8 and strong LA mode of solvent is also observed in the spectrum, the average value of LA shift and FWHM of ZIF-8 is ~ 17 GHz and ~ 1.4 GHz, respectively irrespective of the solvent incorporated. Moreover, the LA mode of the solvent disables the observation of the weak TA mode of ZIF-8 as the Brillouin shift of solvent overlaps with the TA of ZIF-8 (LA mode is at 8.1 GHz for DMF and for alcohols it increases from 5.6 to 6.8 GHz as the chain length is increased). So Brillouin experiments were performed after removing the extra liquid molecules by heating the capillary tube, so that LA of the solvent vanishes and TA of the ZIF-8 appears. Presence of solvents within the ZIF-8 was then ascertained from the TGA and FTIR spectra (Fig. 3.5). A strong peak at 1680 $cm^{-1}$ in the FTIR spectrum indicates the presence of DMF in as-synthesised ZIF-8, while O-H stretching peaks ascertains the presence of alcohol (in alcohol incorporated ZIF-8) and water (in as-synthesised ZIF-8 [11]). The high value of Brillouin shift exhibited by ZIF-8

when the liquid medium surrounds it (*i.e.* LA of the solvents are present) compared to when the extra liquid is removed (Table 3.2) could be probably due to the hyper saturation of the pores of ZIF-8. Using the density of the methanol incorporated framework obtained from the high pressure XRD [15] measurement and the density of butanol incorporated ZIF-8, [28] the elastic constant $C_{11}$ determined from a Brillouin shift of 17 GHz for methanol and butanol incorporated ZIF-8 is ~ 9.9 GPa and 11.1 GPa, respectively which again follows the trend of increase in the elastic constants on increasing the chain length.

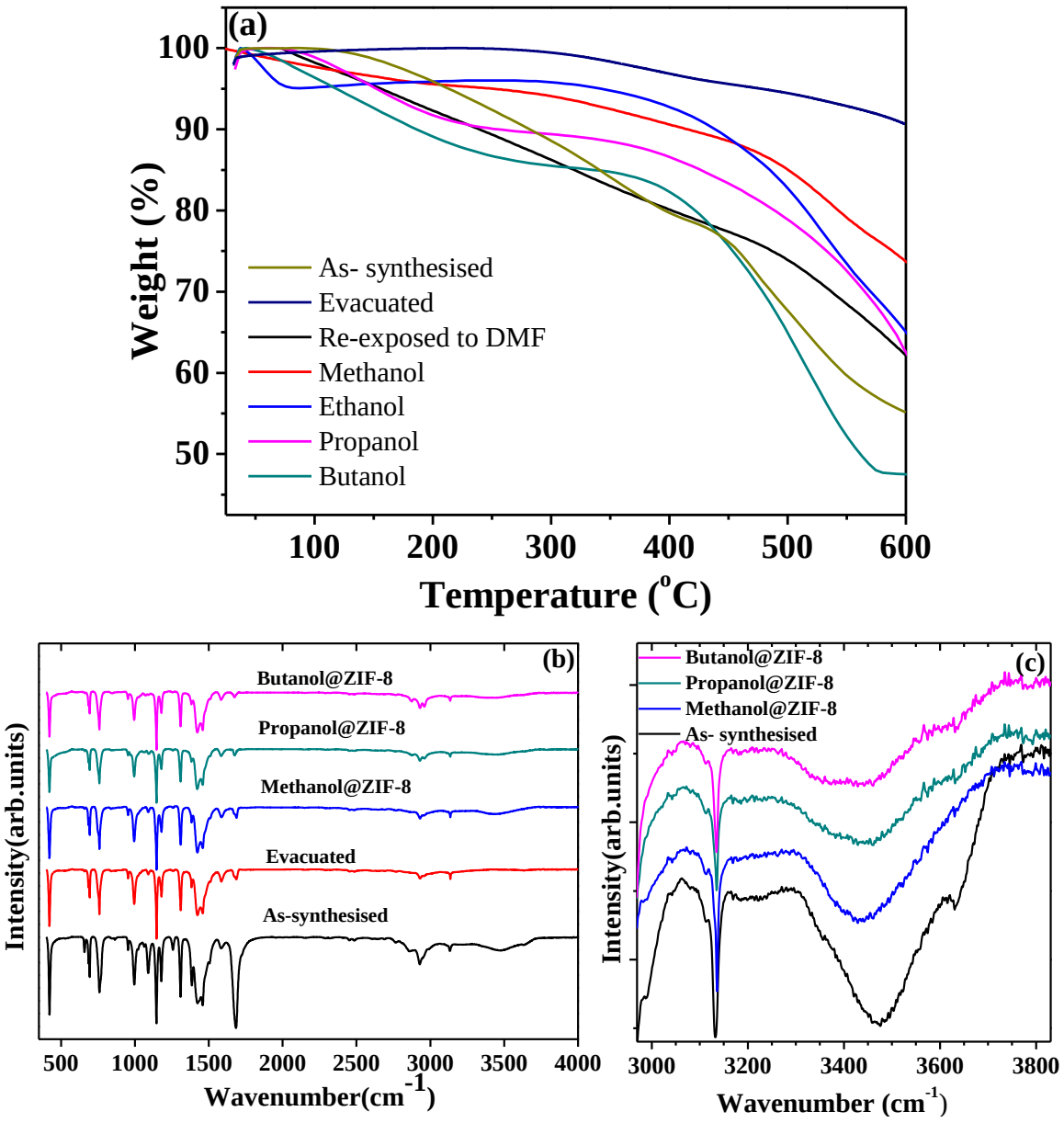


Fig. 3.5. (a)Thermo gravimetric analysis of solvent incorporated ZIF-8. (b) The FTIR spectra of solvent incorporated ZIF-8 and (c) the O-H stretching region of the same. The guest incorporated ZIF- 8 is represented as guest@ZIF-8.

### 3.3.2. Gas adsorption

We now focus on the temperature dependent gas adsorption studies. Ideally to determine the elastic constants, one has to study the phi dependence of the LA and TA modes. In our setup we cannot study the phi dependence of these crystals inside the cryogenic stage and hence the elastic constants could not be directly determined. On introducing guests, the difference between the maximum and minimum values of Brillouin shift of LA mode decreases (Table 3.2). Considering the velocities obtained as $V_{LA,max}$ and $V_{TA,min}$ the elastic constants $C_{11}$ and $C_{44}$ can be obtained, even though the values thus determined will have an error of ~ 3%. Hence the changes in LA and TA can be correlated as the changes in $C_{11}$ and the shear modulus $C_{44}$, respectively.

Figure 3.6 shows the Brillouin spectra of gas adsorbed ZIF-8 compared to the evacuated ZIF-8 at room temperature. It can be seen that the average value of Brillouin shift decreases upon exposing to various gases. At 298 K, a gas pressure of 1 atm results in the decrease of TA and LA shifts by ~ 5% and 3% respectively, independent of the gas, implying that TA modes are more pliable (Table. 3.4). The decrease in the Brillouin shift could be due to the increase in the cell and pore volume pertaining to the intake of gas, analogous to the high pressure experiments [15]. Raman experiments done under similar conditions did not show any change on guest incorporation implying that the pore occupancy plays a significant role in the mechanical properties of ZIF-8 and the microscopic properties are unaltered.

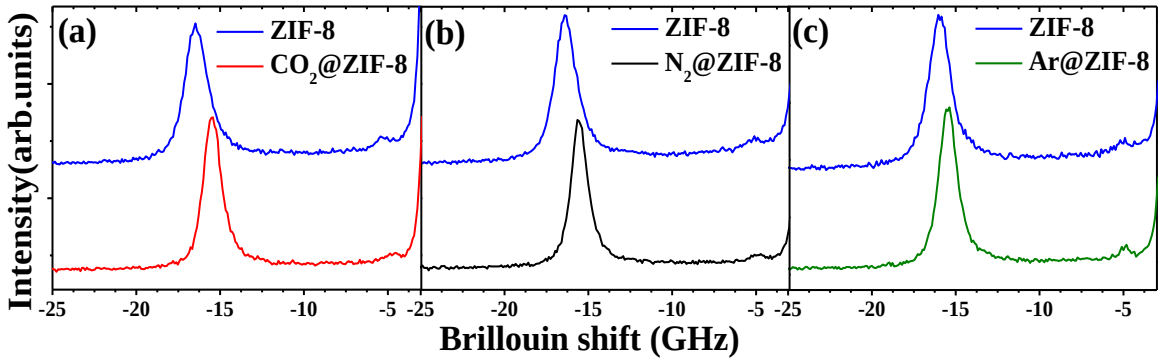


Fig. 3.6. The Brillouin spectra of evacuated and gas adsorbed ZIF-8 (represented by gas@ZIF-8) at room temperature.

Temperature dependent Brillouin shift and FWHM of LA mode for nitrogen adsorption is shown in Fig. 3.7(a, b). Both shift and FWHM shows significant changes near 260 K and

150 K. The changes near 260 K probably indicate the onset of significant gas uptake, as at the room temperature only a few molecules will be adsorbed [13,38] while the changes at 150 K is attributed to the rotation of methyl-imidazolate linker which further increases the amount of gas adsorbed. Temperature dependent Raman studies shows that major changes occur in imidazolate ring puckering mode upon adsorbing gases [18] since the gas molecules are adsorbed near the imidazolate linkers. Figure 3.8(a) shows the ambient temperature Raman spectra of evacuated ZIF-8 with bands assigned using Ref [18]. The temperature dependence of the imidazolate ring puckering mode shown in Fig. 3.8(b), display significant changes at 260 K and 150 K. This manifests the role of imidazolate linker in determining the elastic properties of ZIFs as well as the ability of Brillouin spectroscopy for capturing the flexibility of ZIF-8. The imidazolate ligands determines the stiffness in ZIFs as a bulkier linker results in higher stiffness [10]. The changes in the LA shift observed here illustrate the dependence of elastic constants particularly $C_{11}$, on the imidazolate linker as it becomes bulkier upon adsorbing gas.

Table. 3.4. The average values of Brillouin shift and FWHM in gas incorporated ZIF-8 at room temperature.

| Gas | LA (GHz) | TA (GHz) | FWHM of LA (GHz) |
|---|---|---|---|
| Ar | 15.63 ± 0.04 | 4.97 ± 0.09 | 1.193 ± 0.11 |
| $N_2$ | 15.59 ± 0.07 | 4.99 ± 0.07 | 1.158 ± 0.03 |
| $CO_2$ | 15.51 ± 0.1 | 4.97 ± 0.06 | 1.156 ± 0.05 |

During temperature dependent gas adsorption studies, temperature and gas uptake changes simultaneously. Incorporating guests increases the elastic properties in many porous materials, zeolites and ZIF-8 [32,36,39,40] while decreasing the temperature can also increase the elastic constants due to the increase in the bond strength. To separate the effects due to temperature and guest uptake, Brillouin experiments were performed at a constant temperature and varying gas pressure. The Brillouin spectra obtained at 77 K on increasing the $N_2$ gas pressure (0, 0.5 and 1 atm) is given in Fig. 3.7(c). The adsorption isotherm at 77 K from Ref [18] shows that the amount of $N_2$ gas adsorbed by ZIF-8 corresponds 0, 125 and 350 $mLg^{-1}$ at 0, 0.5 and 1 atm, respectively indicating that the

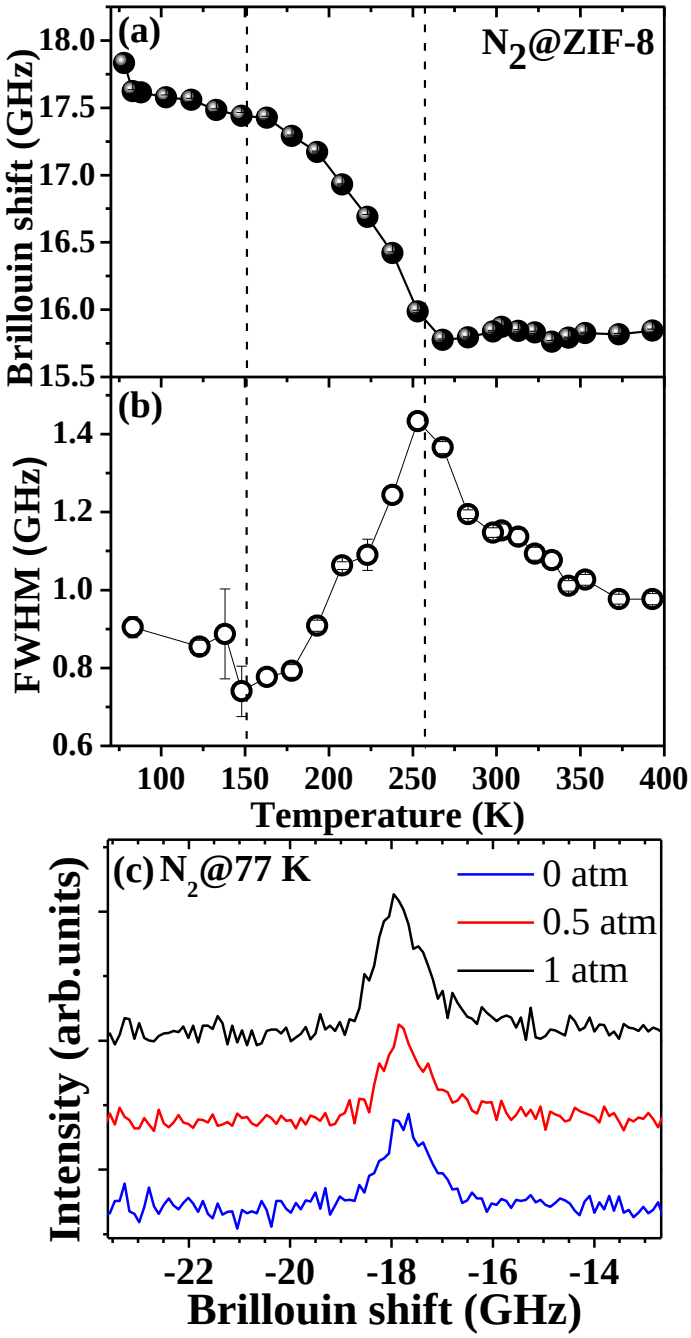


Fig. 3.7. Temperature dependence of (a) Brillouin shift and (b) FWHM of the LA mode during nitrogen adsorption.

number of gas molecules adsorbed by the framework increases on increasing the gas pressure. But Brillouin shift increases by only ~ 0.1 GHz on increasing the gas pressure from 0 to 1 atm. From the XRD measurements, the density of $N_2$ incorporated ZIF-8 corresponds to 1383 kg/m$^3$ (56 $N_2$ molecules per unit cell) [20]. On the assumption that the LA observed is LA,$_{max}$ the elastic constant $C_{11}$ estimated for 0 and 1 atm $N_2$ corresponds to 10.4 GPa and 15.5 GPa, respectively. At room temperature, $C_{11}$ is 9.1 GPa

for an evacuated ZIF-8 and hence the isothermal studies of elastic constants shows that temperature as well as the guest uptake effects the elastic constants with the guest incorporation being the dominant factor for increasing the elastic constants.

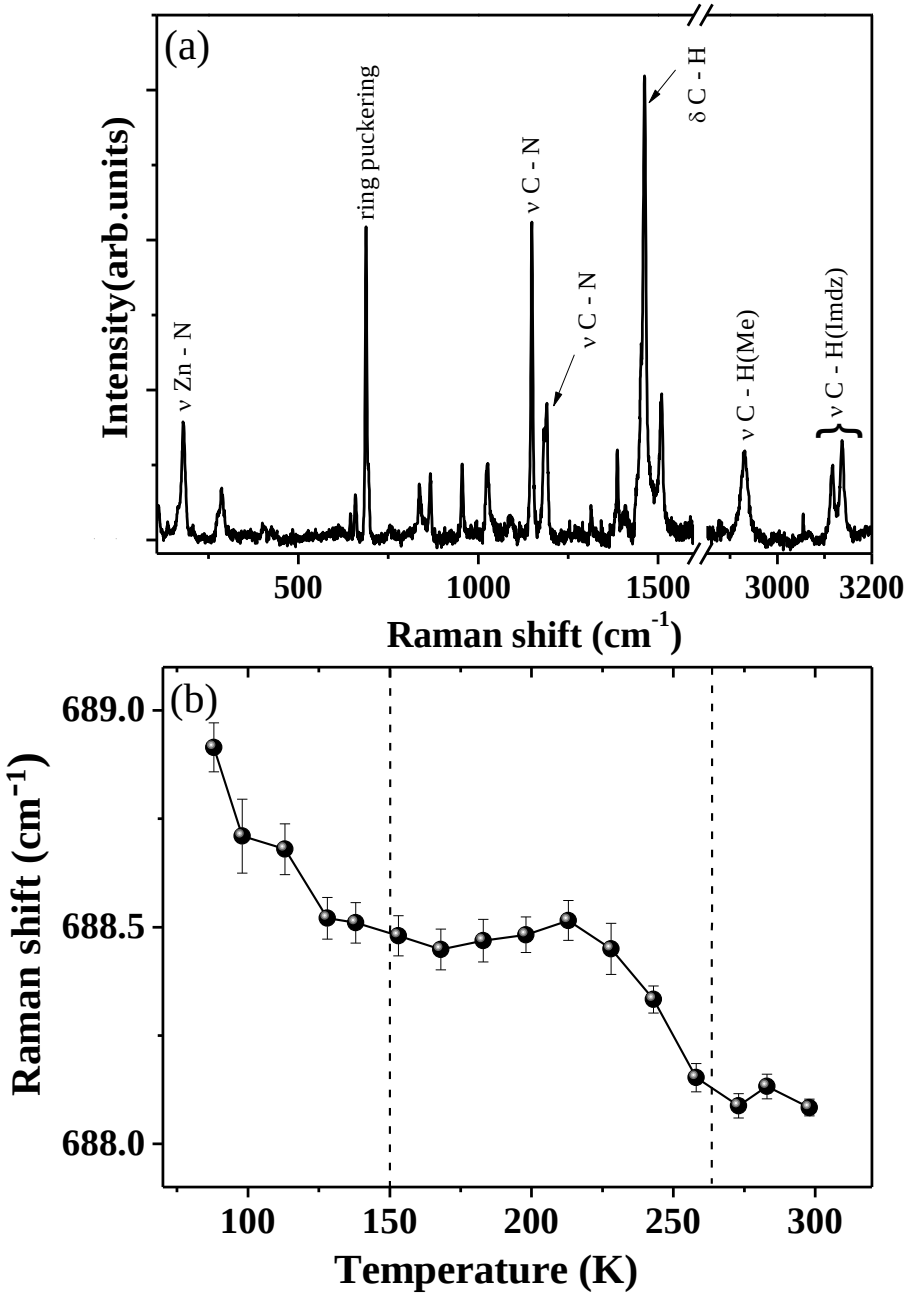


Fig. 3.8 (a) The Raman spectra of evacuated ZIF-8 at room temperature and (b) the temperature dependence of the imidazolate ring puckering mode upon $N_2$ adsorption.

Figure 3.9(a) shows the percentage of Brillouin shift of LA mode verses temperature for $N_2$, $CO_2$ and Ar adsorption. The temperature dependence was same for all the gases adsorbed upto 225 K, below which their behaviour deviates. Nitrogen adsorbed ZIF-8

($N_2$@ZIF-8) and Argon adsorbed ZIF-8 (Ar@ZIF-8) show changes near 260 K and 150 K pertaining to the beginning of significant gas uptake and gate opening, but interestingly shift of Ar@ZIF-8 saturates at a slightly lower value than $N_2$@ZIF-8. The Brillouin shift of carbon dioxide adsorbed ZIF-8 ($CO_2$@ZIF-8) increases steeply below 225 K and it does not show any saturation behaviour like $N_2$@ZIF-8 and Ar@ZIF-8. This could be due to the inability to study the behaviour of $CO_2$@ZIF-8 below the gate opening as $CO_2$ solidifies around 195 K. Gas adsorption depends upon the size, shape and polarity of the guest molecules and all the gases are adsorbed near the imidazolate ligands regardless of the nature of gas [12,41,42]. At 210 K, the LA shift decreases as the polarizability of the gas is decreased (*i.e.*, shift decreases in the order $CO_2$ > $N_2$ > Ar) similar to the case of solvent adsorption.

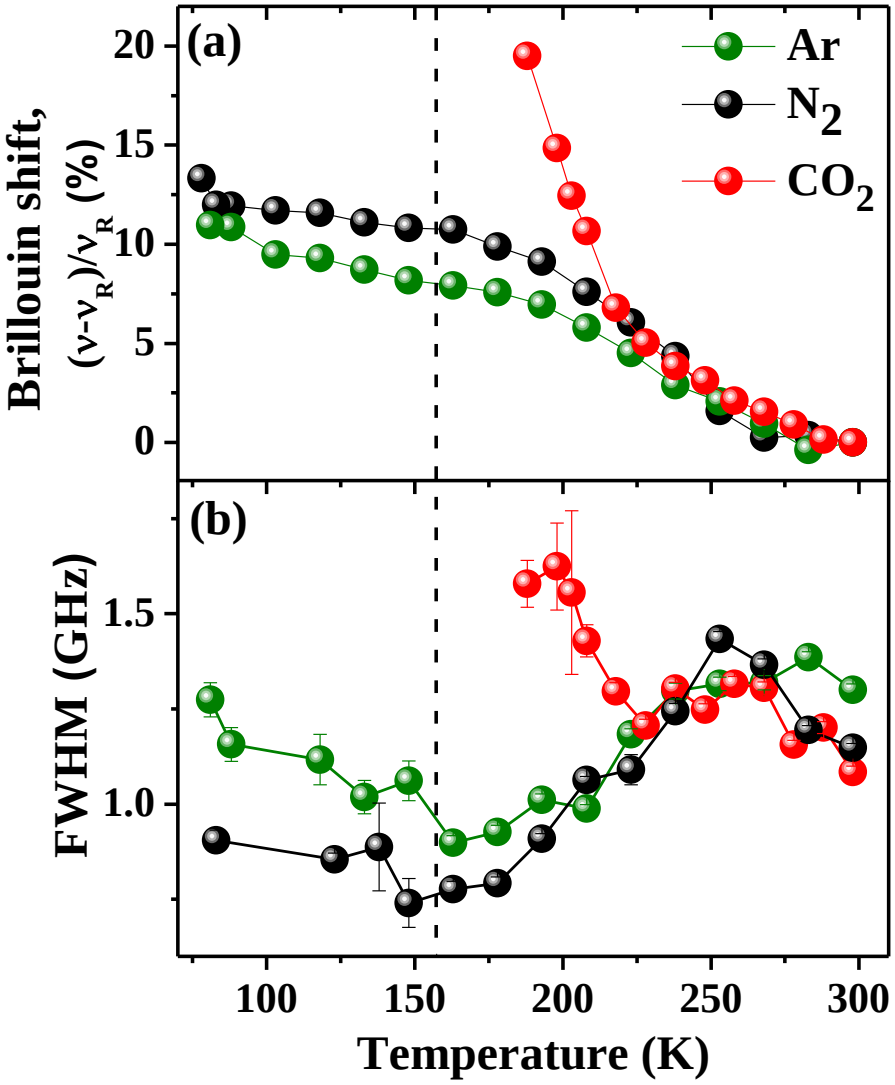


Fig. 3.9. Temperature dependence of (a) Brillouin shift and (b) FWHM of LA mode during $CO_2$, $N_2$ and Ar adsorption.

All gases follows similar trend in FWHM upto 225 K, though the peak at 260 K is not clearly observable for Ar adsorption (Fig. 3.9(b)). Below 230 K, FWHM for $CO_2$@ZIF-8 is seen to increase, similar to $N_2$ and Ar adsorption beyond 150 K. FWHM can be also an indicator of interaction between framework and guest as observed from our solvent incorporation studies. Since $CO_2$ interacts strongly with the framework due to its higher polarizability, it shows very strong increase in the FWHM. On the other hand, $N_2$ and Ar have similar polarisabilities and shows much reduced effect on FWHM and the minor changes in the two is within the experimental error bar.

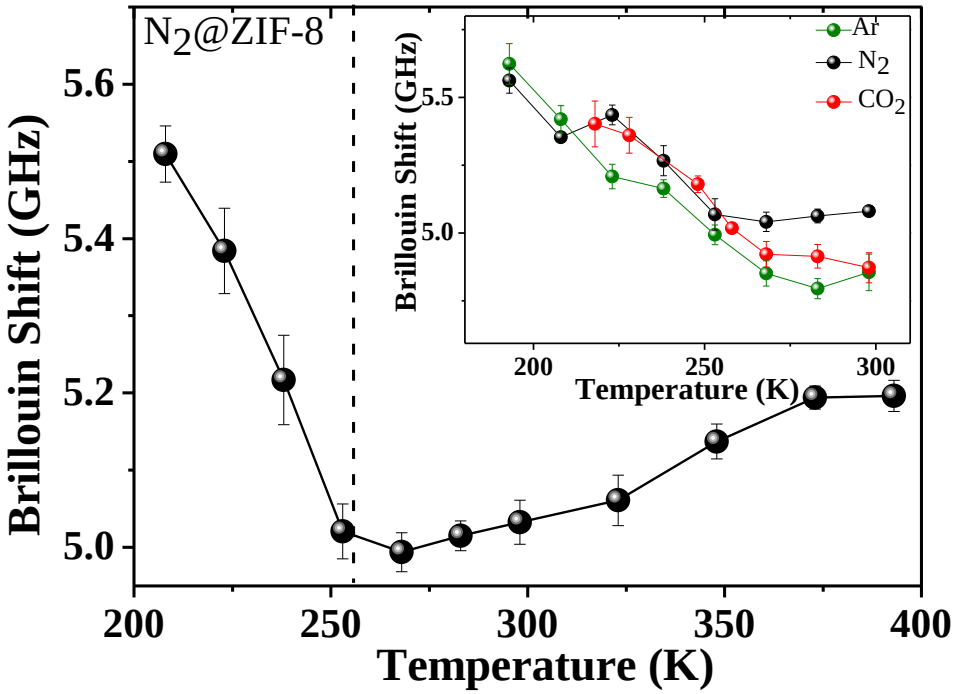


Fig. 3.10. Temperature dependence of TA1 for $N_2$ adsorption. Inset shows the temperature dependence for all the gases studied.

Figure 3.10 depicts the temperature dependence of TA mode of $N_2$@ZIF-8. TA mode decrease slightly as the temperature is decreased and then steeply increase below 260 K as significant gas adsorption commences, similar to the behaviour of LA mode. The temperature dependence of TA shift for all the gases shows similar behaviour upto 200 K (inset of Fig. 3.10), below which the TA modes disappeared. At 220 K the percentage Brillouin shift exhibited by TA modes is ~ 10 % whereas the LA modes exhibit only a 5 % change. This implies that the rigidity of framework against elastic distortions arising from external shear loading, undergoes a huge increase on decreasing the temperature [21]. Shear modulus of ZIF-8 which is the lowest observed at ambient conditions among

extended solids, decreases on decreasing the temperature and increases on adsorbing gas [21]. Though the elastic constants changes on decreasing the temperature, the Born stability conditions will be satisfied under all the experimental conditions investigated implying the mechanical stability of guest incorporated ZIF-8 [32,43].

### 3.3.3. Central peak

The central peak (CP, Fig. 3.3) also shows changes on guest incorporation (Table 3.2) and temperature. We could not determine the difference in FWHM of CP for n=2-4 alcohols as fitting of CP is prone to an error of ± 2 GHz. The CP can originate due to three factors: it can be (1) intrinsic to the sample, (2) intrinsic to the guest molecules or (3) due to the motion of the guest molecules within the framework.

CP intrinsic to the sample: FWHM of CP is related to the thermal diffusivity, $D_{th}$ by the relation $2D_{th}q^2 = \Gamma$ where $D_{th} = \frac{1}{3}V_D l$. Here, $q$ is the phonon wave vector, Γ is FWHM, $V_D$ is the average velocity and $l$ is the mean free path [44,45]. The mean free path of phonons in ZIF-8 ranges from 1.7-3.5 nm [46]. Assuming an average velocity of 1300 m/s, $D_{th}$ = 1.1x10$^{-6}$ m$^2$/s corresponding to a FWHM of ~ 0.4 GHz. Thus FWHM of the CP observed in our experiments cannot be attributed to the thermal conductivity of ZIF-8.

CP intrinsic to the guest molecules: Gases and liquids undergo various relaxation processes and exhibit CP in their Brillouin spectra. The CP due to the thermal fluctuations of gas molecules will be very narrow (FWHM ~ 1 GHz) [47,48] and that of solvent molecules will be very weak as even the LA modes of solvents are not observable in the Brillouin spectra [49]. Thus CP observed cannot be attributed to the intrinsic relaxation of guest molecules. Hence we believe that CP originates due to the motion of the guest molecules within the framework and its interaction with the framework.

Guest molecules can undergo two kinds of motion whereby it can interact with the MOF. The guest molecules can hop from one pore to another through the connecting windows (interpore hopping) or it can collide with the pore walls of the ZIF-8 and is confined within the pores [50]. Using the FWHM (Γ) of the central peak, relaxation time can be derived from the relation $\tau = 1/\pi\Gamma$. Relaxation times thus obtained for evacuated (as well as gas adsorbed), methanol and butanol incorporated ZIF-8 are 18, 25, 35 ps, respectively. The FWHM (~ 17 GHz) and hence the relaxation time obtained for evacuated and gas

adsorbed ZIF-8 are similar because Brillouin experiments were not performed under vacuum conditions and evacuated ZIF-8 was exposed to air after evacuation. Assuming a diffusivity of ~ $10^{-10}$ $m^2/s$ for $CO_2$ in ZIF-8, we derive a relaxation time of ~ 20 ps using the formula $D = a^2/6\tau$ where $a$ can be approximated as ~ 1 Å [51,52] which is in agreement with the relaxation time obtained from our Brillouin spectra. But the relaxation time obtained from CP is agreeable with the calculated values only in the case of gases where diffusivity is of the order of $10^{-9}$ to $10^{-10}$ $m^2/s$. For alcohols, the self diffusivity ranges from $10^{-11}$ - $10^{-16}$ $m^2/s$ which is lower than the gases and it reduces as alkyl chain length is increased [53-55]. Moreover for the solvents, (unlike gases) the factors like adsorbate-adsorbate interaction, clustering *etc.*[56] becomes significant which makes it difficult to assign the CP to interpore hopping motion.

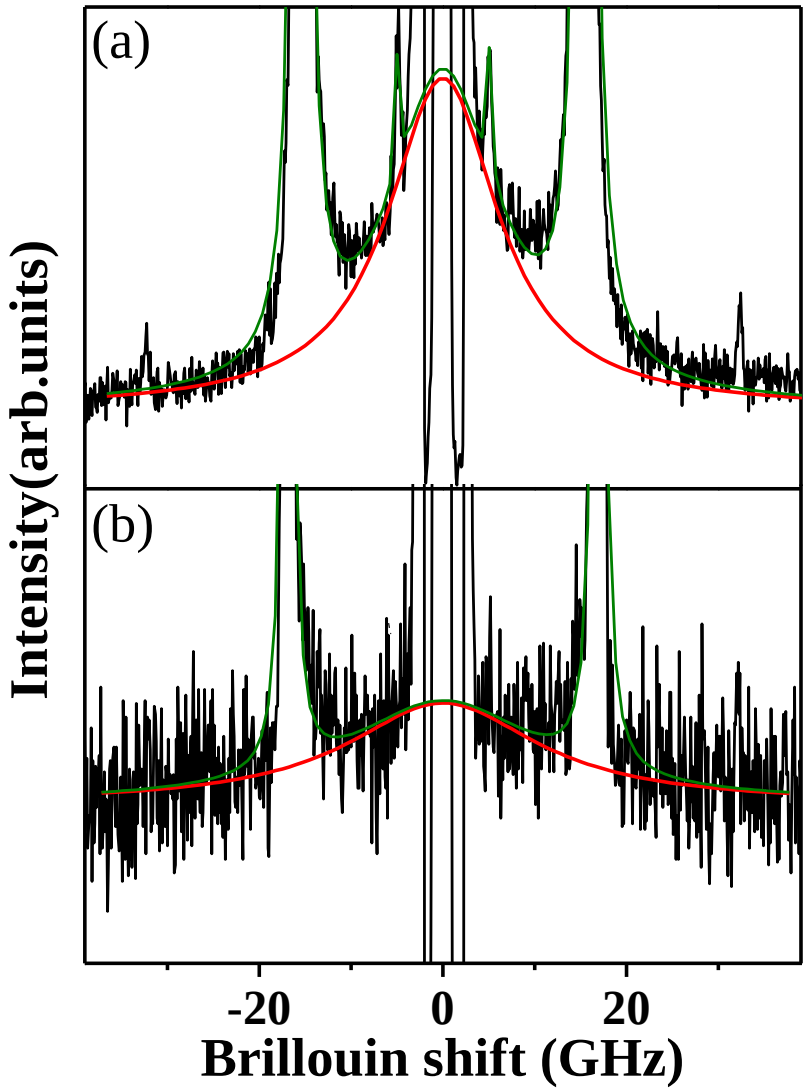


Fig. 3.11. The central peak (shown by red curve) observed during Ar adsorption studies in ZIF-8 at (a) 293 K and (b) 103 K. The spectrum in (b) has been enlarged by a factor of 5.

CP broadened and its intensity became very weak below 160 K during the gas adsorption studies (Fig. 3.11). In porous materials with windows, dimension of window have a huge impact on the diffusivity of the guest. The sudden broadening of the CP in ZIF-8HP phase thus indicates an increase in the diffusivity of the guest molecules as the window size enlarges [13,56]. This observation again proves that CP originates due to the interpore hopping motion of the guest molecules.

## 3.4. Conclusions

In conclusion, the effect of pore occupancy on the elastic properties of ZIF-8 has been studied by introducing various guests. The polarizability of the guests affects the elastic properties, life time and the guest dynamics inside the pores. The behaviour of the elastic constants suggests a decrease in the elastic anisotropy of ZIF-8 upon guest incorporation. The flexibility of ZIF-8 on gas adsorption was captured from the changes in the Brillouin shift and FWHM of the LA mode. On decreasing the temperature, we observe a large increase in shear modulus compared to the increase in the Young's modulus. The high shear stiffening observed at low temperatures can circumvent the shear induced amorphisation of ZIF-8 observed earlier. This could potentially catalyze the industrial applications of ZIF-8.

## 3.5. Bibliography

[1] P. Horcajada, R. Gref, T. Baati, P. K. Allan, G. Maurin, P. Couvreur, G. Férey, R. E. Morris, and C. Serre, Chemical Reviews **112**, 1232 (2012).

[2] H. C. Zhou, J. R. Long, and O. M. Yaghi, Chemical Reviews **112**, 673 (2012).

[3] J. C. Tan and A. K. Cheetham, Chemical Society Reviews **40**, 1059 (2011).

[4] F. X. Coudert, A. Boutin, A. H. Fuchs, and A. V. Neimark, The Journal of Physical Chemistry Letters **4**, 3198 (2013).

[5] S. S. Han and W. A. Goddard, The Journal of Physical Chemistry C **111**, 15185 (2007).

[6] M. Mączka, M. Ptak, and S. Kojima, Applied Physics Letters **104**, 222903 (2014).

[7] T. D. Bennett, J. Sotelo, J. C. Tan, and S. A. Moggach, CrystEngComm **17**, 286 (2015).

[8] P. Canepa, K. Tan, Y. Du, H. Lu, Y. J. Chabal, and T. Thonhauser, Journal of Materials Chemistry A **3**, 986 (2015).

[9] S. Henke, W. Li, and A. K. Cheetham, Chemical Science **5**, 2392 (2014).

[10] J. C. Tan, T. D. Bennett, and A. K. Cheetham, Proceedings of the National Academy of Sciences **107**, 9938 (2010).

[11] K. S. Park, Z. Ni, A. P. Côté, J. Y. Choi, R. Huang, F. J. Uribe-Romo, H. K. Chae, M. O'Keeffe, and O. M. Yaghi, Proceedings of the National Academy of Sciences **103**, 10186 (2006).

[12] C. O. Ania, E. García-Pérez, M. Haro, J. J. Gutiérrez-Sevillano, T. Valdés-Solís, J. B. Parra, and S. Calero, The Journal of Physical Chemistry Letters **3**, 1159 (2012).

[13] D. Fairen-Jimenez, S. A. Moggach, M. T. Wharmby, P. A. Wright, S. Parsons, and T. Düren, Journal of the American Chemical Society **133**, 8900 (2011).

[14] H. Tanaka, S. Ohsaki, S. Hiraide, D. Yamamoto, S. Watanabe, and M. T. Miyahara, The Journal of Physical Chemistry C **118**, 8445 (2014).

[15] S. A. Moggach, T. D. Bennett, and A. K. Cheetham, Angewandte Chemie **121**, 7221 (2009).

[16] Y. Hu, H. Kazemian, S. Rohani, Y. Huang, and Y. Song, Chemical Communications **47**, 12694 (2011).

[17] Y. Hu, Z. Liu, J. Xu, Y. Huang, and Y. Song, Journal of the American Chemical Society **135**, 9287 (2013).

[18] G. Kumari, K. Jayaramulu, T. K. Maji, and C. Narayana, The Journal of Physical Chemistry A **117**, 11006 (2013).

[19] M. A. Springuel-Huet, A. Nossov, F. Guenneau, and A. Gedeon, Chemical Communications **49**, 7403 (2013).

[20] J. P. Zhang, A. X. Zhu, and X. M. Chen, Chemical Communications **48**, 11395 (2012).

[21] J. C. Tan *et al.*, Physical Review Letters **108**, 095502 (2012).

[22] U. Ramamurty and J.-i. Jang, CrystEngComm **16**, 12 (2014).

[23] M. Grimsditch, P. Loubeyre, and A. Polian, Physical Review B **33**, 7192 (1986).

[24] H. Shimizu, H. Tashiro, T. Kume, and S. Sasaki, Physical Review Letters **86**, 4568 (2001).

[25] W. F. Hosford, *Mechanical Behavior of Materials* (Cambridge University Press, New York, 2005).

[26] R. E. Newnham, *Properties of Materials* (Oxford University Press Inc., New York, New York, 2005).

[27] R. L. W. Hayes, *Scattering of light by crystals* (John Wiley & sons, New York, 1978), p. 337.

[28] J. Cousin Saint Remi *et al.*, ChemSusChem **4**, 1074 (2011).

[29] G. Lu and J. T. Hupp, Journal of the American Chemical Society **132**, 7832 (2010).

[30] S. Eslava, L. Zhang, S. Esconjauregui, J. Yang, K. Vanstreels, M. R. Baklanov, and E. Saiz, Chemistry of Materials **25**, 27 (2013).

[31] L. Kirkup, *Data Analysis for Physical Scientists* (Cambridge University Press, New York, 2012), p. 205.

[32] A. U. Ortiz, A. Boutin, A. H. Fuchs, and F.-X. Coudert, The Journal of Physical Chemistry Letters **4**, 1861 (2013).

[33] H. Kiefte, M. J. Clouter, and R. E. Gagnon, The Journal of Physical Chemistry **89**, 3103 (1985).

[34] K. Zhang, L. Zhang, and J. Jiang, The Journal of Physical Chemistry C **117**, 25628 (2013).

[35] C. A. Sandstedt, D. Michalski, and C. J. Eckhardt The Journal of Chemical Physics **112**, 7606 (2000).

[36] L. Bouëssel du Bourg, A. U. Ortiz, A. Boutin, and F.-X. Coudert, APL Materials **2**, 124110 (2014).

[37] J. S. Tse, M. L. Klein, and I. R. McDonald, The Journal of Chemical Physics **81**, 6146 (1984).

[38] H. Huang, W. Zhang, D. Liu, B. Liu, G. Chen, and C. Zhong, Chemical Engineering Science **66**, 6297 (2011).

[39] R. Arletti, L. Leardini, G. Vezzalini, S. Quartieri, L. Gigli, M. Santoro, J. Haines, J. Rouquette, and L. Konczewicz, Physical Chemistry Chemical Physics **17**, 24262 (2015).

[40] B. Coasne, J. Haines, C. Levelut, O. Cambon, M. Santoro, F. Gorelli, and G. Garbarino, Physical Chemistry Chemical Physics **13**, 20096 (2011).

[41] Y. Liu, H. Liu, Y. Hu, and J. Jiang, The Journal of Physical Chemistry B **114**, 2820 (2010).

[42] J. Pérez-Pellitero *et al.*, Chemistry – A European Journal **16**, 1560 (2010).

[43] G. Grimvall, B. Magyari-Köpe, V. Ozoliņš, and K. A. Persson, Reviews of Modern Physics **84**, 945 (2012).

[44] A. Koreeda, T. Nagano, S. Ohno, and S. Saikan, Physical Review B **73**, 024303 (2006).

[45] A. Koreeda, R. Takano, and S. Saikan, Physical Review B **80**, 165104 (2009).

[46] X. Zhang and J. Jiang, The Journal of Physical Chemistry C **117**, 18441 (2013).

[47] T. J. Greytak and G. B. Benedek, Physical Review Letters **17**, 179 (1966).

[48] R. P. Sandoval and R. L. Armstrong, Physical Review A **13**, 752 (1976).

[49] J. H. Ko and S. Kojima, Journal of the Korean Physical Society **39** (2001).

[50] D. I. Kolokolov, L. Diestel, J. Caro, D. Freude, and A. G. Stepanov, The Journal of Physical Chemistry C **118**, 12873 (2014).

[51] L. Zhang, G. Wu, and J. Jiang, The Journal of Physical Chemistry C **118**, 8788 (2014).

[52] R. A. Field, D. A. Gallagher, and M. V. Klein, Physical Review B **18**, 2995 (1978).

[53] C. Chmelik, H. Bux, J. Caro, L. Heinke, F. Hibbe, T. Titze, and J. Kärger, Physical Review Letters **104**, 085902 (2010).

[54] J. A. Gee, J. Chung, S. Nair, and D. S. Sholl, The Journal of Physical Chemistry C **117**, 3169 (2013).

[55] K. Zhang, R. P. Lively, C. Zhang, R. R. Chance, W. J. Koros, D. S. Sholl, and S. Nair, The Journal of Physical Chemistry Letters **4**, 3618 (2013).

[56] R. Krishna, Chemical Society Reviews **41**, 3099 (2012).

# Chapter 4

# Guest dependent high pressure study of ZIF-8 using Brillouin and Raman spectroscopy

Dhanya Radhakrishnan and Chandrabhas Narayana "*Guest dependent Brillouin and Raman scattering studies of Zeolitic Imidazolate Framework-8 (ZIF-8) under external pressure"* J. Chem. Phy., 2016 (In press)

## 4.1. Introduction

Stability of a material under the application of high pressure is an important factor when considering whether a material can be used for industrial applications. Practical applications often expose the materials to significant external stresses making it highly desirable to investigate the mechanical properties of MOFs. Though pressure dependent x-ray diffraction (XRD) studies can be used to determine the bulk modulus, the elastic constants of MOFs have been studied only using computational approaches till now. Using XRD, Chapman *et al.* have shown that the bulk modulus of Cu-BTC framework depends on the type of pressure transmitting medium [1]. This indicates that the guest molecules play an important role in determining the mechanical properties of MOFs.

XRD studies show that ZIF-8 is highly compressible and undergoes irreversible structural transition and amorphisation when pressurized beyond 0.34 GPa either non-hydrostatically or hydrostatically (using a non- penetrating fluid) inside a diamond anvil cell (DAC) pressure, which deteriorates their adsorption properties [2]. Even though the lattice stability of ZIF-8 gets severely hampered under external pressure, it possess high chemical stability as demonstrated using high pressure Fourier transform infrared spectroscopy (FTIR) studies without any pressure transmitting medium (PTM) [3]. The XRD studies have demonstrated that in the presence of a pressure transmitting medium, which penetrates into the pores, (for example, methanol) ZIF-8 undergoes a transition around 1.47 GPa due to the rotation of the imidazolate linker which enlarges the size of the windows and the pore volume thus permitting more PTM into the pores [4]. The interaction between the PTM and ZIF-8 was believed to play an important role in this reversible crystalline to crystalline transition. The role of pressure in introducing more guest molecules inside ZIF-8 was also demonstrated by the enhanced storage of $CO_2$ using the FTIR investigations [5]. Using molecular dynamics (MD) simulation, Aure´lie *et al.* demonstrated that the pressure induced amorphisation in ZIF-8 is due to the mechanical instability arising from the shear softening. Moreover, the presence of guest molecules in ZIF-8 increases its resistance to the shear deformation which increases the pressure at which amorphisation occurs [6]. The root cause for the pressure induced mechanical failure of ZIF-8 is its low shear modulus (< 1 GPa), which is the lowest yet reported for any extended solid as evidenced from the Brillouin spectroscopy measurements at room temperature by Tan *et al* [7].

In this chapter, we have studied the pressure dependence of the acoustic modes of ZIF-8 using Brillouin spectroscopy in different pressure transmitting mediums as well as under non-hydrostatic conditions. Unlike the nanoindentation and the ultrasonic techniques, Brillouin spectroscopy is an ideal tool for determining the elastic constants of materials at ambient and extreme conditions especially when the sample size is very small. Raman spectroscopy has been demonstrated to give the molecular origin of the observed properties in MOFs under pressure, temperature and guest environments [8-10]. To support our Brillouin spectroscopy results, we have also used Raman spectroscopy to investigate the pressure induced changes in the local structure as well as signatures of guest-host interaction.

## 4.2. Experimental methods

The synthesis and characterisation of ZIF-8 is given in Chapter 3. Brillouin spectra were recorded in the backscattering geometry, using a 532 nm p-polarized excitation from a single longitudinal mode diode pumped and frequency doubled Nd-YAG laser with a power of 2 mW. The laser was focussed on the sample using a 20X objective lens. Scattered light was analyzed using a 3+3 pass tandem Fabry–Perot interferometer (JRS Scientific Instruments, Switzerland). The transmitted light was detected using a photo avalanche diode (SPCM-AQR-16, Perkin Elmer, Canada) and processed using a multi channel analyser with 1024 channels. A free spectral range of 43 GHz and an accumulation time of 10-15 min was used for recording the Brillouin spectrum. Raman spectra were recorded using a custom built Raman spectrometer using a 532 nm laser excitation and a grating of 1800 lines/mm (Chapter 2).

A membrane type diamond anvil cell with a culet size of 500 microns was used for the high pressure experiments. The pressure was controlled by a pneumatic drive system which uses helium gas. We have performed the high pressure experiments using two hydrostatic mediums - methanol: ethanol mixture in the ratio 4:1 and 1-propanol. Experiments were performed in non-hydrostatic condition also by filling the hole (~ 150 μm) only using ZIF-8 and without any PTM. Since the pressure range is very low, one could use large culet sizes of ~ 1 mm as well as sapphire anvils instead of diamond anvils. Due to non availability of these in our laboratory we have been doing such experiments in diamond anvil cells with very thick gaskets (pre-indented to a thickness of ~ 100 μm) as

well as with larger holes, where one can control the pressure changes very well in the very low pressure regime. We have been successful using DAC to elucidate many such low pressure phenomenons in the past. In addition the crystallite sizes have been ~ 70 μm, and spot size of the laser was about a few μm, hence using larger crystals do not help in a micro-Brillouin geometry. In-situ pressure was measured using the ruby fluorescence technique. In addition to the Brillouin and Raman spectra of ZIF-8, we have also obtained the spectra of PTM by focussing the light outside ZIF-8, in the PTM.

## 4.3. Results and discussion

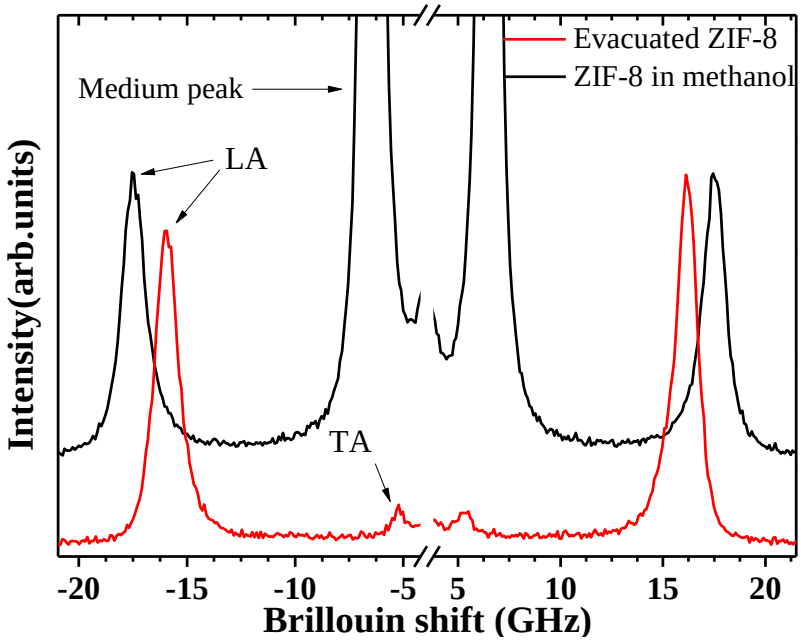


Fig. 4.1. The Brillouin spectra of ZIF-8 (evacuated and in methanol: ethanol pressure transmitting medium) at ambient conditions.

Figure 4.1 shows the Brillouin spectra of ZIF-8 in the presence and absence of hydrostatic medium (methanol-ethanol) at ambient conditions. The Brillouin spectrum of evacuated ZIF-8 consists of a strong longitudinal acoustic mode (LA) at ~ 16 GHz and a weak transverse acoustic mode (TA) at ~ 5 GHz. The TA mode obtained is very weak as the backscattering geometry used generally forbids its appearance. On introducing the hydrostatic medium, we could not observe the TA modes of ZIF-8 as it overlaps with the strong LA mode of PTM and hence the pressure dependence of the TA mode of ZIF-8 could not be studied. On introducing the hydrostatic medium, Brillouin shift of ZIF-8

increases by ~ 6% when compared to the evacuated ZIF-8. The Brillouin shift thus observed in the presence of excess solvent is higher than the case where the solvents are present only inside the pores of the ZIF-8 (as explained in the Chapter 3). This probably is because of the hyper-saturation of the pores and/or due to the adsorption of the solvents on to the outer surface of the framework as well.

Let us now focus on the high pressure Brillouin studies in methanol: ethanol PTM (Fig. 4.2(a)). Ideally, Brillouin shift increases on increasing the external pressure, which is accredited to the decrease in the cell volume upon pressurising. But here, on increasing the pressure Brillouin shift remains almost constant up to a pressure of 0.2 GPa. Under external pressure, ZIF-8 exhibits complex dynamics as observed in the high pressure XRD measurements by Moggach *et al.* using methanol-ethanol PTM [4]. In that case, on increasing the pressure it was observed that the pore as well as the cell volume increases upto 0.18 GPa and the PTM surrounding the sample was squeezed into the nanopore [4]. This is counter-intuitive to the usual trend where the cell volume decreases on applying external pressure. Hence the observed behaviour in Brillouin experiment can be explained as the competition between two processes: the first one being the increase in cell volume below 0.2 GPa as observed in the high pressure XRD experiment [4] which can decrease the Brillouin shift and the second one being the increase in the shift as a result of the incorporation of the guest molecules. These two processes compensate each other resulting in the constant Brillouin shift observed. Above 0.2 GPa, the Brillouin shift increases steeply. Around 1.3 GPa we observe two LA modes, shifted by ~ 2 GHz, existing simultaneously (Fig. 4.2(b)) and this indicates the coexistence of the two single crystalline phases. Above 1.4 GPa, we observe only one Brillouin peak (of higher value) which increases with increasing the pressure with a different slope. In the pressure dependent x-ray case on increasing the pressure above 0.18 GPa, the pore and the cell volume decreases as expected (the normal behaviour) although the number of methanol molecules inside the pore continues increasing and is followed by a transition at 1.47 GPa [4]. The crystal structure does not change during this transition, but the accessible pore volume increases due to a possible rotation of imidazolate linker, thereby inserting more methanol molecules inside the pore [4]. In fact, the number of methanol molecules inside the pores of ZIF-8 increases from only 12/unit cell at 0 GPa to 41/unit cell at 1.47 GPa [4]. Our Brillouin observation is consistent with this observation at 1.47 GPa in high

pressure XRD, which was implied due to the reoriented imidazolate ligands [4]. The fact that the Brillouin shift of the new phase is much higher than the earlier phase suggests that there is an increase in the elastic constant due to the influx of the guest molecule into the pores. The lower slope in the dω/dP also suggests that the pore will not have further uptake, but the pressure indeed is decreasing the overall volume of the MOF. Thus in the case of methanol-ethanol PTM, we observe that there is a two step process in the uptake of the medium, namely, one before the flipping of the imidazolate ligands and second after the flipping of the imidazolate ligands.

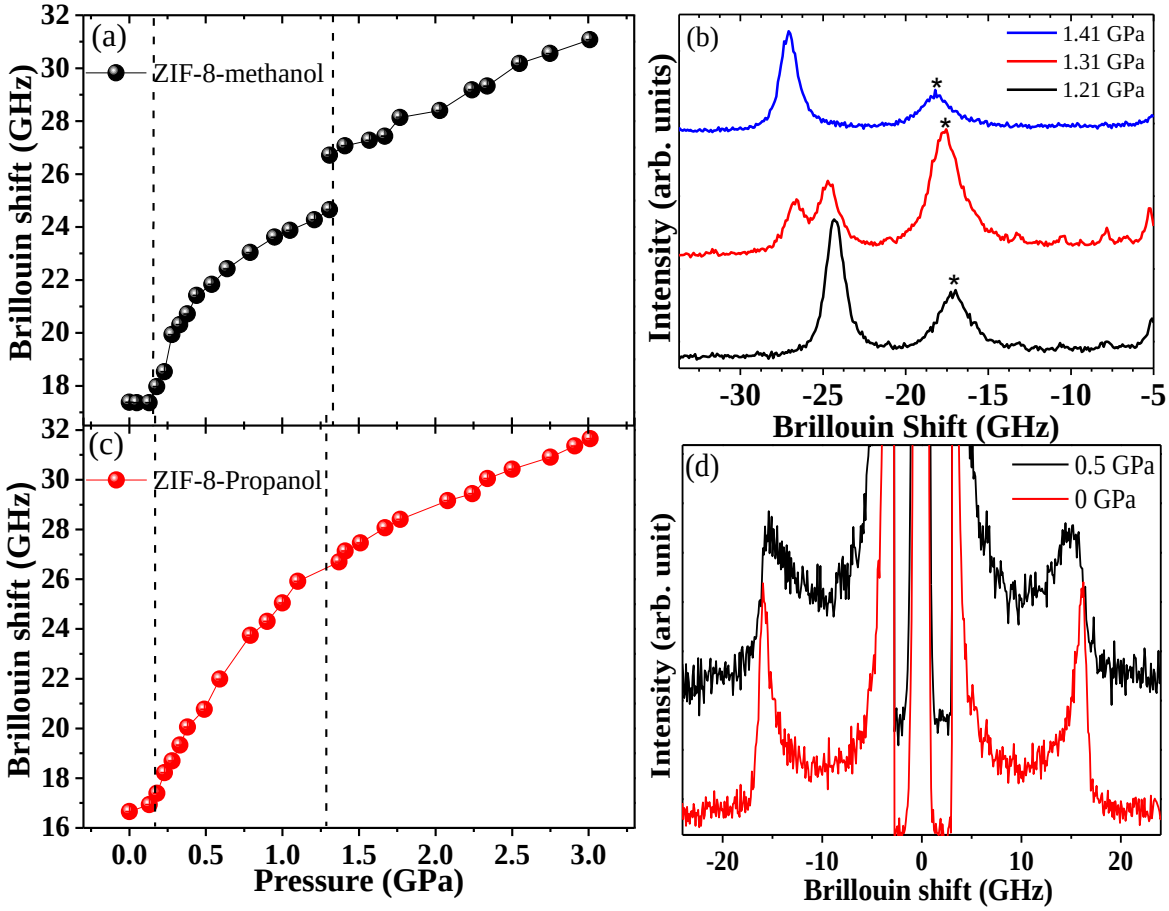


Fig. 4.2. The pressure dependence of LA mode of ZIF-8 in (a) methanol: ethanol and (c) propanol mediums. (b) The pressure evolution of ZIF-8 in methanol: ethanol PTM and (d) under the application of non-hydrostatic pressure. The * in (b) indicates the LA mode of the medium.

We now have used propanol as the PTM. It is interesting to see that the Brillouin shift of ZIF-8 remains unchanged till 0.2 GPa (Fig. 4.2(c)), similar to the earlier case. In this case also, there is a steep increase in the Brillouin shift above 0.2 GPa up to 1.4 GPa. Unlike in

the case of methanol-ethanol, we do not observe any splitting of LA in the case of propanol but only a slope change is observed at ~ 1.4 GPa. The behaviour of the Brillouin shift above 1.4 GPa for both methanol-ethanol and propanol PTM are almost same. In both the case, we do see there is a gate opening due to the flipping of the imidazolate ligands at 1.4 GPa, but it is interesting to see that in methanol-ethanol PTM we observe a sudden increase in the influx of the guest molecules. The absence of discontinuous jump in the Brillouin shift in the case of propanol PTM indicates that the nature of the PTM has an influence on the gate opening behaviour of ZIF-8. In ZIF-8, the 6-membered windows are one of the major guest adsorption sites [10,11]. Also, it is known that interaction between the guest and ZIF-8 increases as we increase the chain length of alcohol and hence propanol molecules can interact strongly with the framework compared to methanol [12]. The rotation of imidazolate ligands at high pressure (gate opening) results from the steric hindrance between the methyl groups which face each other within the windows [8]. At high pressures the steric hindrance becomes higher as the framework volume will be decreased, thus forcing the methyl-imidazolate linker to rotate and open the windows.

Compared to methanol (ethanol is only 20% percent in the methanol-ethanol mixture and hence neglected in this discussion), propanol molecules interact strongly with the framework leading to a smooth rotation of the methyl-imidazolate linker with a gradual intake of PTM, which results in the absence of discontinuity at the iso-structural phase transition in the case of propanol. Juxtaposed to this in the case of methanol, the interactions are weaker initially. But as more molecules are forced into the pores, the guest-host interaction increases, leading to a sudden flipping of the methyl-imidazolate linker followed by a sudden influx of PTM. This is the reason for the discontinuity as well as the coexistence of the two phases. High pressure Raman studies of ZIF-8 reported later in this chapter supports this interpretation.

Under non-hydrostatic conditions, LA mode softens and broadens on applying pressure. The Brillouin shift decreases by ~ 6% upon exerting a pressure of only 0.2 GPa. Further application of pressure results in the broadening of the peaks with peaks becoming weak above 0.5 GPa (Fig. 4.2(d)). This could be an indication of the impending amorphisation observed earlier [2]. Though there was no PTM, TA modes were not visible in this case also and an intense central relaxation peak was observed at zero frequency shift. The

absence of the TA mode could be due to the intense central relaxation peak which makes it difficult to de-convolute the TA from the Rayleigh component and the broad component of the central (ω = 0) peak. The appearance of the large central peak is an indication of the slow dynamics associated with the amorphisation.

Interestingly under hydrostatic conditions, Brillouin shift increases steeply as a function of pressure with the application of a moderate pressure of only 3 GPa. The final Brillouin shift observed in both the mediums was almost similar which indicates that external pressure squeezes the surrounding PTM into the pores of ZIF-8. The acoustic velocity can be determined from the Brillouin shift, $v$ using the relation $v = 2\frac{2\pi}{\lambda} n\, V \sin\theta/2$, where $n, \lambda, \theta$ are the refractive index, wavelength of the incident light and scattering angle, (= 180º) respectively (Eq. 1.11). Although ZIF-8 is elastically anisotropic [7], its anisotropy decreases on incorporating the guests (Chapter 3). Assuming elastic isotropy, the elastic constant $C_{11}$ can be derived from the longitudinal acoustic velocity using the relationship $C_{11} = V^2\rho$, where ρ is the density [13]. The pressure dependent density of methanol incorporated ZIF-8 can be obtained from the literature and can be extrapolated for different pressures [4]. The refractive index of the solvent incorporated ZIF-8 can be determined from the formula $n_{eff} = V_{sol}n_{sol} + V_{fram}n_{fram}$ where $V_{sol}$, $V_{fram}$, $n_{sol}$ and $n_{fram}$ are the volume fraction and refractive index of the solvent and framework, respectively. The refractive index and the volume fraction of the guest in ZIF-8 can be obtained from the Ref [14]. The pressure dependent refractive index of methanol can be obtained from the existing literature, [15] and the refractive index of ZIF-8 is assumed to be constant through-out the experiment for simplicity.

Figure 4.3 shows the pressure dependence of $C_{11}$ thus determined. On applying pressure, $C_{11}$ increases from ~ 11 GPa (at ambient pressure) to ~ 54 GPa (at 3 GPa). This amounts to ~ 400% increase in $C_{11}$ on applying a moderate pressure of only 3 GPa. It is interesting to note that such an increase with pressure is the highest ever observed in any material till now. The increase in the elastic constants depicts the role of guest-host interaction in enhancing the elastic properties of porous materials. In addition our results manifest that in the presence of interacting guest molecules, ZIF-8 approaches the elastic constants of its inorganic analogs- zeolites which ranges from 20 - 120 GPa [7].

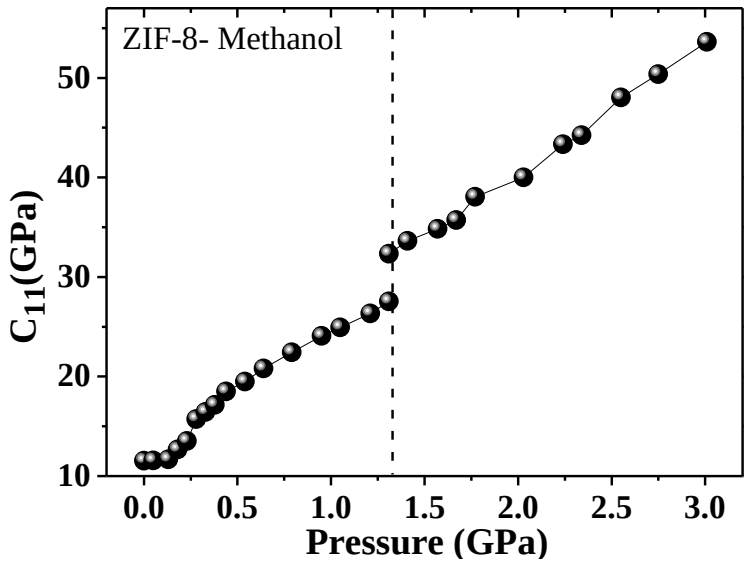


Fig. 4.3. The pressure dependence of the elastic constant $C_{11}$ in methanol: ethanol PTM.

Raman spectroscopy has been used in order to look for the microscopic origin of the pressure dependent effects observed in the Brillouin scattering studies. Figure 3.8(a) shows the Raman spectra of evacuated ZIF-8. The major Raman peaks of ZIF-8 are observed at [8,16]: 180 $cm^{-1}$ (ν Zn-N), 687 $cm^{-1}$ (Imdz ring puckering), 695 $cm^{-1}$ (ring puckering + C-H out of plane bend, represented as M1- see Fig 4.4(a)) 1146 $cm^{-1}$ (ν C− N), 1180 $cm^{-1}$ (ν C – N + N − H wag), 1187 $cm^{-1}$ (ν C – N), 1462 $cm^{-1}$ (C − H bending of methyl), 1509 $cm^{-1}$ (ν C− C), 2931 $cm^{-1}$ (methyl ν C – H ), 3114 $cm^{-1}$and 3138 $cm^{-1}$ (Imdz ν C − H). In addition to the ZIF-8 modes, we have also looked at the pressure dependence of the PTM entrapped in ZIF-8 which can be observed along with the ZIF-8 peaks in the Raman spectra and compared the results with the peaks associated with PTM outside ZIF-8 by recording the Raman spectra away from ZIF-8 crystal within the PTM. Figures 4.4(b, c) show the C-H stretching regions of ZIF-8 in the two PTMs depicting the framework and the peaks of PTM within the ZIF-8, in comparison with the intrinsic PTM peaks (outside the ZIF-8). Methanol has strong Raman peaks at 2835 $cm^{-1}$ and 2940 $cm^{-1}$ corresponding to symmetric stretching of C-H bonds and Fermi-resonant vibration of $CH_3$ bending while the corresponding modes in propanol are observed at 2877 $cm^{-1}$ and 2940 $cm^{-1}$, respectively [17,18]. Though C-H stretching modes of methyl group of ZIF-8 are also present at ~ 2900 $cm^{-1}$ [8], they are very weak when compared to the strong peaks of

the PTM and cannot be distinguished from them. The pressure dependence of PTM modes will be discussed after discussing the pressure dependence of the ZIF-8 modes.

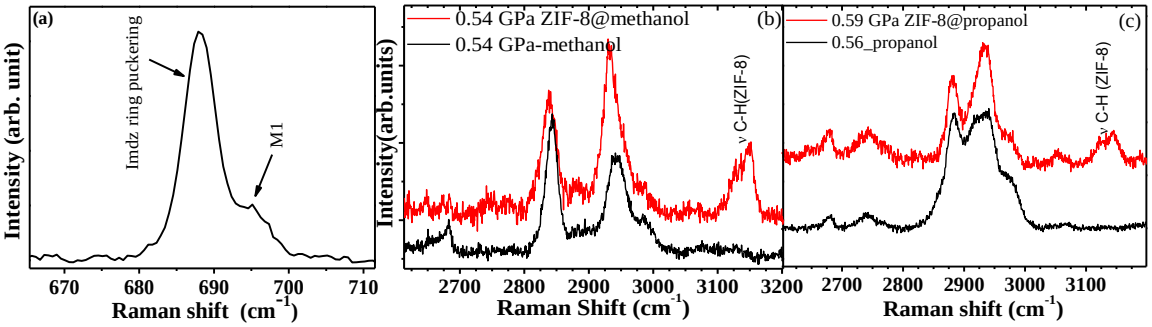


Fig. 4.4(a) Imidazolate ring puckering and M1 mode. The C-H stretching region of the Raman spectra for the PTM peaks – intrinsic (black) and within ZIF-8 (red) for (b) methanol: ethanol and (c) propanol mediums.

The pressure dependence of the imidazolate ring puckering, C-H bending and C-H stretching modes of ZIF-8 in methanol-ethanol and propanol PTM is shown in Fig. 4.5. In methanol PTM, changes were observed for these modes at ~ 0.2 and 1.4 GPa (Fig. 4.5(a-c)) with the transition at 1.4 GPa accompanied by a discontinuity in the Raman shift of C-H bending and stretching modes. In ZIF-8, major binding sites of the guests are near the organic linkers, contrary to the usual binding site near the metal entities as observed in most of the MOFs, for example MOF-5 [19-22]. This is evident from our Raman studies since most of the imidazolate modes undergo huge changes when subjected to external pressure. The sudden increase in the frequency shift of the C-H bending of the methyl group indicates the opening of the gates which reduces the steric repulsion between the methyl groups [8]. Moreover the C-H (Imdz) stretching (Fig. 4.5(c)) and C-N stretching peak (at 1146 $cm^{-1}$, Fig. 4.6(a)) soften suddenly by 10 $cm^{-1}$ and 4 $cm^{-1}$, respectively at 1.4 GPa. The sudden softening of these stretching modes can be attributed to the increased interaction between the methanol molecules and framework due to the large number of methanol molecules now present inside the pore. In propanol medium also, change in slope could be observed for few of the modes at ~ 0.2 and 1.4 GPa, but there were no discontinuity in the Raman shift, similar to those present in methanol PTM at 1.4 GPa through-out the pressure range investigated (Fig. 4.5(d-f)). The softening of the stretching vibrations of C-H (Imdz) and C-N at 1.4 GPa were also not observed (Fig. 4.5(f), Fig.

4.6(b)) implying a constant interaction between the framework and guest molecules. This is consistent with our high pressure Brillouin studies of ZIF-8 and validates our assumption there.

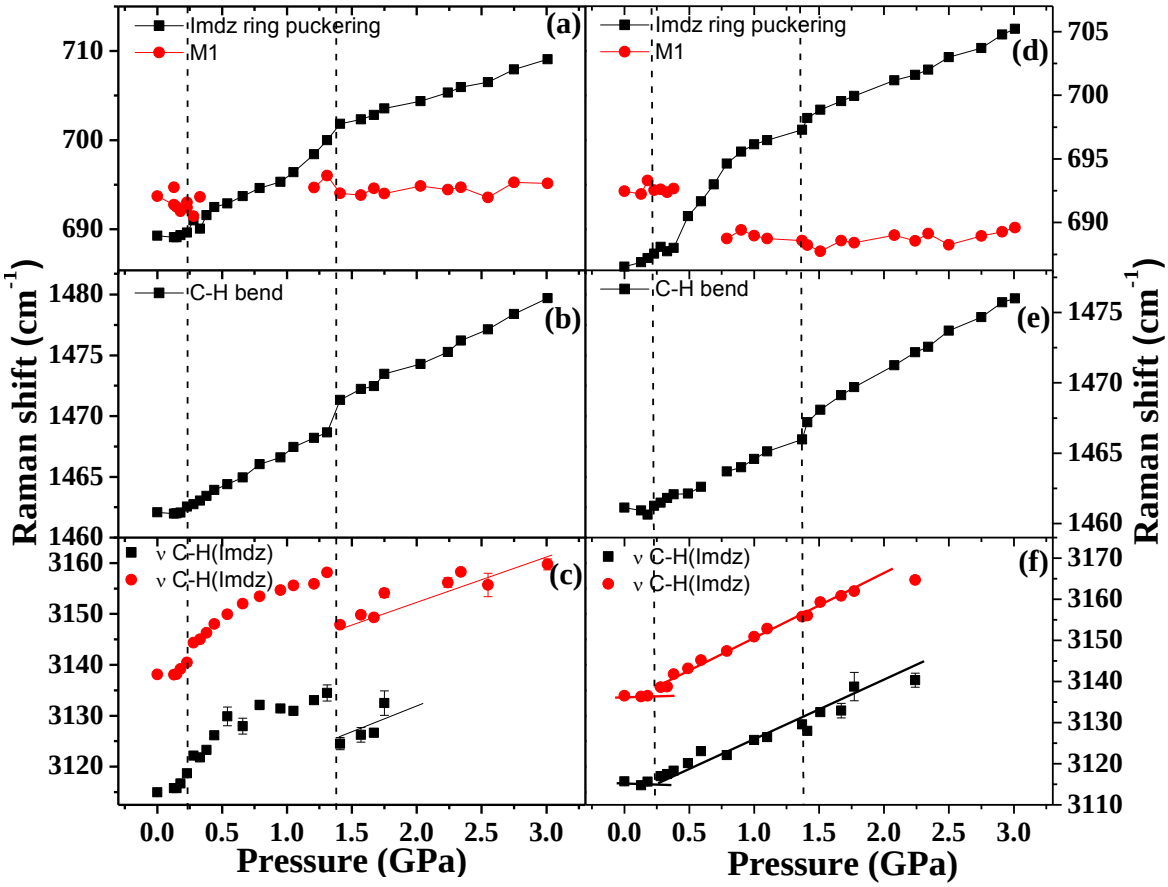


Fig. 4.5. The pressure dependence of the Raman modes of ZIF-8 in methanol: ethanol (a-c) and propanol (d-f) mediums. The vertical lines corresponds to the pressures 0.2 and 1.4 GPa.

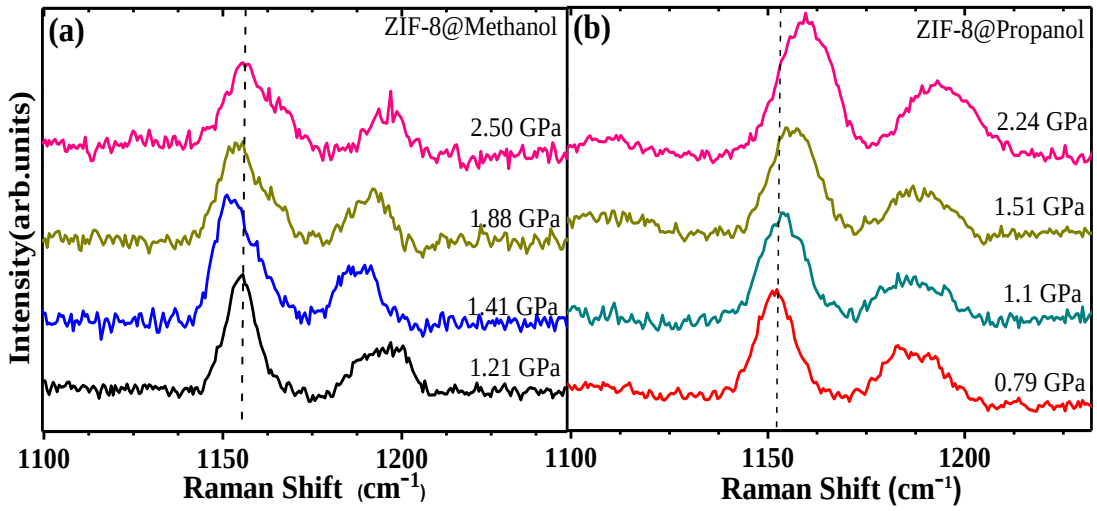


Fig 4.6. The evolution of Raman spectra of C-N stretching peaks in (a) methanol: ethanol and (b) 1-propanol pressure transmitting mediums.

In order to further understand the role of the interaction of the guest molecule with the framework we compared the Raman modes associated with the PTM within the MOF and outside the MOF. Figures 4.7(a, b) shows the pressure dependence of the Fermi resonant mode of the guest molecules within the framework in comparison to that of the molecules outside the framework. Compared to the Raman peaks of intrinsic PTM, the peaks of PTM within ZIF-8 are observed at a lower frequency. Both PTMs exhibits such behaviour and the decrease in frequency can be attributed due to the interaction between the guest and the framework which influences the bond stiffness [9,10]. For the entrapped methanol molecules, the transition at 1.4 GPa is accompanied by a sudden increase in the frequency of this mode as well as the emergence of a new peak at 240 $cm^{-1}$ (Fig. 4.7(c)). This could be attributed to the formation of methanol clusters inside the nanopore due to large number of methanol molecules which are now present at the centre of the pore [12,23].

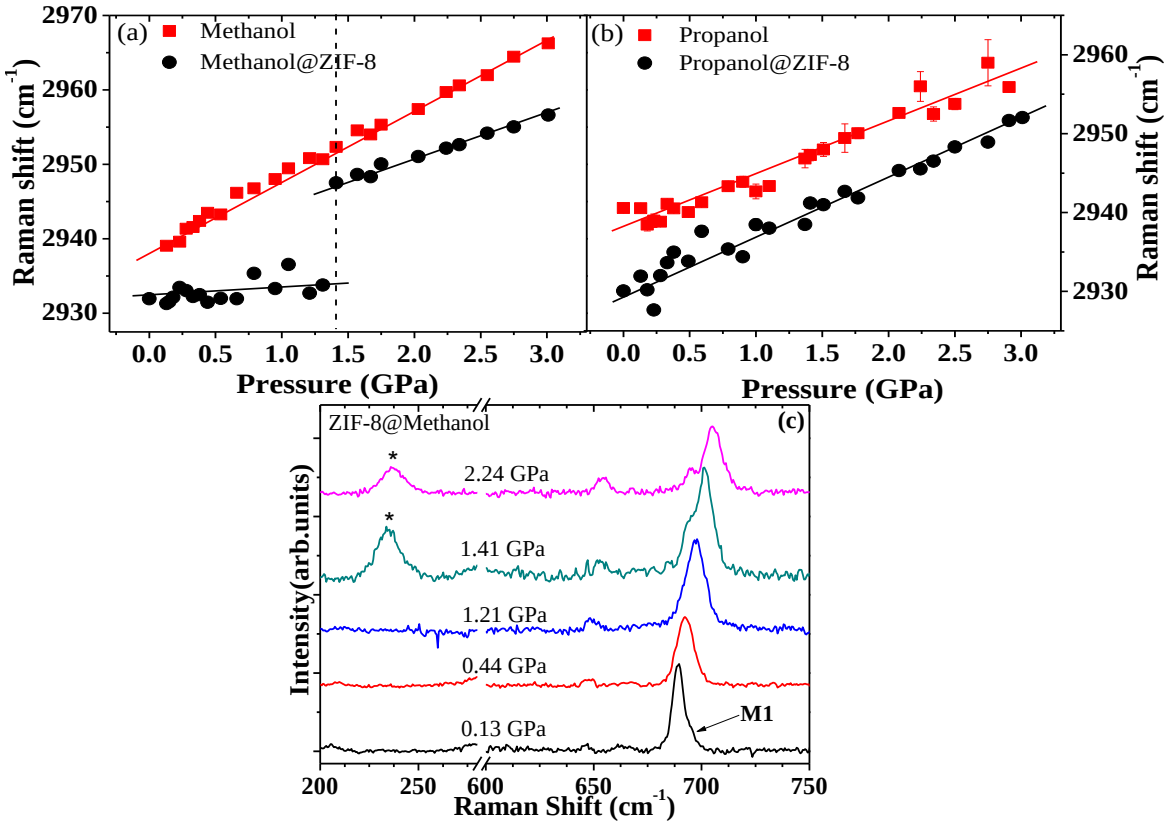


Fig. 4.7. The pressure dependence of the C-H Fermi resonance peak in (a) methanol: ethanol and (b) propanol mediums. The red and black colour represents the pressure dependence of the PTM mode outside and inside ZIF-8, respectively. (c)The evolution of Raman spectra in methanol: ethanol pressure transmitting medium showing the emergence of the peak at 240 $cm^{-1}$ after 1.4 GPa.

Unlike methanol, Raman shift of propanol mode increases linearly as the pressure is increased and no major changes occur in the pressure regime investigated. This implies a constant interaction between propanol and framework contrary to the interaction between methanol and ZIF-8. It has to be also mentioned that, the Brillouin shift of the LA modes of medium within ZIF-8 and outside were same for both the mediums unlike Raman and this suggests that the bulk properties of guests are unaffected, even though microscopically there is a definitive interaction.

## 4.4. Conclusion

We have studied the pressure dependence of Brillouin and Raman spectra of ZIF-8 using methanol: ethanol and propanol as pressure transmitting mediums. On applying external pressure, Brillouin shift increases resulting in an increase in the elastic constant $C_{11}$ by ~ 400%. This illustrates the role of guest in enhancing the mechanical properties of MOFs, as the PTM is squeezed into the nanopore by applying external pressure. The Raman and Brillouin studies also demonstrate that the PTM plays an important role in determining the flexibility and gate opening behaviour of ZIF-8. Two transitions (0.2 GPa and 1.4 GPa) were observed in ZIF-8 in both PTMs. The transition at 1.4 GPa was abrupt in the case of methanol, whereas it was gradual in propanol PTM which implies a smooth gate opening behaviour for the larger guest molecules, which interacts strongly with the framework.

## 4.5. Bibliography

[1] K. W. Chapman, G. J. Halder, and P. J. Chupas, J. Am. Chem. Soc. **130**, 10524 (2008).

[2] K. W. Chapman, G. J. Halder, and P. J. Chupas, Journal of the American Chemical Society **131**, 17546 (2009).

[3] Y. Hu, H. Kazemian, S. Rohani, Y. Huang, and Y. Song, Chemical Communications **47**, 12694 (2011).

[4] S. A. Moggach, T. D. Bennett, and A. K. Cheetham, Angewandte Chemie **121**, 7221 (2009).

[5] Y. Hu, Z. Liu, J. Xu, Y. Huang, and Y. Song, Journal of the American Chemical Society **135**, 9287 (2013).

[6] A. U. Ortiz, A. Boutin, A. H. Fuchs, and F.-X. Coudert, The Journal of Physical Chemistry Letters **4**, 1861 (2013).

[7] J. C. Tan *et al.*, Physical Review Letters **108**, 095502 (2012).

[8] G. Kumari, K. Jayaramulu, T. K. Maji, and C. Narayana, The Journal of Physical Chemistry A **117**, 11006 (2013).

[9] D. Y. Siberio-Pérez, A. G. Wong-Foy, O. M. Yaghi, and A. J. Matzger, Chemistry of Materials **19**, 3681 (2007).

[10] J.-P. Zhang, A.-X. Zhu, and X.-M. Chen, Chemical Communications **48**, 11395 (2012).

[11] D. Fairen-Jimenez, R. Galvelis, A. Torrisi, A. D. Gellan, M. T. Wharmby, P. A. Wright, C. Mellot-Draznieks, and T. Duren, Dalton Transactions **41**, 10752 (2012).

[12] K. Zhang, L. Zhang, and J. Jiang, The Journal of Physical Chemistry C **117**, 25628 (2013).

[13] J. F. Nye, *Physical properties of crystals* (Oxford University press, 1985).

[14] G. Lu and J. T. Hupp, Journal of the American Chemical Society **132**, 7832 (2010).

[15] R. S. J. Bak, High pressure research **11**, 329 (1994).

[16] L. M. Markham, L. C. Mayne, B. S. Hudson, and M. Z. Zgierski, The Journal of Physical Chemistry **97**, 10319 (1993).

[17] R. L. Sobocinski, M. A. Bryant, and J. E. Pemberton, Journal of the American Chemical Society **112**, 6177 (1990).

[18] Y. Yu, Y. Wang, K. Lin, N. Hu, X. Zhou, and S. Liu, The Journal of Physical Chemistry A **117**, 4377 (2013).

[19] H. Wu, W. Zhou, and T. Yildirim, The Journal of Physical Chemistry C **113**, 3029 (2009).

[20] J. Pérez-Pellitero *et al.*, Chemistry – A European Journal **16**, 1560 (2010).

[21] J. L. C. Rowsell, E. C. Spencer, J. Eckert, J. A. K. Howard, and O. M. Yaghi, Science **309**, 1350 (2005).

[22] H. Wu, W. Zhou, and T. Yildirim, Journal of the American Chemical Society **129**, 5314 (2007).

[23] R. Krishna, Chemical Society Reviews **41**, 3099 (2012).

# Chapter 5

# Second sound in double walled carbon nanotubes

Dhanya Radhakrishnan**,** Chandrabhas Narayana and Ajay K Sood**,** *"Second sound in carbon nanotubes"* (manuscript prepared)

## 5.1. Introduction

Phonons play a major role in heat propagation in solids. Heat transfer in a phonon gas can be due to ballistic phonons, second sound and thermal diffusion depending on the normal and resistive phonon relaxation times [1]. Second sound is a wavelike propagation of entropy or temperature which occurs generally in the vicinity of thermal conductivity maxima within a narrow temperature regime at low temperatures, and its velocity shows a large temperature dependence [2-8]. Second sound can be observed only when the normal (momentum conserving) phonon-phonon collisions are more frequent than the resistive (momentum destroying) collisions. This "window condition" requires very pure samples [1] and the energy carried by the second sound increases with the purity of the sample [9,10]. Due to these requirements, second sound has been observed only in limited systems such as super-fluid helium, solid helium, NaF, Bi and $SrTiO_3$. Heat pulse experiments have been employed to study the second sound. In addition, it has been shown that narrow central peak (NCP) in the Brillouin spectrum evolves into two peaks around zero energy transfer at low temperatures which are associated with Stokes and anti-Stokes bands due to second sound [11,12]. These side bands due to second sound ride above the broad central peak (BCP) [3]. The linewidth of the BCP narrows while NCP broadens as temperature is reduced, eventually becoming indistinguishable in ballistic regime [11,13].

Carbon nanotubes (CNTs), since their discovery have received tremendous attention due to their high thermal conductivity [14] with applications in heat dissipation in electronic and micromechanical devices, thermal interface materials, thermal rectification *etc.* [15] The measured thermal conductivity of individual multi walled nanotubes (MWNT) is estimated to be over 3000 W/m-K at room temperature [16] which is higher than that of diamond and graphite [17-19]. In comparison, a mat of unaligned MWNTs has much lower thermal conductivity (~ 20 W/m-K) owing to the thermal resistance at tube-tube junctions [20]. Though, the measured value of thermal conductivity of CNTs depends on the sample quality, whether aligned or unaligned and isolated or network, CNTs (both SWNT and MWNT) exhibit similar temperature behaviour with a conductivity maximum near room temperature [15,16,21,22].

Owing to their thermal conductivity maxima near room temperature and weak Umklapp phonon processes [23], CNTs are good candidate to look for the second sound at higher

temperatures. Molecular dynamics simulations have predicted that second sound carries largest amount of energy during heat transport in zig-zag CNTs, leading to a high thermal conductivity [24]. Using temperature dependent Brillouin spectroscopy, we report here for the first time, observation of second sound in double walled carbon nanotubes (DWNT). In addition to the second sound, we observe both the narrow and broad central component in DWNT and have studied their temperature evolution.

## 5.2. Experimental details

DWNT, synthesised by chemical vapour deposition (CVD) was obtained as a thick film deposited on a parafilm. The nanotubes were separated from the parafilm by vigorously shaking the nanotube coated parafilm in chloroform. Once nanotubes are separated from the parafilm, it was washed with chloroform several times and was taken on a Si chip for Brillouin measurements. DWNTs thus obtained are found to be in bundles of ~ 20 nm diameter (5-15 tubes) and few microns long. Individual tubes were ~ 2.2 nm in diameter as deduced from Raman and TEM.

Brillouin spectra were recorded in back scattering geometry using 532 nm p-polarized excitation from a single-mode diode pumped Nd-YAG laser with power ~ 6 mW focussed on a spot size of ~ 5 μm. Scattered light was analyzed using a Sandercock-type 3+3 pass tandem Fabry–Perot interferometer, with a finesse of ~ 100 and equipped with a photo avalanche diode (Perkin Elmer, Canada) as the detector (Chapter 2). A free spectral range of 150 GHz and accumulation time of ~ 1 hr was used for the measurement at ambient conditions. Temperature measurements were done on DWNT using a Linkam stage (THMS 600) from 400-77 K with a temperature stability of 0.1 K. Different free spectral ranges were used for the temperature dependent Brillouin measurements of doublet (150 GHz and 333 GHz), BCP (333 GHz) and NCP (50 GHz). Though temperature dependence of BCP and second sound can be studied simultaneously using a free spectral range of 333 GHz, the second sound doublets were not resolvable above 323 K as the peaks were very close to the central Rayleigh peak and was dominated by BCP. So, above 323 K a lower spectral range (150 GHz) was employed to observe the second sound. Raman spectroscopy measurements were performed using 532 nm laser excitation with the experimental setup described in Chapter 2. Raman spectroscopy was used to characterise the CNTs and to study the temperature dependence of DWNTs.

## 5.3. Results and discussion

Figure 5.1 shows the Brillouin spectrum of DWNT at room temperature. The spectrum consists of a broad doublet which rides on a very broad and intense background. The scattered light was collected at different incidence angle, θ and azimuthal angle, ϕ (scattering geometry is shown in the inset of Fig. 5.1). The spectra were fitted using Lorentzian function with an appropriate background. Keeping θ constant and varying ϕ, the peak position and intensity is unchanged, indicating the in-plane isotropy of the sample arising from the randomly oriented carbon nanotubes (Fig. 5.2(a)). However, the frequency increases linearly (Figs. 5.2(b, c)) with respect to the parallel component of the wavevector $q_{||}$, which is tuned by varying θ. $q_{||} = 2k_i Sin\theta$ where $k_i = 2\pi/\lambda$, $\lambda$ is the wavelength of laser. This indicates that the phonons are propagating along the surface of the CNT as observed in some opaque materials and the sound velocity ($V = 2\pi\nu/q_{||}$) thus determined is 15.3 ± 0.4 km/s [25]. This value differs from the theoretically predicted value of longitudinal acoustic mode, LA for individual nanotubes which ranges from 17-24 km/s [26-28]. Also, there is very less probability that the observed peaks are the transverse acoustic mode (TA), as TA modes do not appear very often in the back scattering geometry [29].

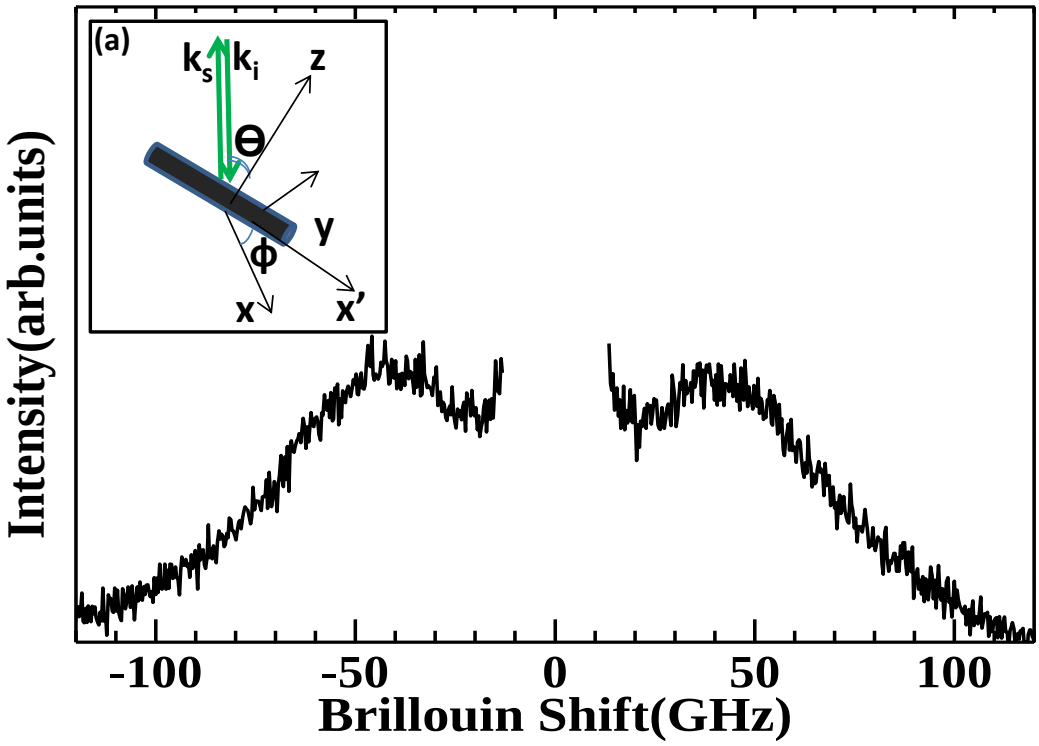


Fig. 5.1. Brillouin spectrum of DWNT at room temperature at θ = 40°. The inset shows the scattering geometry with respect to a nanotube.

The Brillouin peak we obtained is similar to the one obtained for unaligned SWNT by Bottani *et al.*, [30] except that our study shows θ dependence. Though dependence on θ was necessary for assigning the Brillouin peak as propagating LA mode in CNT, [30] we attribute these resonant features sitting on a broad background as second sound due to their anomalous temperature dependence (which will be discussed soon) and is predicted to have a velocity of 12.2 km/s in SWNT [24].

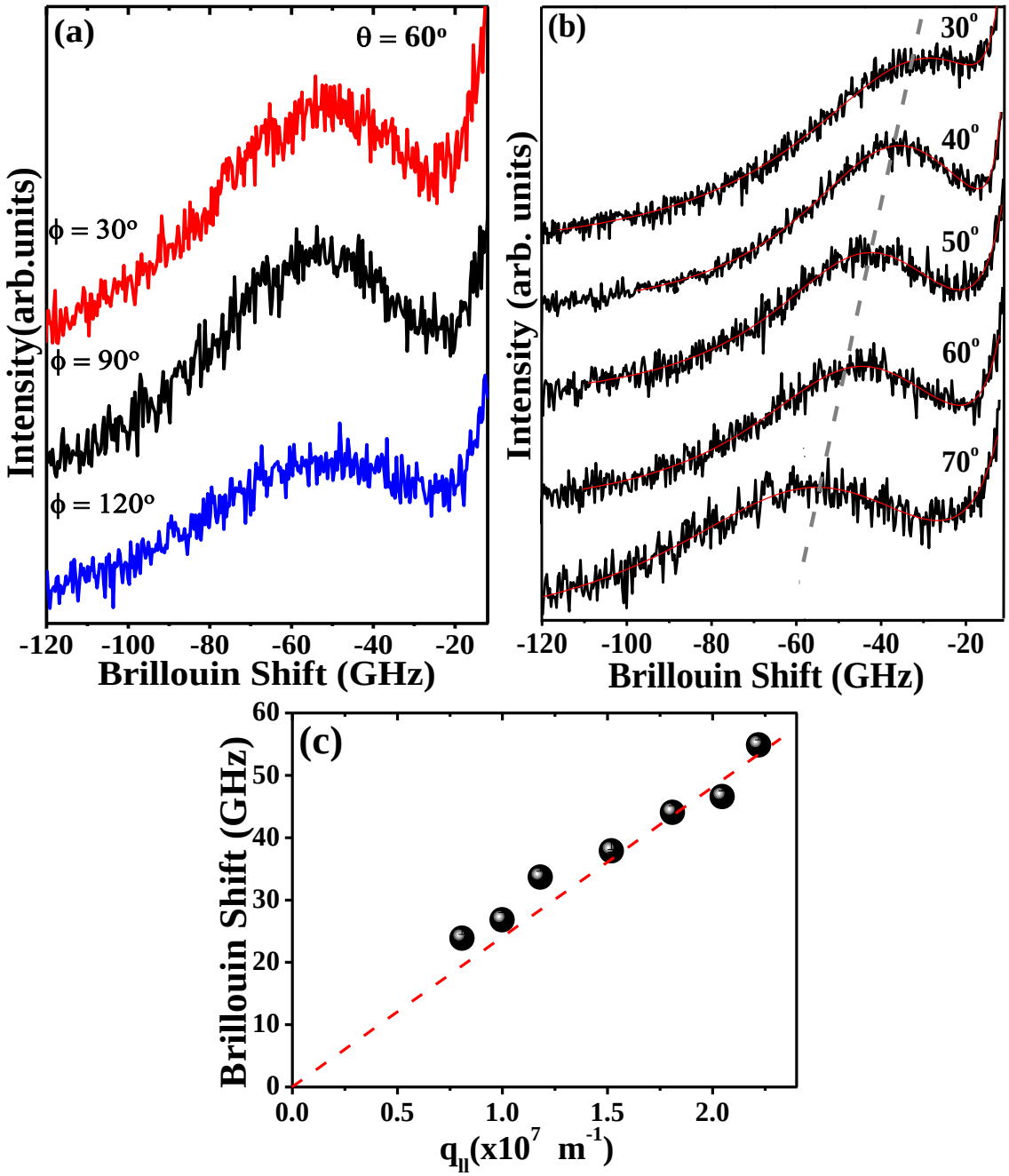


Fig. 5.2. Brillouin spectra of DWNT as (a) φ and (b) θ are varied. (c) Brillouin shift with respect to the parallel component of wavevector for DWNT (red dashed line is guide to the eye).

Ideally we should observe LA and TA modes in the Brillouin spectra, while the second sound and central peaks will be encountered rarely. The LA mode in CNT would have appeared around 60 GHz assuming a Young's modulus of 1 TPa and θ dependence [30-32]. But, we could not observe LA in our spectra as it could be hidden under the intense second sound, or it could be too weak to be detected as in graphene [33]. Also, though we tried obtaining Brillouin spectra from various CNT samples, only samples having very low defect gave the Brillouin signal. The Raman spectra of the CNTs studied is shown in Fig. 5.3 and we had obtained the Brillouin spectrum only when the defect band 'D band' which appears at ~ 1340 $cm^{-1}$ is very low in intensity. In general, $I_D/I_G$ ratio in CNT is used for estimating the quality of the sample [34,35]. Apart from the DWNT, we had obtained Brillouin spectra only from SWNT (diameter ~ 1.2 nm, obtained from Carbon Solutions Inc, California) and MWNT, (diameter ~ 10 nm, obtained from Shenzhen Nanotech Port Co Ltd) Raman spectra for which is the first and third curve (from bottom) in Fig. 5.3.

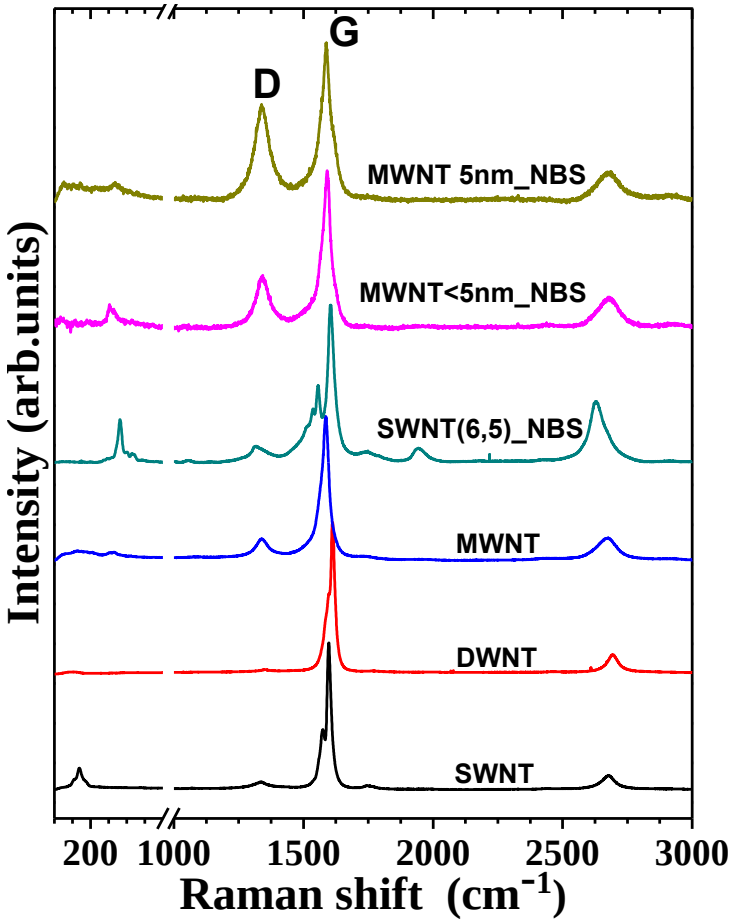


Fig. 5.3. Raman spectra of few nanotubes that were studied. The first three samples (from top) did not give any Brillouin spectrum and is denoted by CNT_NBS (NBS-No Brillouin signal). Brillouin spectra were obtained only from the last three samples (SWNT, DWNT and MWNT).

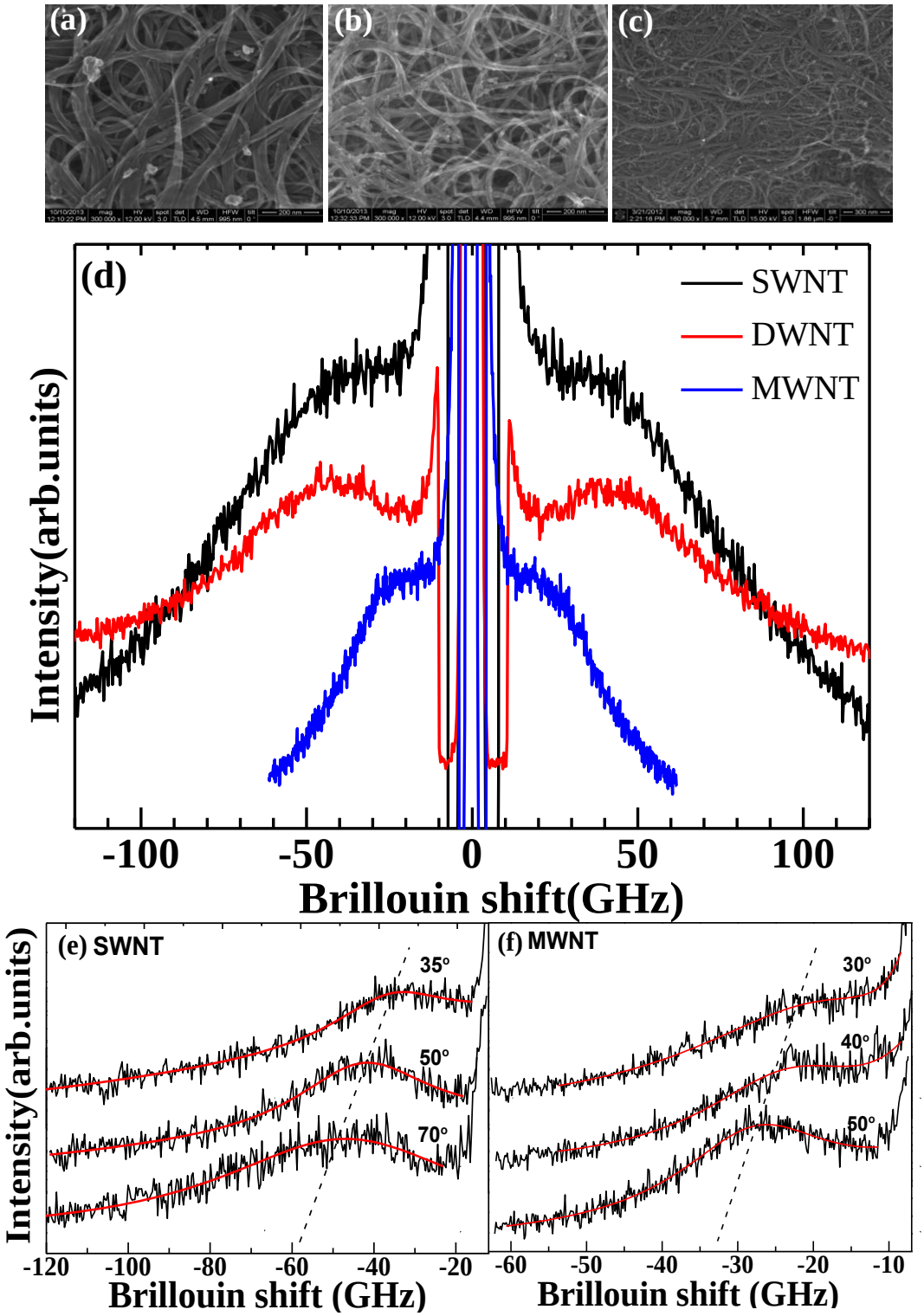


Fig. 5.4. The FESEM images of (a) SWNT (b) DWNT and (c) MWNT. (d) Brillouin spectra of SWNT, DWNT and MWNT and room temperature at θ = 50º. The evolution of the Brillouin spectra as θ is varied for (e) SWNT and (f) MWNT.

The Brillouin spectra obtained from SWNT, DWNT and MWNT are shown in Fig. 5.4(d). The theta dependence observed in the case of SWNT and MWNT is shown in Fig.

5.4 (e, f). As observed for the case of DWNT, the Brillouin shift of SWNT and MWNT also increases as θ is increased. It is observed that as the $I_D/I_G$ ratio of the nanotubes increases, the intensity of the Brillouin signal reduces, as seen in MWNT which necessitates a longer accumulation time. For CNTs having very high $I_D/I_G$ ratio, Brillouin signals were absent. The intensity of the Brillouin signal was also independent of other impurities (for example, fullerenes, nano carbons) in the sample, as all the samples show similar impurity content as evidenced from the field emission scanning electron microscopy (FESEM) images (Fig. 5.4(a-c)). Due to the low signal intensity of SWNT and MWNT, we could not follow their temperature dependence as the signal became very weak at low temperatures.

The possibility that the Brillouin peaks observed are diffusive acoustic modes (which is a consequence of nanotube length being comparable to the wavelength of light) can be neglected based on the following arguments: a) we observe a θ dependence in the Brillouin shift. If the Brillouin peaks are due to the confined acoustic modes, θ dependence will not be observed as shown by Bottani *et al* [30]. b) Brillouin spectrum is not observed when impurities in the nanotube are high. If the observed mode is a diffusive acoustic mode, regardless of the defects the Brillouin peaks should have been present.

We now follow the temperature dependence of the Brillouin spectral features for the DWNT. Figure 5.5(a, b) shows the temperature dependence of Brillouin shift and full width at half maximum (FWHM) for the broad doublets of DWNT measured at $\theta = 48^o$. The peaks were fitted using three Lorentzian functions: two for the doublets (represented by squares in Fig. 5.5) and one for the broad central component. At high temperatures the Brillouin doublets were very broad and around 303 K, peaks became prominent as their intensity increased on decreasing the temperature. As the temperature is decreased, the Brillouin shift increases and FWHM decreases showing saturation below 150 K. What is truly remarkable is the large change in frequency shift (~ 71%) and the FWHM (by ~ 66%).

Such anomalous change has never been observed so far for an acoustic mode. For example carbon allotropes, graphite [36] and diamond [37,38] exhibit a change of only ~ 3% in their frequency shift of acoustic modes in similar temperature range. Also the temperature dependence of Young's modulus of CNTs is shown theoretically to change

only by 3%, corresponding to a frequency change of ~ 1.5% in this temperature range [39-41]. This temperature behaviour cannot be attributed to the anharmonic behaviour of acoustic modes since acoustic modes show normal lattice anharmonicity only at very low temperatures (< 10 K) [15]. Phase transition can also give rise to such behaviour in the acoustic modes. Figure 5.6(a) shows the ambient temperature Raman spectrum of DWNT with the insets showing the deconvoluted radial breathing mode (RBM) and the graphitic bands (G band – deconvoluted into four peaks and represented by G1 - G4). Figure 5.6(b-g) shows the temperature dependence of the RBM and G bands which exhibit only the anharmonic behaviour demonstrating that, no phase transitions are involved in the temperature regime investigated.

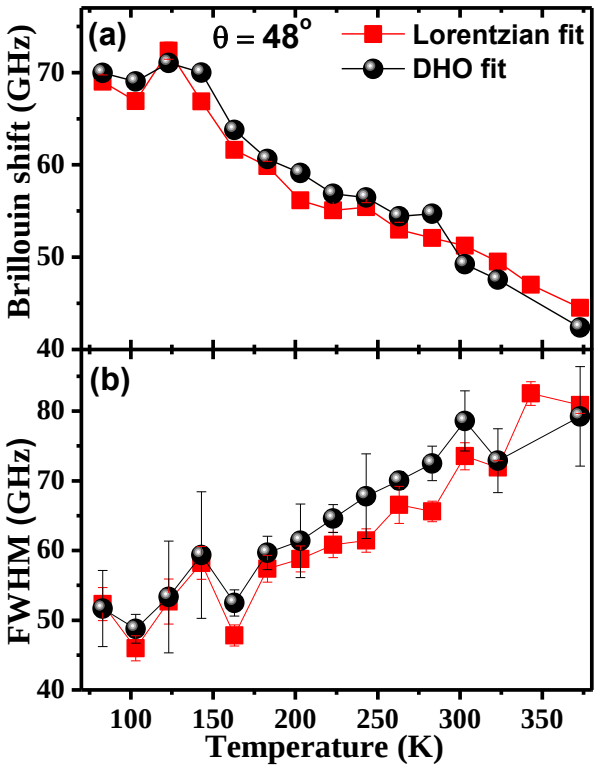


Fig. 5.5. Temperature dependence of (a) shift and (b) FWHM of the Brillouin doublet of DWNT at $\theta = 48^0$. The squares and circles are the values determined from the Lorentzian fit and damped harmonic oscillator fit, (DHO fit using Eq. 5.1) respectively.

We have also observed narrow c**o**mponent of central peak and broad component of central peak at all temperatures. The temperature dependence of the NCP is shown in Fig. 5.7(a, c). The spectra were fitted with a single lorentzian function after removing the Rayleigh component. The FWHM of this component is seen to be increasing as temperature is reduced, though the change is very small. In collision dominated regime,

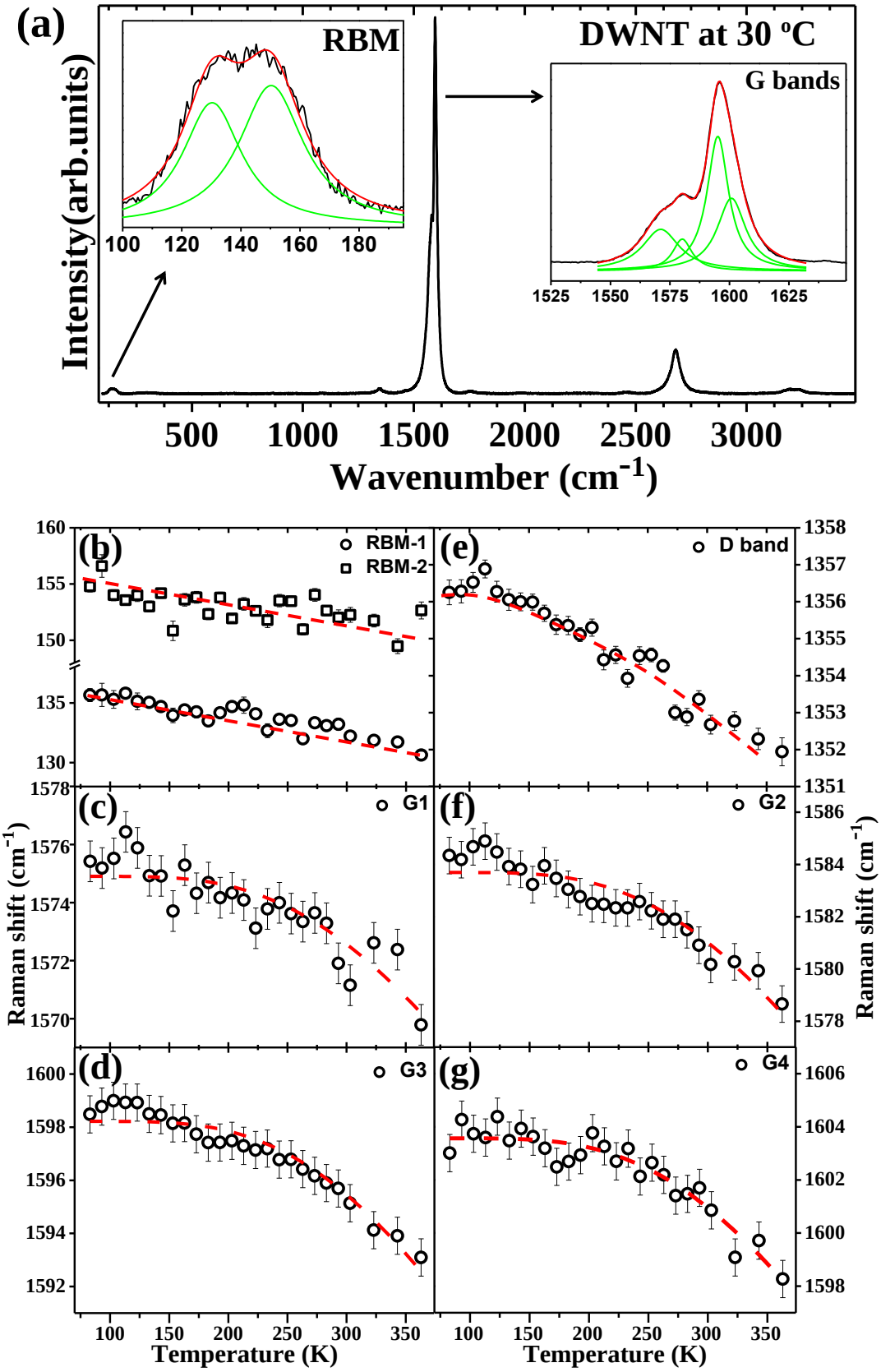


Fig. 5.6(a) The Raman spectrum of DWNT at room temperature. The inset shows the deconvolution of radial breathing mode (RBM) and G bands. (b-g) The temperature dependence of RBM and G bands in DWNT. The red lines are fits for cubic anharmonicity.

linewidth (half width at half maxima) of NCP will be equal to $D_{th}q^2$ where $D_{th}$ is the thermal diffusivity and $q$ is the wave vector transfer (Chapter 1) [11,42]. $q = 2\frac{2\pi}{\lambda} n\sin(\beta / 2)$, where n ~ 1.75 is the refractive index [43,44] and β is the angle between the incident and scattered light which is 180° in our case. Thermal conductivity, $\kappa$ can be estimated from $D_{th}$ using the relation $D_{th} = \frac{\kappa}{C\rho}$ where, $C$ is specific heat and $\rho$ is the density (2260 kg/m$^3$). The thermal conductivity thus obtained from NCP at 300 K is ~ 190 W/m-K (C = 650 J/kg K for SWNT) [45]. This value is very close to the thermal conductivity exhibited by an aligned SWNT mat (~ 217 W/m-K) and also exhibit similar temperature dependence (Fig. 5.8(a)) [46].

The temperature dependence of BCP can be studied by fitting the second sound and BCP simultaneously using the equation given below

$$S_D = A\frac{2\omega_0{}^2\Gamma_{ss}}{(\omega^2 - \omega_0{}^2)^2 + 4\omega^2\Gamma_{ss}{}^2} + B\frac{\Gamma_2}{\omega^2 + \Gamma_2^2} \quad (5.1)$$

The first term here represents the damped harmonic oscillator (DHO) of thermal phonons where, $\omega_0$ is the natural frequency of phonon gas and $\Gamma_{SS}$ is the linewidth of the second sound [12,47]. $\Gamma_{ss} = \frac{2}{5}\omega_0{}^2\tau_N + \frac{1}{2\tau_R}$, where $\tau_N$ and $\tau_R$ are the relaxation time for normal and resistive phonon collisions as explained in Chapter 1. The frequency of the second sound can be determined from the formula $\omega_{SS} = \sqrt{\omega_0^2 - 2\Gamma_{ss}^2}$. The second term in Eq. 5.1 is a Lorentzian function with a linewidth $\Gamma_2$ and is used for fitting the BCP. The parameters $\omega_0$, $\Gamma_{ss}$, A, B and $\Gamma_2$ were adjusted for fitting the spectrum.

The peak position and FWHM of the second sound derived using Eq. 5.1 is shown as circles in Fig. 5.5 and the values determined are in close agreement with the Lorentzian fit. Temperature dependence of BCP is shown in Fig. 5.7(b, d). BCP is very intense and narrow at high temperature and it broadens at low temperature, contradicting the behaviour in any material observed till now [42,48]. Koreeda *et al.* [47,49] has used a Lorentzian where the linewidth is 1/τ (τ is the averaged relaxation time over all thermal phonons) to fit the BCP which explains the decrease in linewidth as temperature is lowered (Chapter 1). The opposite trend in the temperature dependence observed here implies that linewidth of BCP should be also proportional to the relaxation time, similar to NCP. Moreover second sound emerges from the BCP contrary to the idea that it should emerge from NCP (Chapter 1). Assuming BCP as another narrow component whose

linewidth is equal to $D_{th}q^2$, we derived a thermal conductivity of ~ 3300 W/m-K at 300 K which is the conductivity exhibited by an individual CNT [16,23]. The temperature dependence of the thermal conductivity obtained from BCP is shown in Fig. 5.8(b) and this is in close agreement with the literature [16]. The relaxation time $\tau_R$ can be obtained from the relation, $\kappa = CV_D^2\tau$ where $V_D$ is the average sound velocity ($V_D$ ~ $10^4$ m/s). The relaxation time thus obtained is ~ $10^{-11}$ s. The values of $\tau_N$ can be then estimated using $\Gamma_{SS}$ and $\omega_0$ obtained from the DHO fit and $\tau_R$ from the BCP. Temperature dependence of the frequencies $\tau_R^{-1}$, $\tau_N^{-1}$ and $\omega_{ss}$ thus obtained is shown in Fig. 5.9(a).

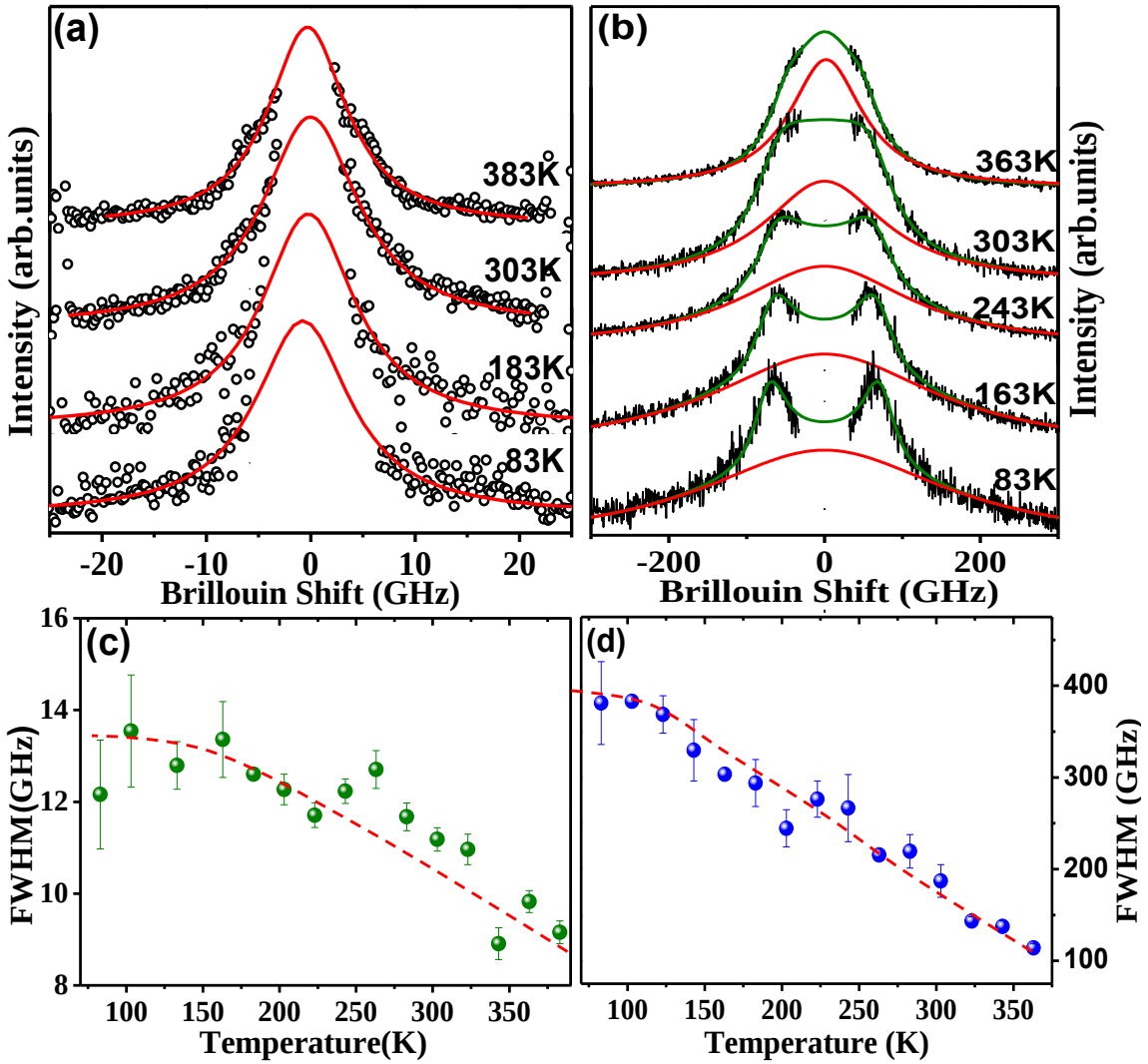


Fig. 5.7 (a) Temperature evolution of NCP and (b) BCP (shown by red solid lines). Temperature dependence of FWHM for (c) NCP and (d) BCP. The red dashed lines are guide to the eyes.

$\tau_R^{-1}$ increases as temperature is increased and it becomes larger than $\omega_{ss}$ beyond ~ 310 K. $\tau_N^{-1}$ is almost constant below 310 K and increases steeply above this. Though $\tau_N$ is

susceptible to large error due to its dependency on $\tau_R$, $\omega_0$ and $\Gamma_{SS}$, its value is higher than $\tau_R^{-1}$ and $\omega_{ss}$ at all the temperatures investigated. Below 310 K, second sound window begins to open up, satisfying the window condition $\tau_R^{-1} < \omega_{SS} < \tau_N^{-1}$ which is necessary for the propagation of second sound. In fact, the window remains open throughout the region from 310 K to 77 K rendering the fact that the broad doublet observed here is indeed the propagating second sound. To our knowledge, second sound has never been observed at room temperature and also over such a large temperature range. Above 310 K, umklapp phonon processes dominates [16] leading to the condition $\tau_R^{-1} > \omega_{SS}$ resulting in an over damped second sound.

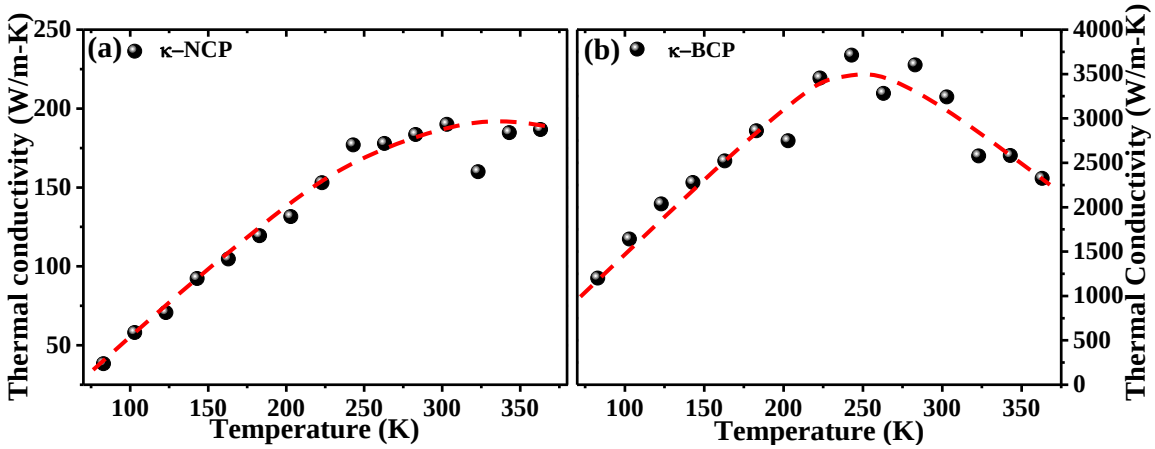


Fig. 5.8. Thermal conductivity verses temperature derived from (a) NCP and (b) BCP. The dashed red lines are guide to the eyes.

The second sound can be simulated using different values of $\tau_R$ and $\tau_N$ using the DHO part of Eq. 5.1. Using $\tau_N$ = 0 s, corresponding to the case of ideal second sound [1] and $\tau_R$ = $10^{-12}$ s (relaxation time from NCP) a doublet peak can never be achieved as this results in only a central lorentzian peak. A peak thus derived using the value of $\tau_R$ at RT (= 1.2 x $10^{-12}$ s) is shown in the inset of Fig. 5.9(b). The doublet feature of second sound can be obtained only if $\tau_R$ of the order of $10^{-11}$ s is used which demands the use of relaxation time derived from BCP. The spectra thus obtained for different temperatures using the values of $\tau_R$ obtained from the BCP and $\tau_N = 0\ s$ is shown in Fig. 5.9(b). The concurrent existence of NCP and BCP implies that there are two resistive phonon relaxation processes existing simultaneously within the CNT bundle. The slower resistive process corresponds to the relaxation time within an individual CNT [16,22] and the faster $\tau_R$ corresponds to the relaxation time in an aligned CNT. Former results in second

sound and BCP while the later give rise to NCP. Though our sample contains unaligned CNT bundles, using Brillouin spectroscopy, we could capture the relaxation time within a CNT bundle where individual CNTs will be aligned. The phonon Knudsen number (Chapter 1) defined as $\mathrm{Kn} = \omega_0 \tau$ can be estimated for the normal and resistive phonon processes and its values at different temperatures is given in Fig. 5.10 [47,50]. $\mathrm{Kn_R}$ ranges from ~ 1 to 2.2 as the temperature is reduced from 323 K – 83 K, while $\mathrm{Kn_N}$ is less than 0.25 throughout the temperature range investigated, thus validating the fact that the second sound regime extends from 310 K – 77 K.

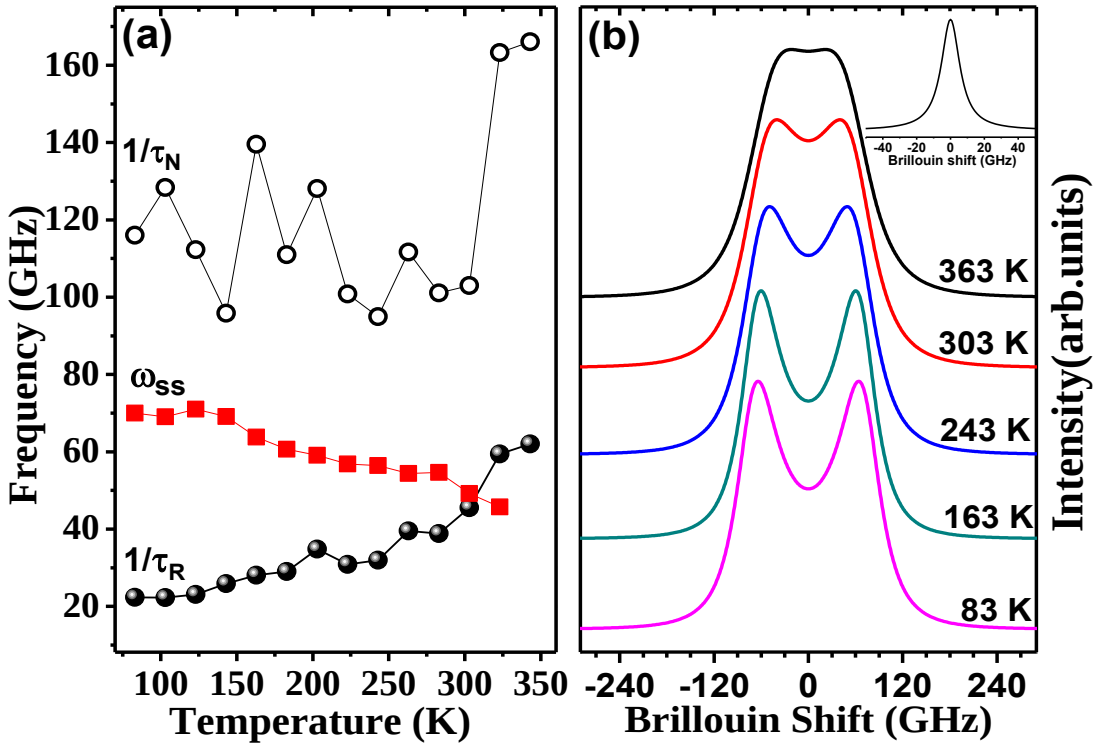


Fig. 5.9(a) Temperature dependence of $\omega_{SS}$, $1/\tau_N$ and $1/\tau_R$ obtained by fitting the Brillouin spectrum using Eq. 5.1. (b) The simulated second sound spectra at different temperatures when $\tau_R$ is ~$10^{-11}$ s (derived from BCP) and $\tau_N$ = 0 s. The inset shows the spectra obtained when $\tau_R$ = 1.2 x $10^{-12}$ s and $\tau_N$ = 0 s.

Presence of second sound over such a large temperature regime and at higher temperature is in accordance with the theoretical prediction by Lee *et al.* in suspended graphene [51]. Due to the low dimensionality of graphene, a strong normal phonon scattering will be observed even at room temperature compared to the 3D materials [51,52]. So observation of high normal phonon relaxation rate and second sound in carbon nanotubes could be a

consequence of the lower dimensionality of the system as it is known that Umklapp phonon scattering will be suppressed in one-dimensional materials [53,54].

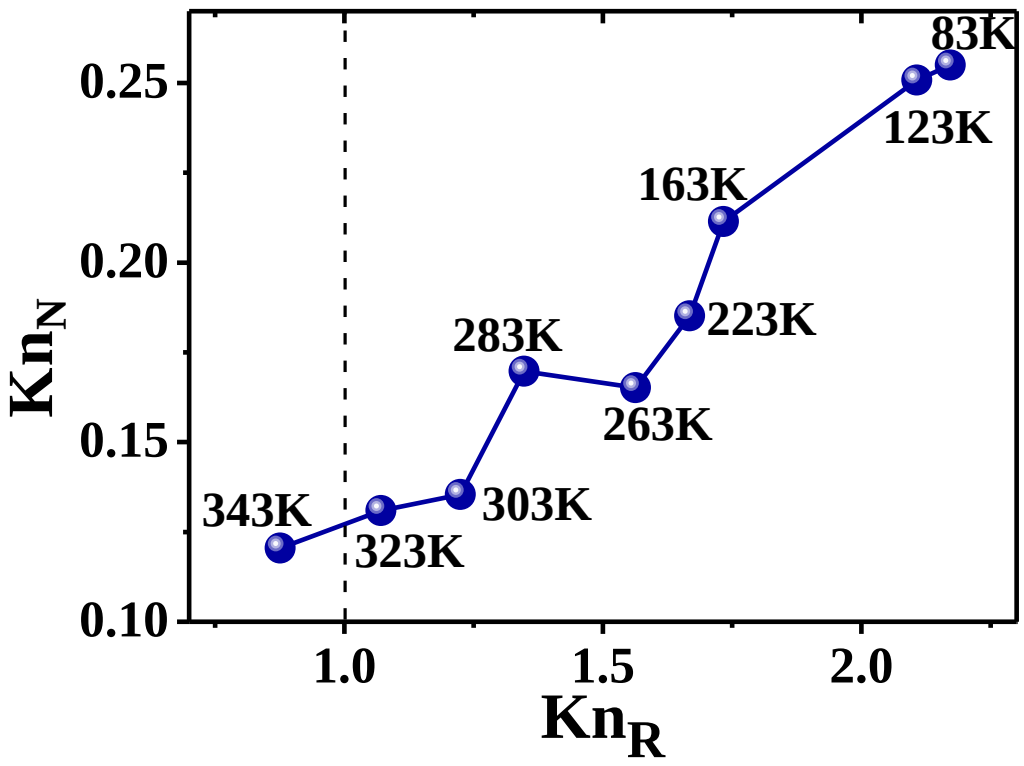


Fig. 5.10. The phonon Knudsen number at different temperatures.

## 5.4. Conclusions

In conclusion we have observed second sound in DWNT at room temperature. The second sound regime extends throughout the temperature range of 310 K - 77 K. The high thermal conductivity and its maxima around room temperature lead to frequent normal phonon collisions and rare resistive phonon collisions within CNT resulting in the occurrence of second sound. We also observe two central peaks, narrow and broad throughout the temperature regime investigated. The FWHM of both NCP and BCP increases as the temperature is reduced. This temperature dependence of BCP contradicts the behaviour in other materials which lead us to conclude that BCP arise from the thermal conductivity of individual CNT while NCP originate from the CNT bundle where individual tubes are aligned.

## 5.5. Bibliography

[1] W. Dreyer and H. Struchtrup, Continuum Mechanics and Thermodynamics **5**, 3 (1993).

[2] C. C. Ackerman, B. Bertman, H. A. Fairbank, and R. A. Guyer, Physical Review Letters **16**, 789 (1966).

[3] B. Hehlen, A.-L. Pérou, E. Courtens, and R. Vacher, Physical Review Letters **75**, 2416 (1995).

[4] H. E. Jackson, C. T. Walker, and T. F. McNelly, Physical Review Letters **25**, 26 (1970).

[5] V. Narayanamurti and R. C. Dynes, Physical Review Letters **28**, 1461 (1972).

[6] V. Narayanamurti and R. C. Dynes, Physical Review B **12**, 1731 (1975).

[7] V. Narayanamurti, R. C. Dynes, and K. Andres, Physical Review B **11**, 2500 (1975).

[8] E. W. Prohofsky and J. A. Krumhansl, Physical Review **133**, A1403 (1964).

[9] H. E. Jackson and C. T. Walker, Physical Review B **3**, 1428 (1971).

[10] T. F. McNelly, S. J. Rogers, D. J. Channin, R. J. Rollefson, W. M. Goubau, G. E. Schmidt, J. A. Krumhansl, and R. O. Pohl, Physical Review Letters **24**, 100 (1970).

[11] A. Koreeda, T. Nagano, S. Ohno, and S. Saikan, Physical Review B **73**, 024303 (2006).

[12] A. Koreeda, R. Takano, and S. Saikan, Physical Review Letters **99**, 265502 (2007).

[13] H. E. Jackson, R. T. Harley, S. M. Lindsay, and M. W. Anderson, Physical Review Letters **54**, 459 (1985).

[14] M. S. Dresselhaus, G. Dresselhaus, and A. Jorio, Annual Review of Materials Research **34**, 247 (2004).

[15] A. M. Marconnet, M. A. Panzer, and K. E. Goodson, Reviews of Modern Physics **85**, 1295 (2013).

[16] P. Kim, L. Shi, A. Majumdar, and P. L. McEuen, Physical Review Letters **87**, 215502 (2001).

[17] A. Alofi and G. P. Srivastava, Physical Review B **87**, 115421 (2013).

[18] A. De Combarieu, J. Phys. France **28**, 951 (1967).

[19] J. E. Graebner *et al.*, Diamond and Related Materials **7**, 1589 (1998).

[20] W. Yi, L. Lu, Z. Dian-lin, Z. W. Pan, and S. S. Xie, Physical Review B **59**, R9015 (1999).

[21] N. R. Pradhan, H. Duan, J. Liang, and G. S. Iannacchione, Nanotechnology **20**, 245705 (2009).

[22] J. Hone, M. Whitney, C. Piskoti, and A. Zettl, Physical Review B **59**, R2514 (1999).

[23] C. Yu, L. Shi, Z. Yao, D. Li, and A. Majumdar, Nano Letters **5**, 1842 (2005).

[24] M. A. Osman and D. Srivastava, Physical Review B **72**, 125413 (2005).

[25] R. T. Harley and P. A. Fleury, Journal of Physics C: Solid State Physics **12**, L863 (1979).

[26] J. Yu, R. K. Kalia, and P. Vashishta, The Journal of Chemical Physics **103**, 6697 (1995).

[27] D. Sánchez-Portal, E. Artacho, J. M. Soler, A. Rubio, and P. Ordejón, Physical Review B **59**, 12678 (1999).

[28] G. D. Mahan, Physical Review B **65**, 235402 (2002).

[29] J. R. Sandercock, *Light scattering in solids III* (Springer Berlin Heidelberg, Vol. 51, p. 173.

[30] C. E. Bottani, A. L. Bassi, M. G. Beghi, A. Podestà, P. Milani, A. Zakhidov, R. Baughman, D. A. Walters, and R. E. Smalley, Physical Review B **67**, 155407 (2003).

[31] M. M. J. Treacy, T. W. Ebbesen, and J. M. Gibson, Nature **381**, 678 (1996).

[32] A. Krishnan, E. Dujardin, T. W. Ebbesen, P. N. Yianilos, and M. M. J. Treacy, Physical Review B **58**, 14013 (1998).

[33] Z. K. Wang, H. S. Lim, S. C. Ng, B. Özyilmaz, and M. H. Kuok, Carbon **46**, 2133 (2008).

[34] R. A. DiLeo, B. J. Landi, and R. P. Raffaelle, Journal of Applied Physics **101** (2007).

[35] M. S. Dresselhaus, G. Dresselhaus, R. Saito, and A. Jorio, Physics Reports **409**, 47 (2005).

[36] W. B. Gauster and I. J. Fritz, Journal of Applied Physics **45**, 3309 (1974).

[37] G. Gao, K. V. Workum, J. D. Schall, and J. A. Harrison, Journal of Physics: Condensed Matter **18**, S1737 (2006).

[38] E. S. Zouboulis, M. Grimsditch, A. K. Ramdas, and S. Rodriguez, Physical Review B **57**, 2889 (1998).

[39] C.-L. Zhang and H.-S. Shen, Applied Physics Letters **89** (2006).

[40] N. R. Raravikar, P. Keblinski, A. M. Rao, M. S. Dresselhaus, L. S. Schadler, and P. M. Ajayan, Physical Review B **66**, 235424 (2002).

[41] H. Jin-Yuan, L. Jian-Ming, H. Min-Yi, and H. Chi-Chuan, Nanotechnology **17**, 3920 (2006).

[42] A. Koreeda, M. Yoshizawa, S. Saikan, and M. Grimsditch, Physical Review B **60**, 12730 (1999).

[43] T.-I. Jeon, K.-J. Kim, C. Kang, I. H. Maeng, J.-H. Son, K. H. An, J. Y. Lee, and Y. H. Lee, Journal of Applied Physics **95**, 5736 (2004).

[44] W. A. deHeer, W. S. Bacsa, A. Châtelain, T. Gerfin, R. Humphrey-Baker, L. Forro, and D. Ugarte, Science **268**, 845 (1995).

[45] J. Hone, M. C. Llaguno, M. J. Biercuk, A. T. Johnson, B. Batlogg, Z. Benes, and J. E. Fischer, Applied Physics A **74**, 339 (2002).

[46] J. Hone, M. C. Llaguno, N. M. Nemes, A. T. Johnson, J. E. Fischer, D. A. Walters, M. J. Casavant, J. Schmidt, and R. E. Smalley, Applied Physics Letters **77**, 666 (2000).

[47] A. Koreeda, R. Takano, and S. Saikan, Physical Review B **80**, 165104 (2009).

[48] A. Koreeda, T. Nagano, S. Ohno, and S. Saikan, Physical Review B **73**, 024303 (2006).

[49] A. Koreeda, R. Takano, and S. Saikan, Physical Review Letters **99**, 265502 (2007).

[50] A. Koreeda, R. Takano, and S. Saikan, Ferroelectrics **378**, 129 (2009).

[51] S. Lee, D. Broido, K. Esfarjani, and G. Chen, Nat. Commun. doi: 10.1038/ncomms7290 (2015).

[52] A. Cepellotti, G. Fugallo, L. Paulatto, M. Lazzeri, F. Mauri, and N. Marzari, Nat Commun **6** (2015).

[53] D. T. Morelli, J. Heremans, M. Sakamoto, and C. Uher, Physical Review Letters **57**, 869 (1986).

[54] J. Hone, *Carbon Nanotubes* (Springer Berlin Heidelberg, 2001), Vol. 80, p. 273.

# Chapter 6

# A Brillouin scattering investigation of solvent dynamics in pyrrolidinium based ionic liquids

*The author's main contribution in this chapter is to perform the temperature dependent Brillouin measurements on pyrrolidinium based ionic liquids and analyzing the data. The samples were synthesized by Dr. Supti Das, Solid State and Structural Chemistry Unit, Indian Institute of Science.*

Supti Das, Dhanya Radhakrishnan, Chandrabhas Narayana and Aninda J. Bhattacharyya, *"A Brillouin scattering investigation of solvent dynamics/Relaxations in Pyrrolidinium based Ionic Liquids"* (manuscript prepared)

## 6.1. Introduction

Ionic Liquids (ILs) are the generic term for a class of molten organic salts which are fluids at temperatures around 100 °C or below [1-5]. They comprise of an organic cation and an inorganic anion. ILs have stimulated much interest for a variety of chemical, physical and biological processes in past few decades due to their remarkable unique properties like negligible volatility, thermal & electrochemical stability, non flammability, varying viscosity, high ionic conductivity *etc.* The physicochemical properties of ILs can be tuned by varying the combinations of cations or anions. The diverse range of applications of ILs can be attributed to these properties of ILs. Recently, hydrophobic ILs [2] has received significant interest which are considered as green as well as safe electrolytes in electrochemical devices specially in solar cells, super capacitors, rechargeable battery *etc* [6-10].

During past decade, developing new ILs has grown as an important research field. ILs based on the N, N'- dialkyl imidazolium cation is one of the most highly studied classes, due to its immense applications in different fields of research [11-15]. Another important series of ionic liquids is based on N-alkyl-N-methylpyrrolidinium cation ($P_{1n}$, n = 1-4) and the bis(trifluoromethanesulfonyl) imide (TFSI) anion [3-5,16-18]. These two ions ($P_{1n}$ and TFSI) together make a hydrophobic ionic liquid with a relatively high ionic conductivity even in the solid state and exhibit wide electrochemical stability window. Also, pyrrolidinium based ILs are quite attractive in terms of applications in advance energy storage devices *e.g.* Li-Air battery [7,9,10] while other ILs failed in terms of stability. An interesting phenomenon regarding these series of ILs is that depending upon the length of the alkyl chains, they can form plastic crystal or liquid phases. Pristine *N*-alkyl-*N*-methylpyrrolidinium bis(trifluoromethylsulfonyl) imide with n = 1, 2 (*i.e.* $P_{11}$TFSI and $P_{12}$TFSI) are plastic crystals at ambient temperature and shows quite high conductivity and electrochemical stability in their solid phase. Whereas pure *N*-methyl-*N*-butylpyrrolidinium bis(trifluoromethylsulfonyl) imide (n = 4 *i.e.* $P_{14}$TFSI) is an interesting Room Temperature Ionic Liquid (RTIL) with good room temperature ionic conductivity ($\sigma \geq 1$ mS·cm$^{-1}$) and large stability window of 5.5 V (which is almost 2 V higher than its imidazolium counterpart) [3]. Adding metal salt (*e.g.*, LiTFSI) in $P_{1n}$TFSI makes a promising electrolyte for metal-air or other secondary battery applications. Moreover, these ILs undergo multiple phase transitions as the temperature is reduced. Detailed knowledge of these phase transitions and different relaxation processes are

essential since such properties are important for understanding the solvent dynamics in electrolytes. In recent years, lot of focus has been made on the interpretation of the transport properties of various ILs [3,6,13,19]. The dynamics and relaxations of RTILs have also gained much attention and is probed using dielectric relaxation spectroscopy, [13] NMR relaxation, quasielastic neutron scattering, [20] terahertz spectroscopy, [21] Kerr effect spectroscopy, [22] infrared spectroscopy, [23] Raman spectroscopy [24,25] *etc*. But thorough study on the dynamics/relaxation processes of ILs using Brillouin scattering is negligible.

In our study, we choose to investigate the ILs composed of alkyl-methylpyrrolidinium bis(trifluoromethanesulfonyl) imide ($P_{1n}$TFSI, n = 1, 2 and 4; Fig. 6.1). As mentioned before, these series of ILs can be used in electrochemical as well as other applications and are often studied by means of various experimental and theoretical methods. We analyze the phase transitions with respect to temperature changes in these ionic compounds using the tool of Brillouin spectroscopy. In particular, insight into the dynamics of these can be gained by studying the changes in the Brillouin shift and full width at half maximum (FWHM) of the acoustic modes using temperature dependent Brillouin Scattering.

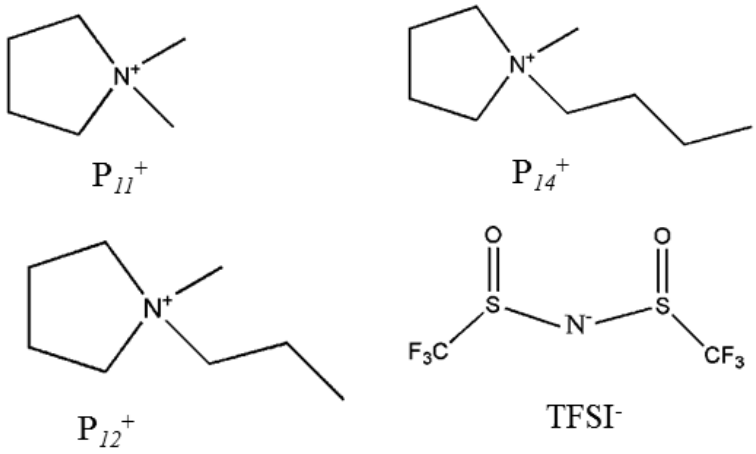


Fig. 6.1. Chemical structure of N-alkyl-N-methylpyrrolidinium bis(trifluoromethanesulfonyl) imide ($P_{1n}$TFSI, n = 1, 2, 4) ionic liquids.

## 6.2. Experimental details

N-methyl-N-butylpyrrolidinium bis(trifluorosulfonyl) imide ($P_{14}$TFSI, purity 98.5 % Sigma Aldrich (fluka)) was used as received from the suppliers. N,N-dimethylpyrrolidinium bis(trifluoromethanesulfonyl) imide ($P_{11}$TFSI) and N-methyl-N-

ethylpyrrolidinium bis(trifluoromethanesulfonyl) imide ($P_{12}$TFSI) was synthesized according to the work reported elsewhere in literature [3].

Brillouin spectra of the samples were carried out in back scattering geometry, as explained in Chapter 2 with a laser power of ~ 10 mW. A 10X objective lens was used for focusing the light. A mirror spacing of 6 mm (FSR = 25 GHz) was used to measure the LA and TA modes in $P_{14}$TFSI while both 6 mm and 12 mm (FSR = 12.5 GHz) was used for measuring all the possible modes in $P_{11}$TFSI and $P_{12}$TFSI. 12 mm mirror spacing was used since the TA modes occur at very low frequencies for $P_{11}$TFSI and $P_{12}$TFSI. Temperature dependent measurements were carried out using a liquid nitrogen cooled cryostage (Linkam stage, THMS 600) with a heating rate of 10 ºC/min and in nitrogen atmosphere. All samples were inserted inside capillary tube with their ends sealed. Suitable heat transmitting grease (H-grease or N-grease, Apiezon) was used to stick the capillary tube to the heating stage.

## 6.3. Results and Discussions

The pyrrolidinium ILs studied here exhibits series of phase transitions before finally melting. Figure 6.2 shows the differential scanning calorimetry (DSC) data of these ILs and the major phase transitions observed are given in Table 6.1 [3]. It can be observed that the melting temperatures of these ILs decreases on increasing the alkyl chain length with $P_{14}$TFSI exhibiting the lowest melting point and is liquid at room temperature (RTIL). $P_{12}$TFSI and $P_{14}$TFSI exhibits glass transition at low temperature and is followed by a series of solid-solid phase transitions on heating. Multiple solid-solid phase transitions indicate the existence of plastic crystal phases with $P_{11}$TFSI and $P_{12}$TFSI being plastic crystals at room temperature. In plastic crystal phases (also known as rotar phases or orientationally disordered phases) the center of mass of the molecules forms a regular crystalline lattice but the molecules are disordered with respect to their orientational degrees of freedom. Plastic crystal can be considered as an intermediate state between a true crystal and true liquid phase. The highest temperature crystalline phase is characterized by a strong rotational disorder of the whole molecular unit or a fragment and one or more phases of higher order exist below this which becomes stable at lower temperatures [26]. The plastic crystal state may contain many lattice vacancies due to which the material exhibit plasticity (mechanically soft), high self-diffusion coefficients *etc.* and may often results in a high conductivity.

$P_{11}$TFSI exist in solid plastic crystal phase (SPC) from 20 ºC till melting. Below 20 ºC, it transforms into a solid crystalline phase. $P_{12}$TFSI undergoes SPC to SPC transition at 18 ºC and 45 ºC and SPC to solid phase at -87 ºC which is immediately accompanied by a glass transition at -90 ºC. The onset of the rotational motions responsible for the plastic crystal behavior in $P_{12}$TFSI starts at the glass transition. $P_{14}$TFSI exhibit plasticity from -45 ºC to -18 ºC (till melting). Between -45 ºC and glass transition, it exists in a supercooled liquid (SCL) state where both translational and rotational degrees of freedom are present. On cooling, the SCL forms 'structural glass' which exhibit both translational and rotational disorder [26]. Whereas, $P_{12}$TFSI which is a plastic crystal before the glass transition forms a 'glassy crystal' (which is orientationally disordered and translationally ordered) on cooling [26].

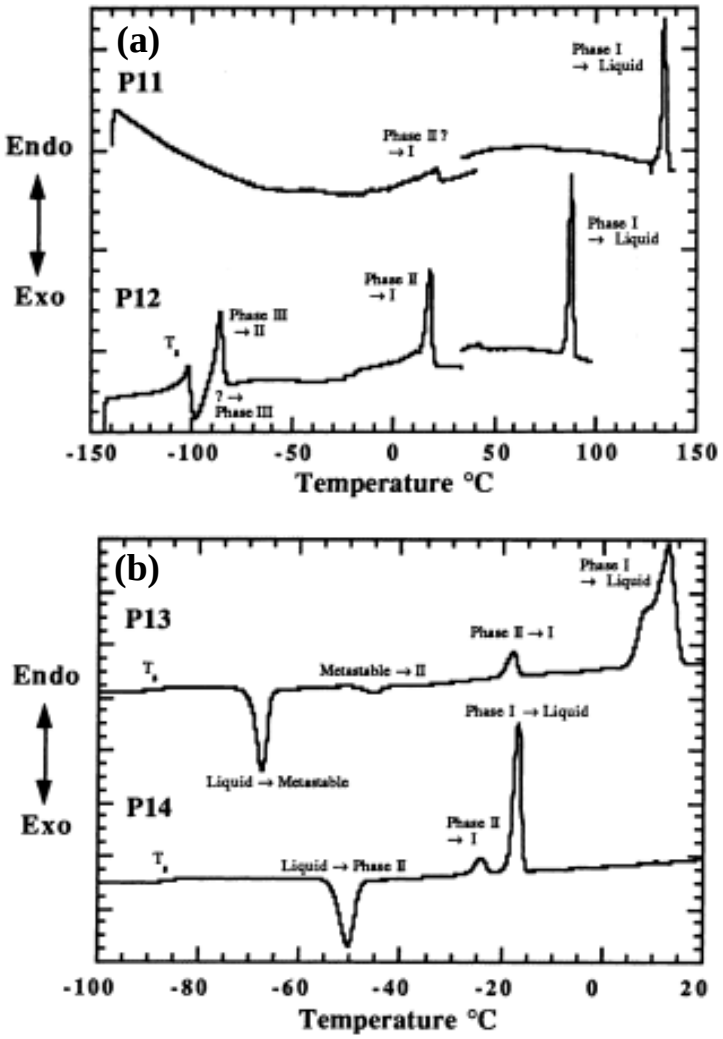


Fig. 6.2. Differential scanning calorimetry (DSC) thermograms of (a) $P_{11}$TFSI and $P_{12}$TFSI and (b) $P_{14}$TFSI. (Adopted from Ref [3])

Table. 6.1. The properties of Pyrrolidinium salts from DSC measurements (obtained from Ref [3]).

| Compound | Acronym | $T_g$ ($^oC$) | $T_{S-S}$ ($^oC$) | $T_M$ ($^oC$) |
|---|---|---|---|---|
| N, N-dimethylpyrrolidinium TFSI | $P_{11}$TFSI | | 20 | 132 |
| | | | 81 | |
| N- methyl-N-ethylpyrrolidinium TFSI | $P_{12}$TFSI | -90 | -87 | 86 |
| | | | 18 | |
| | | | 45 | |
| N- methyl-N-butylpyrrolidinium TFSI | $P_{14}$TFSI | -87 | -24 | -18 |

$T_g$-Glass transition, $T_{S-S}$- solid solid phase transition, $T_M$-melting temperature

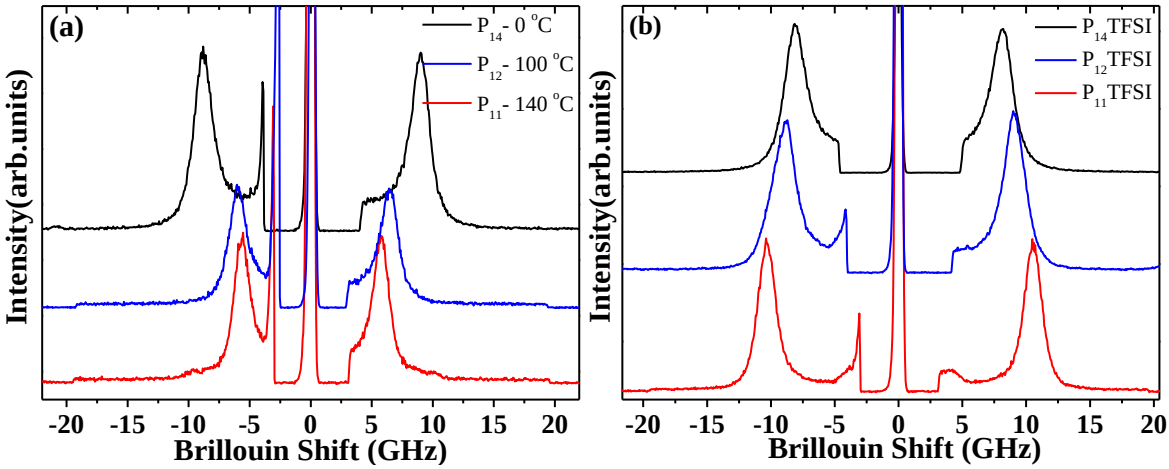


Fig. 6.3. Brillouin spectra of N-alkyl-N-methylpyrrolidinium bis(trifluorosulfonyl) imide ($P_{1n}$TFSI, n = 1, 2 and 4) based ILs in their (a) liquid phase and at (b) 25 ºC.

Figure 6.3(a) shows the Brillouin spectra of these ILs in their liquid phases. The spectra display one well resolved Brillouin peak, shift of which increases from 6 GHz to 9 GHz as the alkyl chain length is increased. This peak is the longitudinal acoustic peak (LA) and the high LA shift exhibited by $P_{14}$TFSI indicates a higher acoustic velocity corresponding to the bulkier $P_{14}^+$ entities. It is well known the higher acoustic velocity signifies a more rigid system. The full width at half maximum (FWHM) is also seen to increase as the chain length is increased. At room temperature (25 °C) the Brillouin shift

of the LA modes of these ILs decreases on increasing the length of the alkyl chain as shown in Fig. 6.3(b). The low Brillouin shift exhibited by $P_{12}$TFSI when compared to $P_{11}$TFSI indicates the high plasticity exhibited by the former. Generally, propagation of sound in plastic crystal is slower compared to the crystalline systems.

The temperature dependent measurements were conducted by covering a wide range of temperatures from melting to crystalline phase including plastic crystalline phase in all the cases. In the absence of any phase transition (when only anharmonic contributions are present), a decrease in the temperature will result in an increase in the Brillouin shift and a decrease in the FWHM. Any deviation from this behavior can be due to the phase transitions and other phenomena's occurring in the system.

Brillouin spectra for pristine $P_{1n}$TFSI (n = 1, 2 and 4) at various temperatures spanning from melting to crystalline transition including the major transitions are exhibited in Fig. 6.4 (we have neglected the weak phase transitions observed in DSC). The LA mode in solid phase is represented by LA-S (S signifies solid phase), and in liquid phase it is represented by LA-L (L signifies liquid phase). Significant changes in peak position are observed across the thermal phase transitions in all the three ILs. In solid phase, all the three ILs exhibits a LA mode and one or two TA modes. For example, the LA mode of $P_{11}$TFSI occurs at ~ 10.5 GHz which is represented by LA-S and the transverse acoustic modes (TA, Fig. 6.5) appear at ~ 3.6 (TA1) and 4.4 GHz (TA2) at 25 ºC. Appearance of TA mode is quite obvious in the solid crystalline state. The Brillouin shift displays changes in the slope near the solid-solid transitions whereas a sudden decrease in the shift as well as the disappearance of the TA modes can be observed when the sample undergoes melting. The presence of solid-solid transitions below melting signifies the presence of more liquid like rotar plastic phase.

As mentioned previously, $P_{12}$TFSI ionic liquid is very interesting as it is known to be an ionic liquid which forms a highly conducting plastic crystal phase at ambient temperature. At 25 ºC, the Brillouin spectra of $P_{12}$TFSI (Fig. 6.4(c)) displays one broad longitudinal mode around 10 GHz which consist of two well resolved Brillouin peaks at 9.5 and 10.4 GHz which are represented by LA-S1 and LA-S2, respectively. Presence of multiple LA modes at room temperature indicates the co-existence of two phases implying that the system is more disordered when compared to $P_{11}$TFSI as well as the transition at 18 ºC is sluggish.

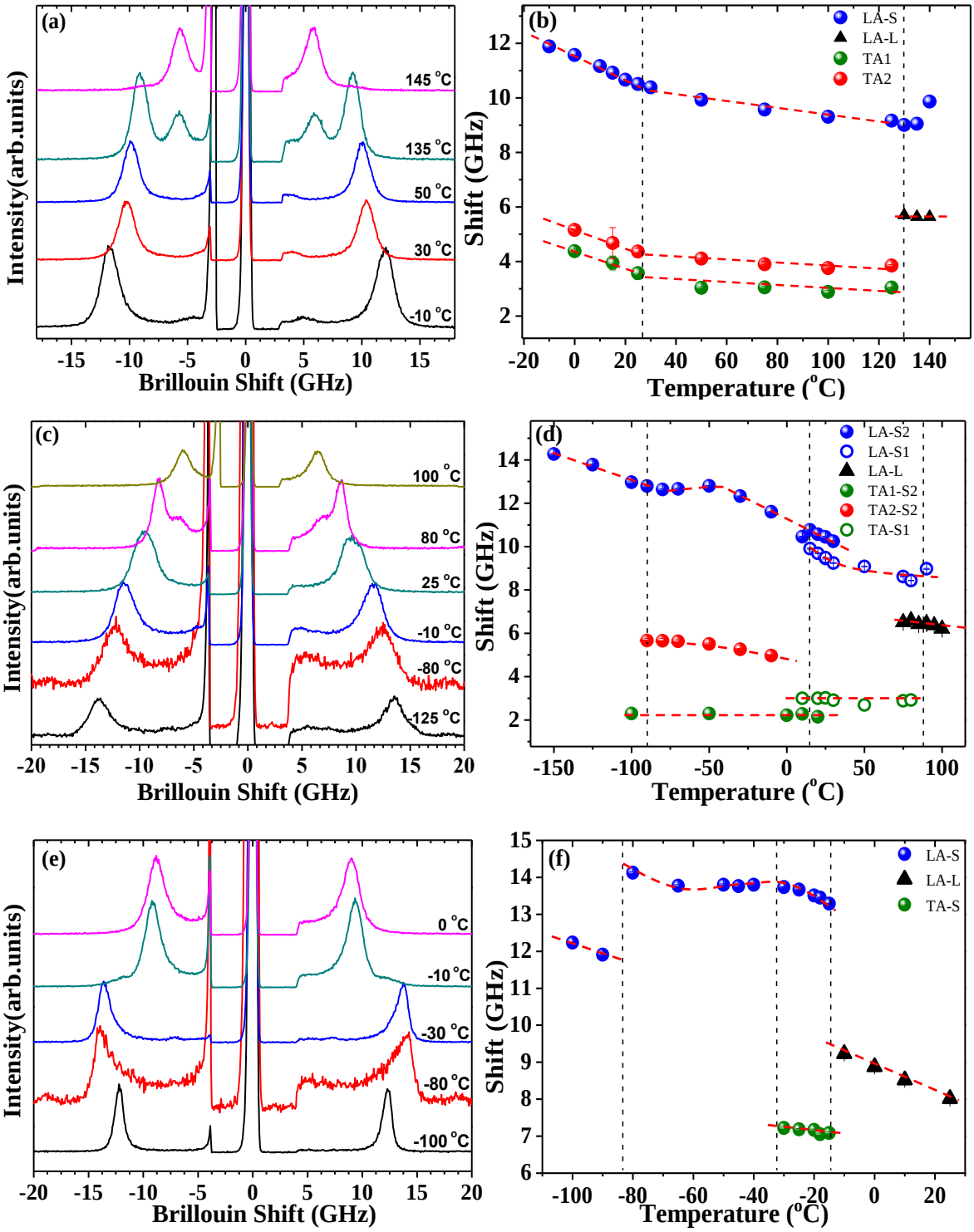


Fig. 6.4. The temperature evolution of the Brillouin spectra (left panel) and (b) the temperature dependence of the acoustic modes (right panel) in $P_{11}$TFSI (a, b), $P_{12}$TFSI (c, d) and $P_{14}$TFSI (e, f). The Brillouin shift of LA modes in solid and liquid phase is represented by blue circles and black triangles, respectively. The red and green circles represent the Brillouin shift of the TA modes. The red dotted lines are the guide to the eyes and black dashed lines correspond to the phase transition temperatures determined from DSC measurements.

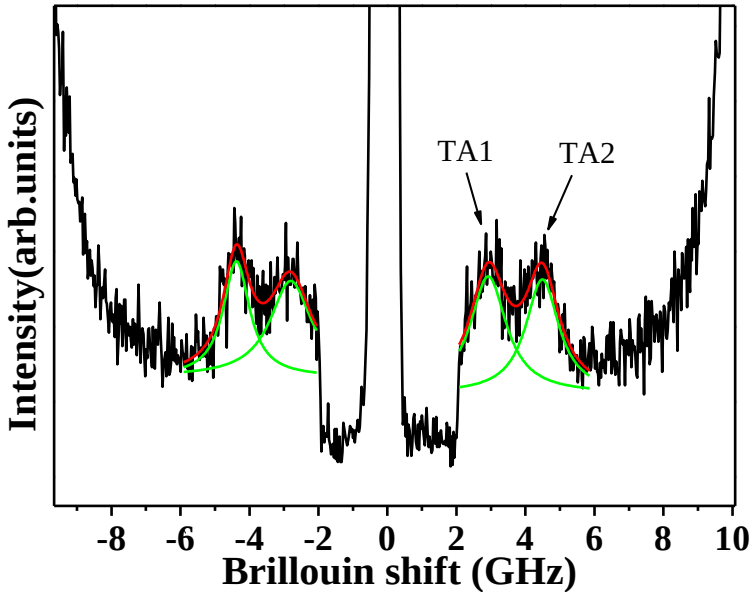


Fig. 6.5. The deconvoluted TA modes of $P_{11}$TFSI at 25 ºC.

Another important feature of $P_{12}$TFSI in comparison to $P_{11}$TFSI and $P_{14}$TFSI is its sluggishness during melting. Though melting transition is at 86 ºC in $P_{12}$TFSI, both liquid and solid phases coexist over a larger period, which is evident from the emergence of the LA mode of the liquid phase at ~ 70 ºC. The LA modes corresponding to both liquid and solid phases can be observed over a large temperature regime in this system.

Ideally, two TA modes should be observed in a solid phase which is generally represented by TA1 (minimum) and TA2 (maximum). In $P_{11}$TFSI we could see two TA modes at all solid phases. In $P_{12}$TFSI, TA1 and TA2 occurs at ~ 5 and ~ 2.2 GHz, respectively in the solid phase 2 (where LA-S2 is observed) while we see only one TA mode at ~ 2.7 GHz in phase 1 (where LA-S1 is observed). The Brillouin shift of the TA1 modes appears at ~ 3.6 GHz and ~ 7 GHz for $P_{11}$TFSI and $P_{14}$TFSI, respectively (TA2 was also observed at ~ 8 GHz for $P_{14}$TFSI but the signal was too weak and hence not shown in Fig. 6.4). Though heavier than $P_{11}$TFSI, the low Brillouin shift of the LA as well as the TA modes exhibited by $P_{12}$TFSI indicates the high plasticity in these systems. Assuming a refractive index of 1.4 (which is in general observed for most ILs) [27], the velocity of TA1 in phases S1 and S2 of $P_{12}$TFSI corresponds to 420 and 515 m/s, respectively which is the lowest yet observed for any molecular solids [28]. The exceptionally low values of the TA modes observed here imply that plastic crystals possess extremely low shear modulus and this can be used as a measure of the plasticity. $P_{14}$TFSI also exhibit TA modes in its solid state

and interestingly, TA modes are not observed throughout the crystalline phase and instead it is observed only in certain temperature range (between -35 ºC and -18 ºC) below melting. This indicates the commencement of the disordered SCL phase on decreasing the temperature.

On cooling below the glass transition temperatures, $P_{12}$TFSI and $P_{14}$TFSI transform into glassy crystal and structural glass, respectively. From the temperature dependence of the Brillouin shift, we can differentiate between these two glass phases. In $P_{12}$TFSI, the transition from SPC to glassy crystal is manifested by a change in slope while in the case of $P_{14}$TFSI, the transition from SCL to structural glass shows a discontinuity in the Brillouin shift.

In order to understand the dynamics of these systems, it is required to correlate the Brillouin data with the structural origin of rotar phases. It is observed that plasticity in the solid state is a phenomenon strongly appearing for smaller $P_{1n}$TFSI, n = 1, 2 compounds, but is absent for the larger alkyl substituents, n = 4. Therefore it appears that the behavior is more likely to be associated with the cation *i.e.*, pyrrolidinium. Generally, the molecule would require considerable free volume in its surrounding area in order to rotate around any of the obvious axes. Pyrrolidinium ring is close to planar and has several axes of rotation which might be active in the solid plastic phases, in particular rotations about an axis normal to the ring. This type of rotation may be possible in the crystalline state with an accessible energy barrier for the smaller alkyl substituents (methyl, ethyl). On the other hand for larger alkyl substituents (butyl) the alkyl side chain may become too bulky to allow free rotation about such an axis and the rotator phases are thus not accessible.

Dynamics of these ionic liquids can be clearly observed from the temperature variation of the FWHM as shown in Fig. 6.6. For all the samples, significant changes in the magnitude of FWHM can be observed in the proximity of phase transitions. In $P_{11}$TFSI and $P_{12}$TFSI at the solid-solid transition, the FWHM suddenly increases and then decreases resulting in a peak-like feature at the transition points. Broadening of the Brillouin mode (increase of FWHM) from room temperature to the transition temperature is a consequence of decrease in life time (fast relaxation) due to the disordered structure. In addition, the rotational motion in plastic phase induces higher degree of disorder in the sample leading to faster dynamics. This shows that disorder and the dynamics of the system increases at each transition. In the solid phase, the FWHM of $P_{11}$TFSI increases as the temperature is decreased till certain temperature after which it decreases as shown in Fig. 6.6(a).

Increase in FWHM below melting temperature indicates the presence of the disordered plastic phase, while the sharp decrease below 20 ºC is attributed to the transition from a rotator plastic crystalline phase to an ordered crystalline phase. Coexistence of two phases (Fig. 6.6(b)) below melting temperature in case of $P_{12}$TFSI is expected to be due to the presence of several disorder phases in the plastic phase. And the almost constant value of FWHM between ~10 °C to -70 °C for $P_{12}$TFSI indicates relatively ordered state in the plastic phase.

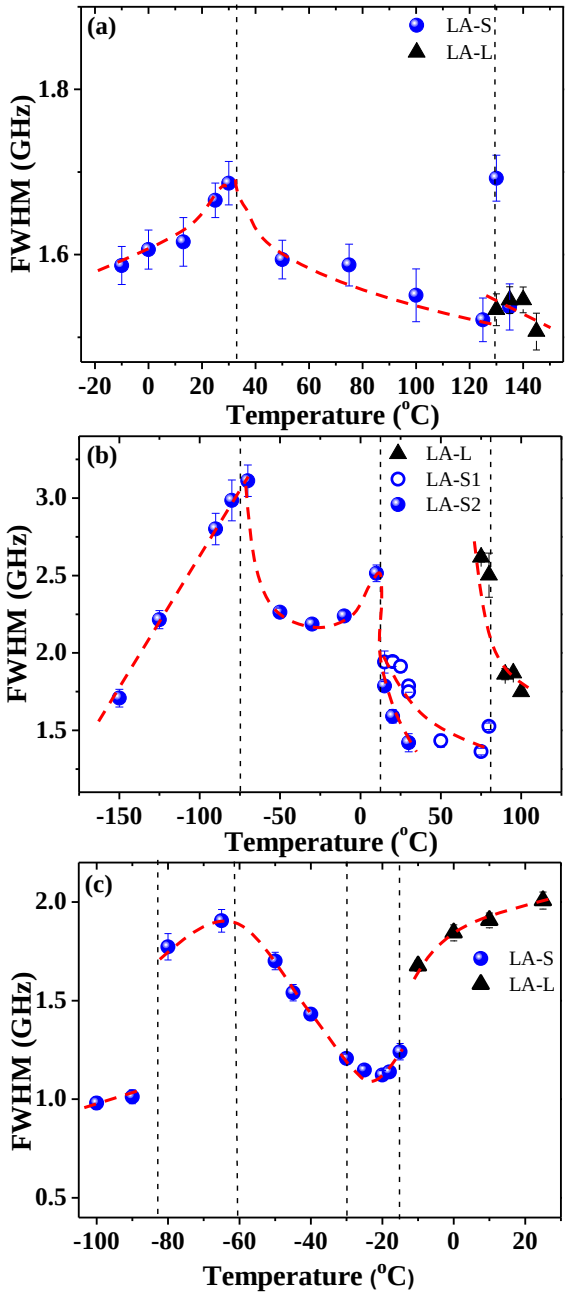


Fig. 6.6. The temperature dependence of the FWHM of (a) $P_{11}$TFSI (b) $P_{12}$TFSI and (c) $P_{14}$TFSI.

The sharp decrease in FWHM at much lower temperature ($T \approx$ -80 °C) is related to increase in life time (slow relaxation) after the formation of a glass phase and can be seen for the case of $P_{14}$TFSI also. It is interesting to observe the variation of FWHM with temperature for $P_{14}$TFSI (Fig. 6.6(c)). Here, for $T < T_m$ the FWHM for $P_{14}$TFSI is almost constant compared to $P_{1n}$TFSI (n = 1, 2). This unusual behaviour below melting (T < -18 °C) temperature signifies less plasticity in this ionic liquid and the presence of ordered plastic solid crystalline phase. The large value of FWHM for temperatures < -35 ºC provides the evidence for the presence of supercooled glassy liquids which is attributed to the presence of disorder in all three directions. A comparison of the FWHM of these ionic liquids at -20 °C (when all are in solid state) reveals that FWHM of $P_{12}$TFSI > $P_{11}$TFSI > $P_{14}$TFSI, implying that $P_{12}$TFSI is highly disordered when compared to the other ILs and hence exhibit higher plasticity. Also it has to be noted that in the plastic crystal phase of all ILs, the FWHM increases with lowering the temperature which is contrary to that observed in a crystalline solid or in a glass. This can be attributed to the increase in the steric hindrance between the ions which stems from the contraction of the lattice as the temperature is decreased resulting in an average higher disorder.

A careful inspection of Figs. 6.4(a, c, e) shows that at low temperature, few of the Brillouin peaks are comparatively asymmetric in its low frequency side. This asymmetric line shape can be accounted by Fano resonance which is attributed to the electron–phonon coupling phenomenon. Whenever necessary, the line-shape parameters like peak frequency, FWHM, and intensity were extracted by a non-linear least square fitting of the data with a Fano line shape function [29] along with an exponential background and otherwise using a Lorentzian function. The Fano function along with the exponential background is given by the expression

$$y = y_0 + A\left[\left(q + \left(\frac{2(\omega - \omega_C)}{w}\right)\right)^2 / (1 + \left(\frac{2(\omega - \omega_C)}{w}\right)^2)\right] + Be^{\omega/C} \quad (6.1)$$

where, $\omega_C$ = resonance frequency, $\omega$ = frequency, $w$ = FWHM, $q$ = asymmetry parameter or Fano parameter; $A$, $B$, $C$ = constants and a low $q$ value suggests a higher asymmetry. $P_{11}$TFSI was fitted with a Lorentzian function throughout the whole temperature range. However Fano line shape was used in some cases of $P_{12}$TFSI and $P_{14}$TFSI. The asymmetry in the lineshape can also arise from the coupling between the central peak and

the acoustic mode. The Brillouin spectrum fitted by Lorentzian and Fano lineshape for $P_{14}$TFSI at -80 °C is shown in Fig. 6.7. It can be seen that reliable fitting of the spectrum is obtained only when Fano lineshape is used as we could not fit the spectrum using a Lorentzian function for the LA and considering the central peak. Also, Fano lineshape was used earlier to extract the lineshape parameters in certain plastic crystal by Supti *et al* [30]. The q value increased from ~ 5 to 9 as the temperature is increased from -150 °C to -30 °C in the case of $P_{12}$TFSI. $P_{14}$TFSI shows lower q values ranging from ~ 3 to 7 as the temperature is increased from -80 °C to -18 °C. Relatively low values of Fano parameter ($q < 3$) exhibited by $P_{14}$TFSI suggests the presence of electron-phonon coupling at low temperature. In general, pure IL freezes to a more compact conformation below $T_m$ where the backbone electrons are localized via pinning of the lattice. This pinning effect increases the probability of coupling of electrons with the lattice phonons and a higher steric hindrance attributed to the increase in size of the side chain induces more coupling. Hence, the asymmetric line shape at low temperature exhibited by $P_{14}$TFSI suggests a higher electron-phonon coupling existing in this system credited to the immobile and bulkier $P_{14}^{+}$ ion.

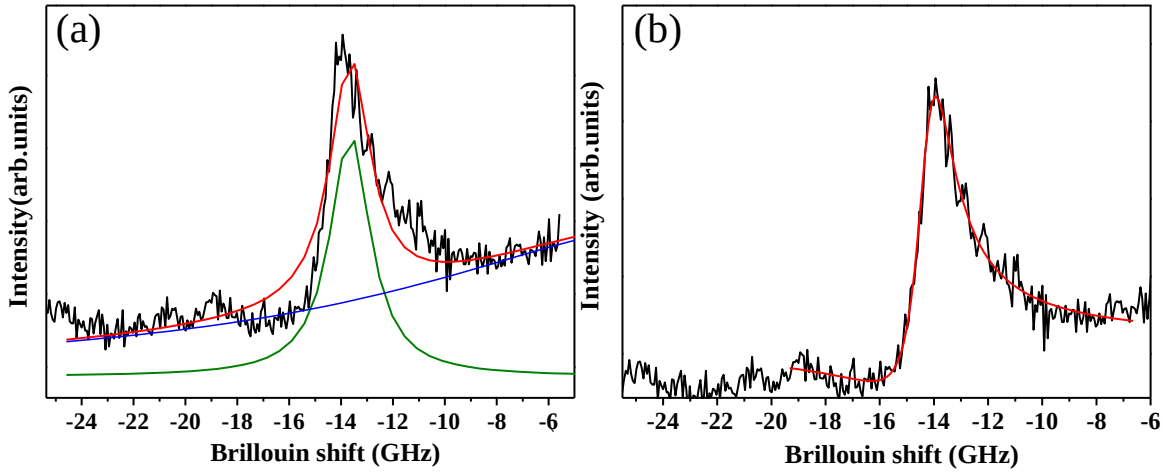


Fig. 6.7. The Brillouin spectrum of $P_{14}$TFSI at -80 °C, fitted using (a) Lorentzian and (b) Fano lineshape. A better fitting of the spectrum was obtained when Fano lineshape was used. The green line and blue line in (a) are the Lorentzian curve and tail of the central peak, respectively. The red line is the cumulative fitted curve.

## 6.4. Conclusions

Brillouin Scattering has been used to study the melting and crystalline phase transition of room temperature ionic liquid N-methyl-N-butylpyrrolidinium bis(trifluorosulfonyl)

imide and plastic crystal phases of dimethylpyrrolidinium bis(trifluorosulfonyl) imide & N-ethyl-N-methylpyrrolidinium bis(trifluorosulfonyl) imide. All ionic liquids shows plasticity in certain temperature ranges. We envisage that the low transverse acoustic velocities as well as the high linewidth exhibited in the solid phase of a few of these systems are indicators of the plasticity of a system as evidenced from the case of $P_{12}$TFSI. Both $P_{11}$TFSI and $P_{12}$TFSI show faster relaxation in the plastic phase signifying their higher conductivity in the solid state. Our study also shows that, Brillouin spectroscopy can be used as a tool to easily identify the glassy crystal (in the case of $P_{12}$TFSI) and structural glass (in the case of $P_{14}$TFSI) phases as their Brillouin shift and FWHM exhibit different temperature dependent behavior.

## 6.5. Bibliography

[1] M. Galiński, A. Lewandowski, and I. Stępniak, Electrochimica Acta **51**, 5567 (2006).

[2] Y. Fukaya and H. Ohno, Physical Chemistry Chemical Physics **15**, 4066 (2013).

[3] D. MacFarlane, P. Meakin, J. Sun, N. Amini, and M. Forsyth, The Journal of Physical Chemistry B **103**, 4164 (1999).

[4] C. Forsyth, D. MacFarlane, J. Golding, J. Huang, J. Sun, and M. Forsyth, Chemistry of Materials **14**, 2103 (2002).

[5] J. Golding, N. Hamid, D. MacFarlane, M. Forsyth, C. Forsyth, C. Collins, and J. Huang, Chemistry of Materials **13**, 558 (2001).

[6] A. Lewandowski and A. Świderska-Mocek, Journal of Power Sources **194**, 601 (2009).

[7] L. Grande, E. Paillard, G.-T. Kim, S. Monaco, and S. Passerini, International journal of molecular sciences **15**, 8122 (2014).

[8] T. Kuboki, T. Okuyama, T. Ohsaki, and N. Takami, Journal of Power Sources **146**, 766 (2005).

[9] M. Kar, T. J. Simons, M. Forsyth, and D. R. MacFarlane, Physical Chemistry Chemical Physics **16**, 18658 (2014).

[10] G. A. Elia *et al.*, Nano Letters **14**, 6572 (2014).

[11] H. Weingärtner, P. Sasisanker, C. Daguenet, P. J. Dyson, I. Krossing, J. M. Slattery, and T. Schubert, The Journal of Physical Chemistry B **111**, 4775 (2007).

[12] T. Echelmeyer, H. W. Meyer, and L. van Wüllen, Chemistry of Materials **21**, 2280 (2009).

[13] J. Hunger, A. Stoppa, S. Schrödle, G. Hefter, and R. Buchner, ChemPhysChem **10**, 723 (2009).

[14] K. Iwata, H. Okajima, S. Saha, and H.-O. Hamaguchi, Accounts of chemical research **40**, 1174 (2007).

[15] H. L. Ngo, K. LeCompte, L. Hargens, and A. B. McEwen, Thermochimica Acta **357**, 97 (2000).

[16] L. Jin, P. Howlett, J. Efthimiadis, M. Kar, D. Macfarlane, and M. Forsyth, Journal of Materials Chemistry **21**, 10171 (2011).

[17] J. Adebahr, P. Johansson, P. Jacobsson, D. MacFarlane, and M. Forsyth, Electrochimica Acta **48**, 2283 (2003).

[18] O. Borodin and G. D. Smith, The Journal of Physical Chemistry B **110**, 11481 (2006).

[19] D. R. MacFarlane, J. M. Pringle, P. C. Howlett, and M. Forsyth, Physical Chemistry Chemical Physics **12**, 1659 (2010).

[20] A. Triolo, O. Russina, C. Hardacre, M. Nieuwenhuyzen, M. A. Gonzalez, and H. Grimm, The Journal of Physical Chemistry B **109**, 22061 (2005).

[21] M. Asaki, A. Redondo, T. Zawodzinski, and A. Taylor, The Journal of chemical physics **116**, 10377 (2002).

[22] H. Shirota, A. M. Funston, J. F. Wishart, and E. W. Castner Jr, The Journal of chemical physics **122**, 184512 (2005).

[23] F. Shi and Y. Deng, Spectrochimica Acta Part A: Molecular and Biomolecular Spectroscopy **62**, 239 (2005).

[24] M. Ribeiro, The Journal of chemical physics **133**, 024503 (2010).

[25] L. F. Faria, J. R. Matos, and M. C. Ribeiro, The Journal of Physical Chemistry B **116**, 9238 (2012).

[26] R. Brand, P. Lunkenheimer, and A. Loidl, The Journal of Chemical Physics **116**, 10386 (2002).

[27] M. Shamsipur, A. A. M. Beigi, M. Teymouri, S. M. Pourmortazavi, and M. Irandoust, Journal of Molecular Liquids **157**, 43 (2010).

[28] A. I. Kitaigorodsky, *Molecular Crystals and Molecules* (Academic press, Inc., New York, 1973).

[29] U. Fano, Physical Review **124**, 1866 (1961).

[30] S. Das, V. S. Bhadram, C. Narayana, and A. J. Bhattacharyya, J. Phy. Chem. B **115**, 12356 (2011).

# Chapter 7

# High pressure Brillouin study of spin ice pyrochlore $Dy_2Ti_2O_7$

*The author's main contribution in this chapter is to perform the high pressure Brillouin measurements on $Dy_2Ti_2O_7$ and analyze the data. Sample was provided by Prof. Ajay K Sood's and Dr. D. Victor S. Muthu's group, IISc, Bangalore, along with the inputs on high pressure Raman spectroscopy measurements. The x-ray diffraction studies were done by Prof. S. M Sharma's group, BARC, Mumbai.*

Dhanya Radhakrishnan, A K Mishra, H. K. Poswal, Pallavi Ghalsasi, D V S Muthu, Chandrabhas Narayana, S M Sharma, Ajay K Sood, *"High Pressure Studies on Spin Ice Pyrochlore $Dy_2Ti_2O_7$: X-ray Diffraction, Brillouin and Raman Spectroscopic Investigations"* (manuscript prepared).

## 7.1. Introduction

The rare earth oxides ($A_2B_2O_6O'$) with pyrochlore structure (Fig. 7.1) have a variety of technological applications due to their diverse physical properties. These applications range from high permittivity ceramics, thermistors, thick film resistors, electrodes, to solid oxide fuel cell components *etc* [1]. The pyrochlores with their 'B' site cation as IV B transition elements (Ti, Zr) are good candidates for immobilization of actinides and hence can be used for radioactive waste disposal [2, 3]. In fact, the zirconate pyrochlores ($Gd_2Zr_2O_7$) have been identified as nuclear waste encapsulator materials due to their enhanced resistance threshold to radiation induced damages [4]. In addition to this, most of the pyrochlore oxides which crystallize in to Kagome lattice and have magnetic $A^+$ or $B^+$ cations are geometrically frustrated antiferromagnets [5]. In these geometrically frustrated magnets, frustration of spins to order and minimize their exchange energies leads to a macroscopically degenerate ground state [6]. However, competing interactions like near neighbor dipolar, crystal field interactions, quantum fluctuations *etc.* can lift the degeneracy resulting into various complex ground states at very low temperatures, for example, spin-liquid, spin-ice and spin-glass. Subjecting such interesting compounds to high pressures can change the delicate balance between the various competing interactions and may lead to the realization of different physical states. For example, $Tb_2Ti_2O_7$ is the only member of the pyrochlore titanates that remains in spin-liquid state down to 70 mK [7]. However, under external pressure of ~ 8.6 GPa, $Tb_2Ti_2O_7$ transforms into a mixed phase of spin-liquid and spin-solid at 1.5 K, as revealed by neutron scattering experiments [8]. Earlier, a structural transition has been observed in spin-liquid $Tb_2Ti_2O_7$ [9] and $Gd_2Ti_2O_7$ [10], linking to the proposed broken symmetry [11] and cubic-to-tetragonal structural fluctuations below 20 K [12]; thus attributing the structural instability of $Tb_2Ti_2O_7$ to its unique spin-liquid state [13].

In the high pressure regime, experimental measurements reveal that $Sm_2Ti_2O_7$ and $Gd_2Ti_2O_7$ pick up anion disorder at ~ 40 GPa [14]. Interestingly in all these pressure induced changes, the cubic structure of the pyrochlore is retained, implying its inherent stability even under quite high pressures. Previous high pressure x-ray diffraction (XRD) study has revealed cubic to monoclinic phase transition in $Ho_2Ti_2O_7$, $Y_2Ti_2O_7$ and $Tb_2Ti_2O_7$ near 37, 42 and 39 GPa, respectively [15]. In an earlier study, the transition pressure for $Tb_2Ti_2O_7$ is reported to be ~ 51 GPa [16].

$Dy_2Ti_2O_7$ crystallizes into the pyrochlore structure with the space group $Fd\bar{3}m$ and lattice parameter 10.109 Å at room temperature [17]. It exhibits spin ice like ground state known as dipolar spin ice at very low temperature, which is a unique property among all the known titanate pyrochlores [18]. The spin ice ground state is analogous to the ordering of protons in ordinary water ice [19] with a pair of spins pointing inward and another pair of spins pointing outward on an elementary tetrahedron. The reported existence of magnetic monopoles in $Dy_2Ti_2O_7$ has also made it an interesting material to study [20]. The high pressure Raman and XRD measurements on $Dy_2Ti_2O_7$ indicates a structural distortion at ~ 9 GPa with a possible lattice instability across this pressure [21]. In this chapter, we have carried out high pressure Brillouin measurements to study the pressure dependence of the elastic constants of $Dy_2Ti_2O_7$.

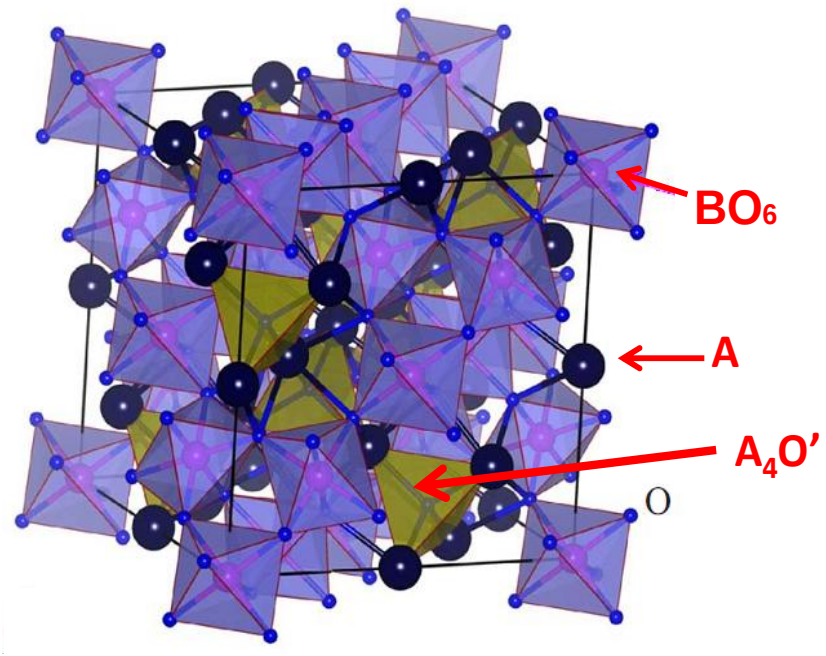


Fig. 7.1. The structure of pyrochlore lattice.

## 7.2. Experimental details

Stoichiometric amounts of $Dy_2O_3$ (99.99%) and $TiO_2$ (99.99%) were mixed thoroughly and heated at 1200 °C for about 15 hours. The resulting mixture was well ground and iso-statically pressed into rods of about 6 cm long and 5 mm diameter. These rods were sintered at 1400 °C in air for about 72 hours. This procedure was repeated until the compound $Dy_2Ti_2O_7$ was formed, as revealed by powder x-ray diffraction analysis, with no traces of any secondary phase. These rods were then subjected to single-crystal growth

by the floating-zone method in an infrared image furnace under flowing oxygen. X-ray diffraction measurements, carried out on the powder obtained by crushing a part of the single crystalline sample and energy dispersive x-ray analysis carried out in a scanning electron microscope confirmed the formation of a pure pyrochlore $Dy_2Ti_2O_7$ phase.

Brillouin experiments were performed in back scattering geometry with a 532 nm excitation from Nd:YAG laser (details in Chapter 2) with a free spectral range of 83 GHz. High pressure Brillouin experiments were carried out using a membrane type diamond anvil cell (DAC). In-situ pressure was determined using ruby fluorescence technique. Experiments were conducted in two pressure transmitting mediums: (1) Methanol: ethanol: water (16:3:1) mixture and (2) millipore water. This was done to ascertain that the transition at 9 GPa is not due to the change in hydrostaticity of the medium.

The sample was loaded inside DAC with unknown orientation and multiple sets of experiments were performed. Ideally Brillouin spectrum should contain two transverse acoustic modes, TA1 (slow) and TA2 (fast). But in most cases we could observe only one TA mode which occurs at ~ 34 GHz *i.e.,* TA1 and TA2 was rarely observed. This set of experiments when only TA1 is observed is denoted as *case 1*. To observe TA2, the sample was rotated along both θ (polar) and φ (azimuthal) directions so that, TA modes with maximum splitting is obtained. Figure 7.2(a) shows the phi dependence of the Brillouin shift and it can be observed that both TA modes are obtained simultaneously in certain directions only. Figure 7.2(b) shows the Brillouin spectra in a specific direction where all the three acoustic modes are observed and with a maximum separation between TA1 and TA2. The LA mode appears at ~ 62 GHz and the TA modes appear at ~ 34 GHz (TA1) and ~ 36 GHz (TA2). A thin slice of the crystal in this orientation was loaded inside the DAC for performing the high pressure experiment. It is known that only along few crystallographic directions we can see all the three acoustic modes with <110> direction showing the maximum separation between the two TA modes [22,23]. Thus, this direction was assumed as <110> direction and is denoted as *case 2*. The velocity thus determined from *case 2* can be used to obtain all the elastic constants, assuming that the experiments are performed along <110> direction while envelope method can be used to derive the elastic constants from *case 1*.

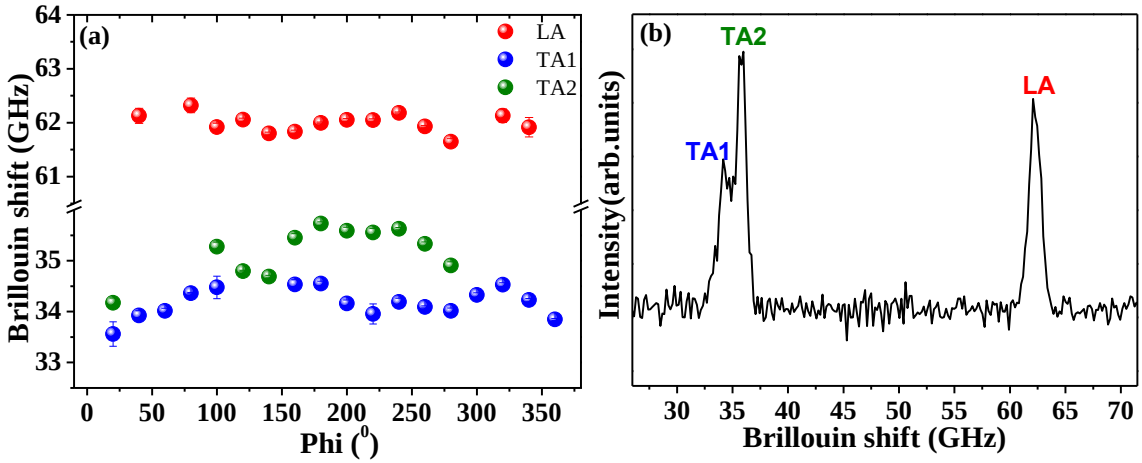


Fig. 7.2. (a) The Brillouin shift *vs.* phi and the (b) Brillouin spectrum as obtained in *case 2* for $Dy_2Ti_2O_7$.

## 7.3. Results and discussions

Figure 7.3 shows the pressure dependence of the Brillouin shift of acoustic modes observed in *case 2*. As the pressure is increased, all the modes harden initially. But around 9 ± 1 GPa, we see a slope change in the LA mode while TA modes are seen to soften above this pressure, thus indicating a phase transition. This is in accordance with the Raman and XRD measurements which also show a transition around the same pressure.

Acoustic velocities can be determined from the Brillouin shift using Eq. 1.11. In calculating the pressure dependent acoustic velocities, the refractive index was assumed to be constant (= 2.39 [24]) throughout the pressure range investigated. This may lead to over or under estimation of the values of the acoustic velocities/elastic constants calculated. But it is well known that refractive index will undergo huge change with pressure only when the bulk modulus (B) of the material is low. For example, pressure dependence of the refractive index (dn/dP) changes by 0.024/GPa for KBr (B=14.8 GPa) and by 0.0117/GPa for NaCl (B=23 GPa) [25,26] while for materials of higher bulk modulus like SiC (B=227 GPa), Diamond (B= 442 GPa) the dn/dP changes by -0.002/GPa and -0.0008/GPa, respectively [27]. $Dy_2Ti_2O_7$ also has a high bulk modulus (~201 GPa at ambient pressure and ~260 GPa beyond the phase transition at 9 GPa as determined from XRD measurements) and hence the refractive index will change only slightly with pressure. Thus the pressure dependent change in the refractive index will be only in the third decimal. Here we are using refractive index which is precise only to the

second decimal. And hence only slight errors in the elastic constants should be expected and the trend in the pressure dependence of the elastic constant will not be effected.

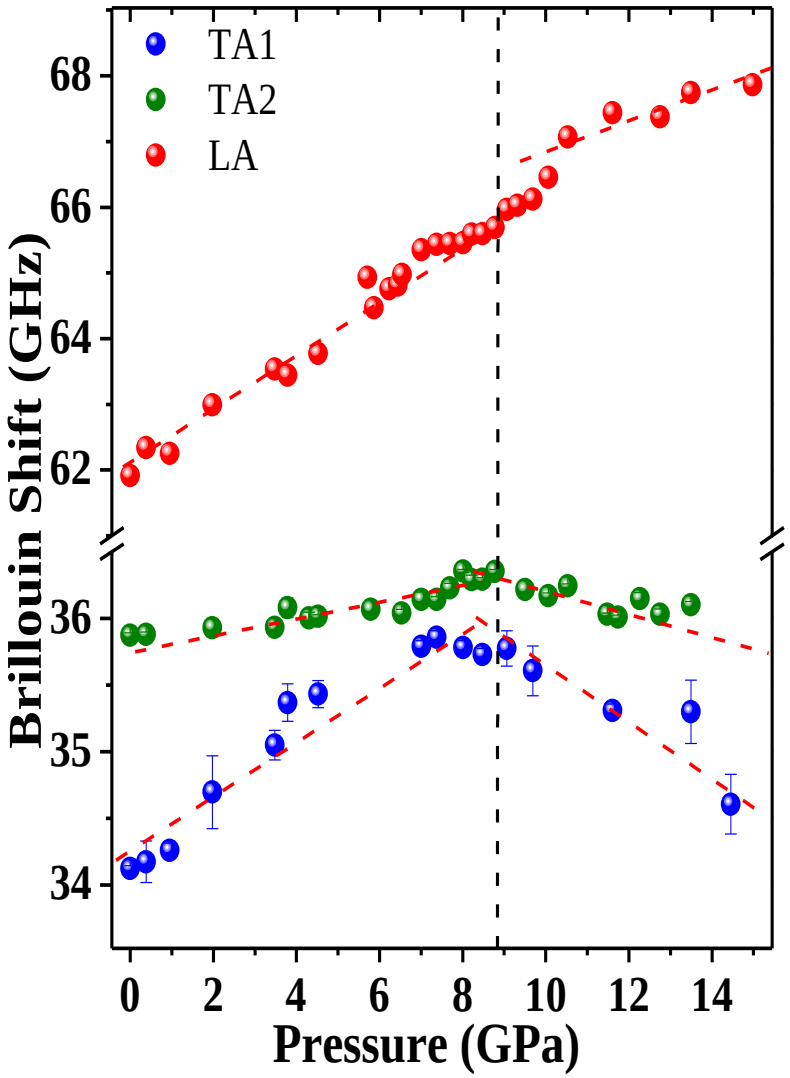


Fig. 7.3. The pressure dependence of LA, TA1 and TA2 modes in $Dy_2Ti_2O_7$ obtained in *case 2*. The red dashed lines are guide to the eyes and black vertical line corresponds to the pressure where transition is observed.

The velocity thus determined from the Brillouin shift can be then used to calculate the elastic constants of the sample. Generally, cubic crystal systems will have three elastic constants $C_{11}$, $C_{12}$ and $C_{44}$ [28]. For an elastically isotropic material, this will be reduced to two ($C_{11}$ and $C_{44}$). The elastic anisotropy can be measured in terms of anisotropic factor, $A = V_{TA2}^2/V_{TA1}^2 = (2C_{44}) / (C_{11} - C_{12})$ (Chapter 1). The anisotropic factor determines how TA1 and TA2 are related to the elastic constants $C_{44}$ and ($C_{11}$-$C_{12}$)/2 when $A \neq 1$. When $A > 1$, which happens in most materials, $C_{44}$ will be larger than ($C_{11}$-$C_{12}$)/2, implying that TA2 depends on $C_{44}$ while the reverse happens when $A < 1$, *i.e.*,

TA1 will depend on $C_{44}$. Anisotropic factor is found to be less than 1 in $Dy_2Ti_2O_7$ from the resonant ultrasonic measurements (RUS) [29]. Hence in this case the TA1 observed will be related to the elastic constant $C_{44}$ and TA2 will be related to $(C_{11}-C_{12})/2$.

The relation between the elastic constants and acoustic velocities in various high symmetry directions when A is less than 1 is given as [22,30,31]:

$$V_{LA,max}^2 = C_{11}/\rho \text{ along } <100> \quad 7.1(a)$$

$$V_{LA,min}^2 = (C_{11}+2C_{12+}{}_4C_{44})/3\rho \text{ along } <111> \quad 7.1(b)$$

$$V_{TA1,min}^2 = C_{44}/\rho \text{ along } <110> \quad 7.2(a)$$

$$V_{TA2,max}^2 = (C_{11}-C_{12})/2\rho \text{ along } <110> \quad 7.2(b)$$

$$V_{LA}^2 = (2C_{44}+C_{11}+C_{12})/2\rho \text{ along } <110> \quad 7.2(c)$$

These equations can be used for determining the values of $C_{11}$, $C_{12}$ and $C_{44}$, once the pressure dependence of density, $\rho$ is known from the XRD measurement. Eq. 7.2(a-c) can be used to calculate the elastic constants from *case 2*.

It has to be mentioned that the TA1 in *case 2* became very weak (Fig. 7.4) at high pressures (greater than 5 GPa) and it was difficult to resolve this peak at certain pressures due to its overlap with the LA mode of the medium. Hence, data from *case 1* where an intense TA1 was observed was also used to calculate $C_{44}$ using envelope method (Eq. 7.2(a)). Figure 7.5 shows the envelope curve obtained for the LA modes in all the experimental runs. Eq. 7.1(a) and Eq. 7.1(b) can be used to derive the elastic constants $C_{11}$ and $C_{12}$ from the lower and upper bounds of LA using envelope method. A comparison of the elastic constants obtained from RUS [29] with the values obtained from our studies at ambient conditions is shown in Table 7.1. The elastic constants obtained from *case 2* agrees well with the RUS measurement, but the elastic constants obtained using envelope method have an error of ~ 3% compared to that determined from *case 2*. This could be a consequence of the uncertainty in determining the lower and upper limits of the acoustic velocities when envelope method is employed. Nevertheless, the pressure dependence of the elastic constants determined from both envelope method and *case 2* were similar.

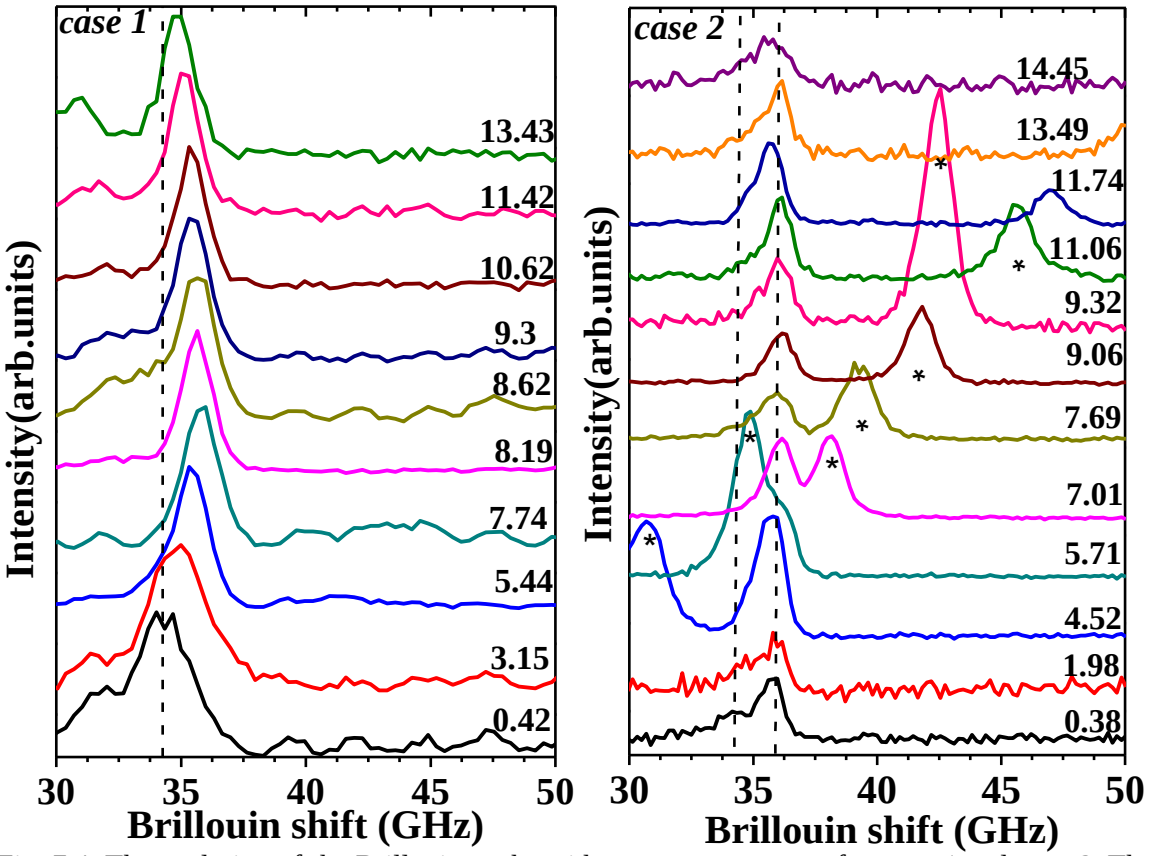


Fig. 7.4. The evolution of the Brillouin peaks with respect to pressure for *case 1* and *case 2*. The dashed lines correspond to the Brillouin shift of TA modes which occurs at ~ 34 GHz (TA1) in *case 1* and ~ 34 GHz (TA1), 36 GHz (TA2) in *case 2* at ambient pressure. The * corresponds to the LA mode of the pressure transmitting medium.

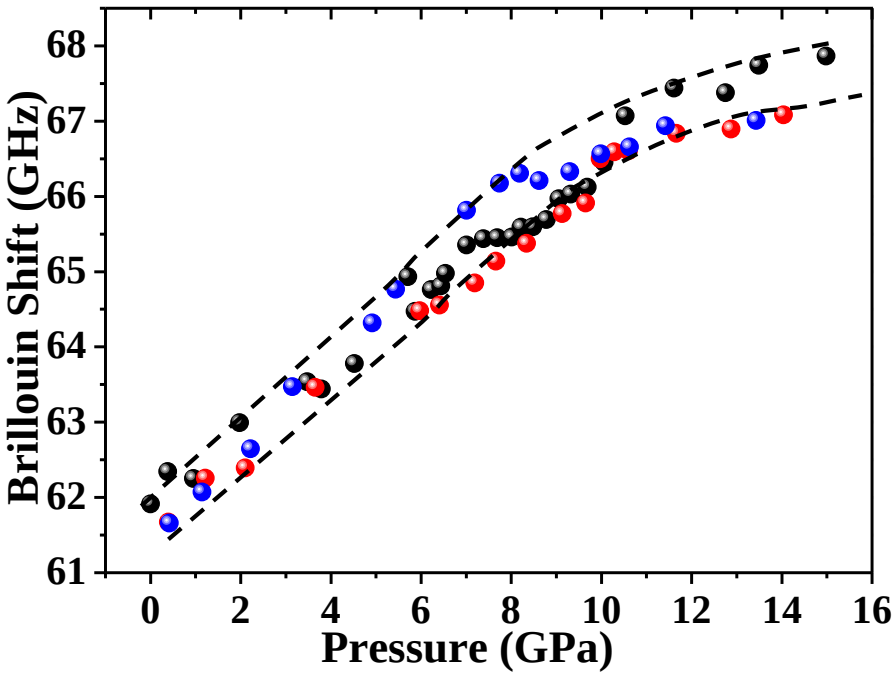


Fig. 7.5. Pressure dependence of LA modes observed in all the experimental runs. The upper and lower bounds of LA are shown by dashed lines.

Table. 7.1. A comparison of the elastic constants, anisotropic ratio (A) and bulk modulus (B) obtained using Brillouin and RUS [29] at ambient conditions.

| | $C_{11}$ (GPa) | $C_{12}$ (GPa) | $C_{44}$ (GPa) | A (GPa) | B (GPa) |
|---|---|---|---|---|---|
| Present studies (*case 2*) | 3.44 | 1.20 | 1.01 | 0.90 | 1.948 |
| Present studies (envelope method, *case 1*) | 3.366 | 1.17 | 1.038 | 0.94 | 1.899 |
| RUS | 3.47 | 1.22 | 0.973 | 0.87 | 1.97 |

The pressure dependence of the elastic constants determined from *case 2* is shown in Fig. 7.6. It is seen that $C_{11}$ and $C_{12}$ shows a slope change around 9 GPa while $C_{44}$ soften beyond this pressure. The adiabatic bulk modulus ($B = (C_{11}+2C_{12})/3$) also shows a change near 9 GPa, with a sudden increase in its value above the transition (Fig. 7.7(a)). The anisotropic factor was seen to increase with an increase in the pressure till 9 GPa above which it was seen to soften, though the overall change is very small (Fig. 7.7(b)).

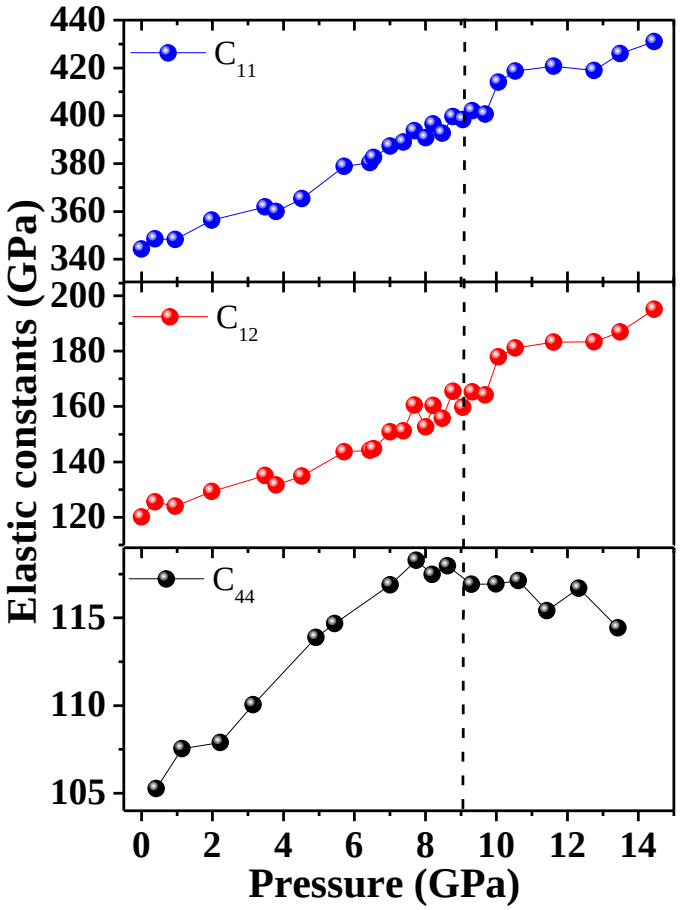


Fig. 7.6. Pressure dependence of the elastic constants obtained for *case 2*. The dashed vertical line corresponds to the transition at 9 GPa.

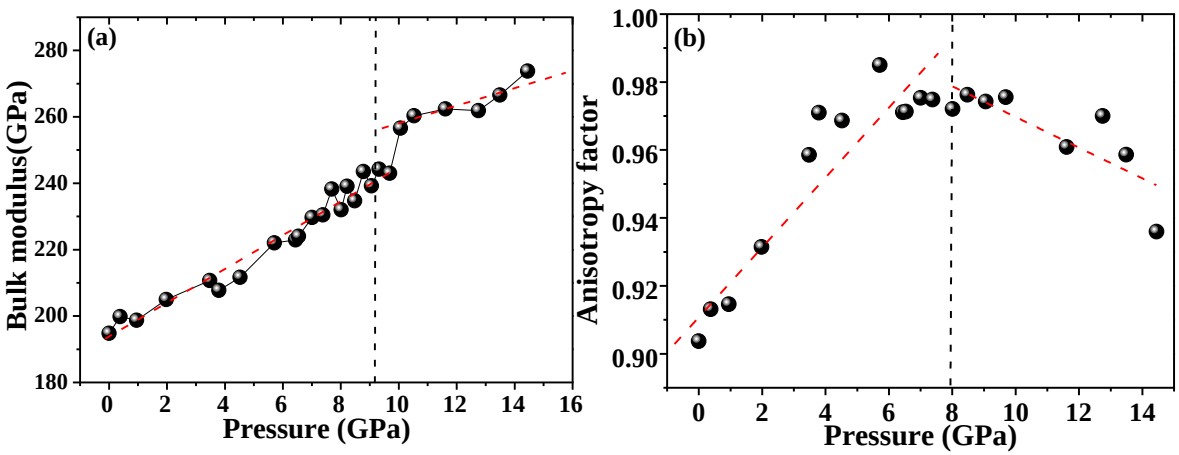


Fig. 7.7. The pressure dependence of (a) bulk modulus and (b) anisotropic factor.

Raman and XRD studies show that the structure of $Dy_2Ti_2O_7$ is stable up to 40 GPa. The XRD studies show that the transition at 9 GPa is an iso-structural transition with only a discontinuity in the volume which is accompanied by a rearrangement of $TiO_6$ octahedra. Pressure dependent shear softening have been observed in materials like ZnO, stishovite, coesite *etc.* prior to phase-transition and indicates the destabilization of the structure [32-34]. Shear softening is also known to be a precursor for first order phase transition which can be induced by temperature or pressure [32-34]. Thus our Brillouin studies show that the transition at 9 GPa will be followed by a mechanical instability in the system which is evident from the shear softening behavior. The vanishing of the elastic constant $C_{44}$ on applying pressure indicates a mechanical instability when the Born's stability condition are not be satisfied and phase transition occurs when $C_{44} = 0$, as observed in the case of calcium oxide [35]. Similarly, extrapolating the value of $C_{44}$ in $Dy_2Ti_2O_7$ suggests a phase transition occurring at ~ 160 GPa.

## 7.4. Conclusions

High pressure Brillouin studies have been carried out in the spin ice pyrochlore $Dy_2Ti_2O_7$ upto 16 GPa. We observe a phase transition at ~ 9 GPa above which the compressibility of the system decreases. Softening of the shear modulus was observed above the transition at 9 GPa from which we can predict a first order phase transition to occur at ultra higher pressures in this system.

## 7.5. Bibliography

[1] M. A. Subramanian, G. Aravamudan and G. V. Subba Rao, Prog. Solid State Chem. **15**, 55 (1983).

[2] A. E. Ringwood, S. Kesson, N. G. Ware, W. Hibberson, A. Major; Nature (London) **278** (1979) 219.

[3] R. C. Ewing, W. J. Weber, J. Lian, J. Appl. Phys. **95** (2004) 5949.

[4] K. V. Govindan Kutty, E. Asuvathraman, R. Raja et al. J. Phys. Chem. Sol. **66**, 2005, 296.

[5] John E. Greedan, Chem. Mat. **10**, 1998, 3058.

[6] R. Moessner and A. P. Ramirez, Phys. Today **59**(2), 24 (2006).

[7] J. S. Gardner, S. R. Dunsiger, B. D. Gaulin, M. J. P. Gingras, J. E. Greedan, R. F. Kiefl, M. D. Lumsden, W. A. MacFarlane, N. P. Raju, J. E. Sonier, I. Swainson, and Z. Tun, Phys. Rev. Lett. **82**, 1012 (1999).

[8] Mirebeau, I. N. Goncharenko, P. Cadavez-Peres, S. T. Bramwell, M. J. P. Gingras, and J. S. Gardner, Nature **420**, 54 (2002).

[9] Surajit Saha, D.V.S. Muthu, Surjeet Singh, B. Dkhil, R. Suryanarayanan, G. Dhalenne, H.K. Poswal, Sukanta Karmakar, Surinder M. Sharma, A. Revcolevschi and A. K. Sood, Phys. Rev. B **79**, 134112 (2009).

[10] Surajit Saha, D.V.S. Muthu, C. Pascanut, N. Dragoe, R. Suryanarayanan, G. Dhalenne, A. Revcolevschi, Sukanta Karmakar, Surinder M. Sharma and A. K. Sood, Phys. Rev. B **74**, 064109 (2006).

[11] T. T. A. Lummen, I. P. Handayani, M. C. Donker, D. Fausti, G. Dhalenne, P. Berthet, A. Revcolevschi, and P. H. M. van Loosdrecht, Phys. Rev. B **77**, 214310 (2008).

[12] J. P. C. Ruff, B. D. Gaulin, J. P. Castellan, K. C. Rule, J. P. Clancy, J. Rodriguez, and H. A. Dabkowska, Phys. Rev. Lett. **99**, 237202 (2007).

[13] S. H. Curnoe, Phys. Rev. B **78**, 094418 (2008).

[14] F. X. Zhang and S. K. Saxena, Chem. Phys. Letters **413**, 248 (2005); F. X. Zhang, B. Manoun, S. K. Saxena, and C. S. Zha, Appl. Phys. Lett. **86**, 181906 (2005).

[15] P. R. Scott, A. Midgley, O. Musaev, D.V.S. Muthu, S. Singh, R. Suryanarayanan, A.Revcolevschi, A.K. Sood and M.B. Kruger, High Pressure Res. **31**, 219 (2011).

[16] R.S. Kumar, A.L. Cornelius, M.F. Nicol, K.C. Kam, A.K. Cheetham, and J.S. Gardner, Appl. Phys. Let. **88**, 031903 (2006).

[17] L. H. Brixner, Inorg. Chem. **3**, 1065 (1964).

[18] A. P. Ramirez etal. Nature 1999,**399**,333.

[19] L pauling The nature of chemical bond (Cornell university press, Ithaca, NY, 1945).

**[20]** D. J. P. Morirs etal Science 2009, **326**, 411.

[21] A. K. Mishra, BARC, Mumbai, 2013.

[22] K. Fritch, Ph.D thesis, Massachusetts institute of technology, 1965.

[23] B. A. Auld, *Acoustic fields and waves in solids* (John Wiley & Sons, Inc., 1973), Vol. 1.

[24] L. G. Shcherbakova, L. G. Mamsurova, and G. E. Sukhanova, Russian Chemical Reviews **48**, 228 (1979).

[25] Y.-f. T. *e. al.*, Physical Review B **8**, 2688 (1973).

[26] A. R. Goñi, F. Kaess, J. S. Reparaz, M. I. Alonso, M. Garriga, G. Callsen, M. R. Wagner, A. Hoffmann, and Z. Sitar, Physical Review B **90**, 045208 (2014).

[27] N. M. Balzaretti and J. A. H. da Jornada, Solid State Communications **99**, 943 (1996).

[28] J. F. Nye, *Physical properties of crystals* (Oxford University press, 1985).

[29] Y. Luan, Ph.D thesis, University of Tennessee, 2011.

[30] W. Hayes and R. Louden, *Scattering of light by crystals* (John Wiley & sons, New York, 1978), p. 337.

[31] R. E. Newnham, *Properties of materials* (Oxford University press,. New York, 2005).

[32] F. Decremps, J. Zhang, B. Li, and R. C. Liebermann, Physical Review B **63**, 224105 (2001).

[33] F. Jiang, G. D. Gwanmesia, T. I. Dyuzheva, and T. S. Duffy, Physics of the Earth and Planetary Interiors **172**, 235 (2009).

[34] J. Zhang, B. Li, and Y. Zhao, High Pressure Research **28**, 415 (2008).

[35] S. Speziale, S. R. Shieh, and T. S. Duffy, Jornal of Geophysical Research **111**, B02203 (2006).

# Chapter 8

# Summary

The present thesis discusses the importance of Brillouin spectroscopy in studying the physical properties of variety of materials which includes an example each from metal organic framework, carbon nanotubes, ionic liquids and spin ice as a function of temperature and pressure. The summary of the results presented in this thesis can be pictorially represented as given below.

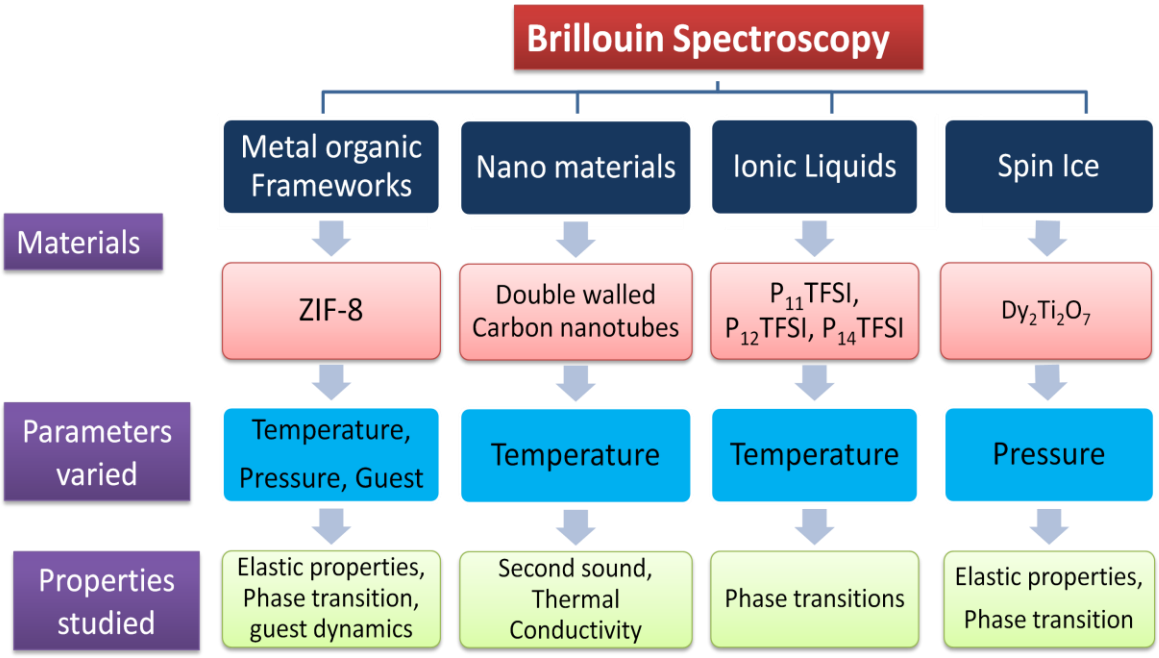


Fig. 8.1. The schematics of the thesis summary.

We have used Brillouin spectroscopy to study the effect of pore occupancy on the elastic constants in a prototypical MOF, zeolitic imidazolate framework (ZIF)-8 by incorporating various guest molecules at ambient, low temperatures and high pressures. The interaction between the guest and host affects the elastic properties, lifetimes and guest dynamics inside the pores. The temperature and pressure dependence of the acoustic modes demonstrated strengthening of the framework upon guest uptake as well as the ability of Brillouin spectroscopy to probe the flexibility of framework. Moreover the nature of the guests also plays an important role in determining the mechanical properties of ZIF-8. The use of Brillouin spectroscopy to study the elastic properties of MOF is much superior to the nano-indentation technique used as shown in this thesis. The Brillouin studies described here are the first report in this aspect to study the guest dependent mechanical

properties. Hence this thesis motivates research in the mechanical properties of MOFs using Brillouin spectroscopy and Raman spectroscopy along with x-ray structure determination.

Second sound is one of the rare phenomena by which heat transport occurs in materials and it results in very high thermal conductivity. We have demonstrated the existence of second sound in double walled carbon nanotubes for the first time using temperature dependent Brillouin spectroscopy and it exists at ambient conditions, unheard of before. Moreover our studies show that second sound exist in a large temperature regime which is very unusual. We have also determined different thermal conductivities existing in carbon nanotube mats from the central peaks in the Brillouin spectrum. An interesting future prospect for this work can be theoretical calculations to study the light scattering phenomena in the hydrodynamic regime for nanosystems.

While the temperature or the pressure can be used for detecting the phase transitions in materials, the temperature dependent Brillouin spectra in a series of alkylmethylpyrrolidinium bis(trifluoromethanesulfonyl) imide ($P_{1n}$TFSI, n=1,2,4) based ionic liquids showcased some unique trends in the Brillouin shift and FWHM in the plastic crystal and glassy phase in some of these ionic liquids. The high pressure Brillouin experiments on spin ice $Dy_2Ti_2O_7$ indicated a phase transition as well as pressure induced shear softening.

Hence this thesis illustrates that Brillouin spectroscopy has a huge potential in studying various physical properties of materials. Being a non contact probe to determine the elastic properties, the application of Brillouin spectroscopy can be extended to study the elastic properties of biomaterials and organic systems also. This will make Brillouin spectroscopy a promising technique for studying the physical properties of materials which are scientifically as well as industrially important.

.

## List of Publications relevant to this thesis

1. **Dhanya Radhakrishnan** and Chandrabhas Narayana, "*Effect of pore occupancy on the acoustic properties of ZIF-8: A Brillouin spectroscopic study at ambient and low temperatures"* J. Chem. Phy., **143**, 234703 (2015). **(Chapter 3)**
2. **Dhanya Radhakrishnan** and Chandrabhas Narayana, *"Guest dependent Brillouin and Raman scattering studies of Zeolitic Imidazolate Framework-8 (ZIF-8) under external pressure"* (J. Chem. Phy., 2016, In Press). **(Chapter 4)**
3. **Dhanya Radhakrishnan,** Chandrabhas Narayana and Ajay K Sood**, "***Second sound in carbon nanotubes"* (manuscript prepared). **(Chapter 5)**
4. Supti Das, **Dhanya Radhakrishnan**, Chandrabhas Narayana and Aninda J. Bhattacharyya, *"A Brillouin scattering investigation of solvent dynamics/Relaxations in Pyrrolidinium based Ionic Liquids"* (manuscript prepared). **(Chapter 6)**
5. **Dhanya Radhakrishnan**, A K Mishra, H. K. Poswal, Pallavi Ghalsasi, D V S Muthu, Chandrabhas Narayana, S M Sharma, Ajay K Sood *"High Pressure Studies on Spin Ice Pyrochlore $Dy_2Ti_2O_7$: X-ray Diffraction, Brillouin and Raman Spectroscopic Investigations"* (manuscript prepared). **(Chapter 7)**

## Miscellaneous works

1. Venkata Srinu Bhadram**,** Diptikanta Swain, **R Dhanya**, A. Sundaresan and Chandrabhas Narayana, "*Effect of pressure on octahedral distortions in rare-earth chromites ($RCrO_3$): role of R-ion size and its implications*", Mater. Res. Express, 1, 02611 (2014).
2. Umesha Mogera, Narendra Kurra, **R Dhanya**, Chandrabhas Narayana and Giridhar U. Kulkarni, "*Low cost, rapid synthesis of graphene on Ni: An efficient barrier for corrosion and thermal oxidation*", Carbon, **78**, 384 - 391 (2014).
3. Umesha Mogera, **Dhanya R**, Rajashekhar Pujar, Chandrabhas Narayana and Giridhar U. Kulkarni, *"Turbostratically Single Layer, Defect-free Graphene" Journal of Physical Chemistry Letters* **6**, 4437 - 4443 (2015).
4. Soumyabrata Roy, Sumanta Sarkar, Jaysree Pan, Umesh Waghmare, **Dhanya R**., Chandrabhas Narayana, Sebastian Peter, "*Synthetically Tuned Structural Disorder and Band Gap in Polyoxometalate Based Inorganic-Organic Hybrids"*(Inorg. Chem., 2016, In Press).

5. Sumanta Sarkar, Rohan Borah, Aggunda Santhosha, **Dhanya R**, Chandrabhas Narayana, Aninda J Bhattacharyya, Sebastian Peter, *"Sandwiched Heterostructure Composites of rGO/GeO2/PANI with Enhanced Performance for Li ion Battery Anode Material"* Journal of Power Sources, **306**, 791 (2016).
6. Rajib Sahu, **Dhanya Radhakrishnan**, Badri Vishal, Devendra Singh Negi, Anomitra Sil, Chandrabhas Narayana and Ranjan Datta, " Substrate induced tuning of compressive strain and phonon modes in large area $MoS_2$ and $WS_2$ van der Waals epitaxial thin films" (Submitted)